A Sub-mm perspective on massive galaxies in the early universe

Schouws; S.T.M.

A Sub-mm Perspective on Massive Galaxies in the Early Universe

Proefschrift

ter verkrijging van
de graad van doctor aan de Universiteit Leiden,
op gezag van rector magnificus prof.dr. S. de Rijcke,
volgens besluit van het college voor promoties
te verdedigen op dinsdag 1 september 2026
klokke 11:30 uur

door

Sander Schouws
geboren te Heemskerk, Nederland

Promotor:
Prof.dr. H.J.A. Röttgering

Co-promotores:
Dr. R.J. Bouwens
Dr. J.A. Hodge

Promotiecommissie:
Prof.dr. M.T. Kriek
Prof.dr. P.P. van der Werf
Prof.dr. J.F. Hennawi
Dr. J.J.A. Matthee (Institute of Science and Technology Austria)
Dr. M. Stefanon (University of Valencia)

God keep me from ever completing anything.
This whole book is but a draught—nay,
but the draught of a draught.
Oh, Time, Strength, Cash, and Patience!

— Herman Melville, *Moby-Dick*

Contents

Chapter 1

Introduction

IN THE BEGINNING

The story of galaxy formation begins with the birth of the universe itself 13.8 billion years ago. At that moment the seeds for galaxy formation were planted as tiny quantum fluctuations.

Only 300 million years later, these tiny fluctuations had already grown into the first galaxies which are already surprisingly luminous and detectable by our most sensitive telescopes. Moreover, just another 400 million years later we observe galaxies that are chemically already quite similar to the galaxies we observe in the local universe today.

The aim of this thesis is to explore this early epoch of rapid galaxy formation from a sub-mm perspective, ranging from the detection of oxygen in one of the most distant galaxies currently known at $z > 14$ to a comprehensive study of the strikingly evolved galaxies we see at $z \sim 7$.

In this introduction we will briefly review the theoretical framework of galaxy formation, how we observe these galaxies in the early universe and finally the processes in the interstellar medium (ISM) driving emission in the far infrared (FIR) and the key observables of high redshift galaxies. We conclude with the main questions that this thesis attempts to address and give an overview of the results.

1.1 SETTING THE STAGE

This section broadly outlines the theoretical framework at the basis of galaxy formation, from the underlying cosmology to the linear collapse of dark matter halos. This part of galaxy formation is very well understood and analytically tractable and sets the stage on which galaxy formation takes place, with the complicated and messy physics of baryons that actually make up the galaxies we observe.

1.1.1 *The ΛCDM Universe*

Our current best description of the universe is the standard model of cosmology, known as the Lambda-Cold Dark Matter (ΛCDM) model. This framework has proven remarkably successful for understanding the origin and evolution of the universe. Within this model, the energy density of the present-day universe is dominated by two enigmatic components: dark energy ($\Omega_{\Lambda,0} \approx 0.7$) and cold dark matter ($\Omega_{\rm DM,0} \approx 0.25$). The familiar baryonic matter that makes up gas, stars and planets only constitutes about 1/20 of the cosmic inventory ($\Omega_{\rm baryon,0} \approx 0.05$) (Planck Collaboration et al. 2020).

For each component X, Ω_X is the ratio of its energy density, ρ_X, to the critical density, $\rho_{\rm crit}$. The critical density is the natural density to compare to as it determines the shape of the universe. Current measurements agree that the sum of all components is unity ($\Omega = 1$), which implies that the universe does not have curvature.

These constituents, together with the assumption of isotropy and homogeneity, determine the expansion history of the universe. This expansion history is captured in the Friedmann equations, which are derived from the Einstein field equations for the Friedmann-Lemaître-Robertson-Walker metric. Solving the Friedmann equation gives the scale factor $a(t)$ as a function of time. The scale factor can be interpreted as the ratio between the size of the universe at time t relative to its present size. It furthermore is related to redshift as $a = 1/(1+z)$ and can thus be directly be inferred through spectroscopy by measuring z. Interestingly, this implies that at $z = 1$ the universe was only half the size of the current universe and at $z = 14$ the universe was much more compact at only $\sim$7% of its current size.

Because the energy density of each of the components in the universe scales differently with the scale factor, cosmic history can be divided into different epochs in which different components were dominant. In the current universe, dark energy became dominant around $z = 0.7$. Before the current epoch, the universe was matter dominated until very early in the universe ($z > 3400$), when radiation was the principal component. This means that most of cosmic structure formation and galaxy evolution took place in the matter dominated epoch.

1.1.2 *Collapse of Haloes*

The previous section described the evolution of a perfectly homogeneous and isotropic universe. However, the observed universe is filled with a rich hierarchy of structure. As mentioned before, these structures are the result of tiny fluctuations, set by the primordial power spectrum. Over long enough time these tiny fluctuations collapsed and formed the structures we observe today.

This collapse is governed by the interplay between self-gravity of these fluctuations, which seeks to amplify them, and the overall cosmic expansion, which works to dilute them ("Hubble friction"). The strength of a fluctuation is generally quantified in terms of the density contrast, $\delta(\mathbf{x}, t) = \frac{\rho(\mathbf{x},t)-\bar{\rho}(t)}{\bar{\rho}(t)}$, which measures the fractional overdensity at a given point in space relative to the cosmic mean density, $\bar{\rho}(t)$ at time t and location $\mathbf{x}$.

Conveniently, in the regime of tiny fluctuations ($\delta \ll 1$), the evolution of the overdensity can be calculated analytically. In a static universe, the collapse would be exponential, however in our expanding universe the collapse is generally power-law shaped. The precise rate of the growth depends critically on the dominant component of the universe's energy density at any given time. Specifically, during the matter dominated epoch, which is the epoch relevant for galaxy formation, structures grew as $\delta \propto (1+z)^{-1}$.

As fluctuations become more overdense, their evolution enters a highly non-linear phase. The gravitational collapse becomes a complex, multi-stream process that is analytically intractable, so numerical methods become necessary, such as cosmological N-body simulations.

Although linear theory cannot describe the nonlinear collapse itself, the spherical-collapse model establishes a useful correspondence between collapse and the linearly extrapolated density contrast. In this model, a perturbation is considered to have collapsed once its linearly extrapolated overdensity reaches the critical value $\delta_{lin,c} = 1.686$ (e.g. Gunn & Gott 1972; Press & Schechter 1974). This value does not represent the true overdensity of the perturbation, but rather it is the value that linear theory would predict at the time when the spherical perturbation formally collapses. By that stage the perturbation is already highly nonlinear and the process of virialization is underway.

1.1.3 *The Halo Mass Function*

The description of how fluctuations grow over time, cross $\delta_{lin,c}$ and collapse, can be combined with the initial distribution of the fluctuations as given by the primordial power spectrum. This gives an accounting of the number of collapsed halos of a certain mass in a fixed (comoving) volume at any point in time. The resulting distribution is known as the halo mass function (HMF).

The Halo Mass Function is shown in Figure 1.1 and exhibits a characteristic shape: a power-law at the low-mass end with a sharp exponential cutoff at the high-mass end. The sharp exponential cutoff is driven by the increasing rarity of massive haloes, which require a high sigma fluctuation in the primordial density field to be able to collapse early. In a fixed volume, there are not many such high-sigma fluctuations, causing the exponential cutoff. At the low mass end, the variance of the density contrast is much larger and crossing $\delta_{lin,c}$ is not a rare event. The power-law shape of this part of the HMF is predominantly driven by the shape of the primordial power spectrum.

For reference, in Figure 1.1 we show the number of halos that would be expected in a fixed survey volume of 1×1 deg^2 field of view, which is roughly typical for deep extragalactic surveys. Strikingly, this reveals a notable discrepancy between the predicted halo distribution and the galaxy populations we actually observe.

If we compare the number of galaxies spectroscopically confirmed at $z = 14$ and $z = 12$, the counts are roughly similar ($\sim 5-10$) (e.g. Harikane et al. 2023; Carniani et al. 2024). However, from the figure it is clear that for a given halo mass the expected number of halos increases by approximately an order of magnitude between z=14 and z=12. If galaxies simply traced the underlying halo population, we would expect a similar dramatic increase in galaxy counts, which is not supported by observations.

This discrepancy introduces what has been widely discussed in the literature as the "early galaxy tension" or the "early galaxy crisis" following the launch of the James Webb Space Telescope (JWST). Standard galaxy formation models, calibrated to match the galaxies we observe at lower redshifts, predicted a rapid, exponential decline in the UV luminosity function of galaxies at z>10. Instead, JWST has uncovered a surprisingly abundant population of exceptionally luminous, spatially extended, and chemically enriched systems.

The complicated connection between the underlying population of haloes and the galaxies we observe becomes even more apparent in the right panel of Figure 1.1. This figure shows the galaxy stellar mass function (GSMF) at $z = 7$ together with the HMF under the assumption that different fractions of the available baryons in each halo are converted to stars, i.e. a fixed star formation efficiency. Interestingly, there does not seem to be a fixed star formation efficiency that can explain the stellar masses we observe in galaxies across the full mass range and a mass-dependent efficiency is necessary to explain the data.

Both examples illustrate the stark differences between the predicted abundance of dark matter halos derived from beautiful analytic theory, and the complex real world of actual observed galaxy populations. Indeed, explaining both requires mechanisms that depend on (halo) mass and cosmic time. This is where baryonic processes take over, governing

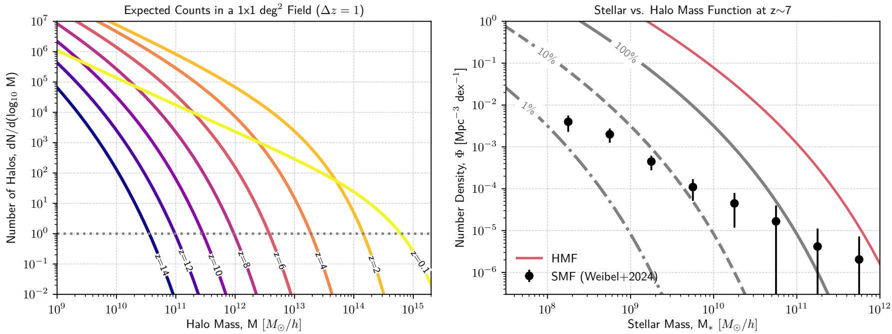

Figure 1.1. *Left panel:* The evolution of the dark matter halo mass function from $z = 14$ to $z = 0.1$. Instead of the usual counts per unit comoving volume it is shown in terms of number of halos per decade of mass in a 1×1 deg^2 field in a redshift interval of $\Delta z = 1$. The horizontal dashed line at y=1 indicates the threshold for expecting at least one halo per mass decade in such an area. *Right panel:* The halo mass function compared with the observed galaxy stellar mass function (GSMF) at $z = 7$ (Weibel et al. 2024). The grey lines illustrate the predicted GSMF under the simple assumption that a fixed fraction of the available baryons in every halo is converted into stars.

how gas cools and how different components of galaxies interact with this gas through feedback processes. How exactly these processes work is the most important open question in galaxy formation and evolution, and will be the focus of the next sections.

1.2 FROM DARK MATTER HALO TO GALAXY

The transformation of baryons within a dark-matter halo into an observable galaxy involves processes central to galaxy formation and evolution. Practically, to form a galaxy in a dark matter halo, large amounts of gas must undergo runaway collapse and form stars. This results in a competition between the self-gravity of the gas and its internal pressure. For gravity to win and form the stars we observe, the internal pressure must be sufficiently low and therefore the gas must become dense and cold.

However, there is a complication. As gas falls into the potential wells set by the dark matter, it converts potential energy into kinetic energy and is heated significantly. At high redshift, however, gas accretion is generally dominated by "cold mode accretion", where gas from the cosmic web flows directly into a developing galaxy along narrow, high-density filaments rather than spreading out into a spherical halo (Dekel et al. 2009). This bypasses the formation of a stable, hot atmosphere of gas enveloping the halo commonly found around massive halos at lower redshift. The inflowing gas is still heated to the halo's virial temperature, typically tens of thousands of Kelvin, through shocks where these streams converge at the halo's center. This high temperature causes the gas pressure to be far too high to allow the runaway gravitational collapse required to form stars. It is therefore crucial to cool the gas by radiating away this thermal energy.

1.2.1 *The Cooling Function*

This cooling is achieved when particles in the gas interact and convert their kinetic energy into radiation, which subsequently escapes and carries away thermal energy. There are several types of interactions that contribute to this and these processes depend on both temperature and the chemical composition of the gas. The combined efficiency of all processes is captured by the cooling function, denoted as $\Lambda(T, Z)$[1]. The cooling function for different metallicities is shown in Figure 1.2.

From the figure, two things can be noted. First, the presence of metals significantly enhances the ability of gas to cool. This is because metals open up numerous transitions in addition to those from hydrogen to radiate away energy. Second, there is a rapid drop in the cooling function below $\sim 10^4$ K. This is because at this temperature the hydrogen cooling channel shuts off catastrophically, both due to a lack of free electrons and insufficient thermal energy to excite hydrogen's lowest energy level (10.2 eV). Because hydrogen is the dominant component of any gas, the cooling rate drops by $>$4 orders of magnitude.

The precipitous drop in the cooling function creates a critical bottleneck, as gas would be unable to cool further were it not for mechanisms other than atomic hydrogen. This is where fine-structure line cooling and molecular cooling become paramount. Heavy elements like carbon and oxygen possess low-lying fine-structure energy levels that can be excited by collisions even in gas with temperatures of just a few hundred Kelvin. The same applies to molecules, which have rotational and vibrational excitations that can be excited at low temperatures.

Radiative de-excitation from these levels, producing far-infrared photons from lines such as [CII]158μm, allows the gas to bypass the 10.000 K

[1] It should be noted that the total cooling rate per unit of volume ($\mathcal{C}$) also strongly depends on the density $\mathcal{C} = n_e n_i \Lambda(T, Z)$, where n_e and n_i are the number densities of electrons and ions, respectively. This is because the radiative processes are two-body interactions involving an electron and an ion.

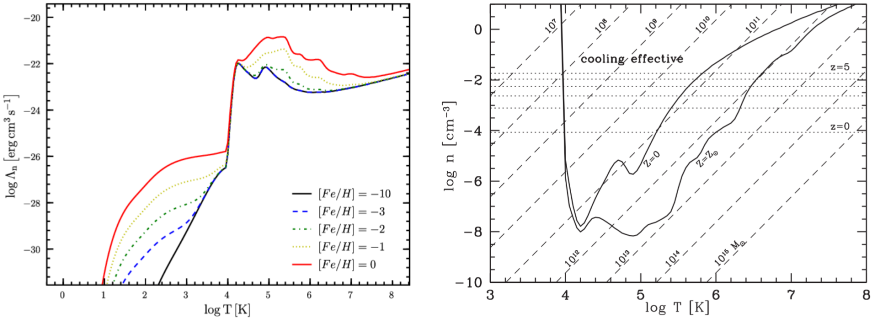

Figure 1.2. *Left panel:* The cooling function versus temperature for gas of different metallicities ([Fe/H]). Note the sharp increase in cooling above 10^4K and the strong dependence on metallicity. (Adapted from: Revaz et al. 2009) *Right panel:* The critical boundary for effective cooling ($t_{\rm cool} = t_{\rm ff}$) in the density-temperature plane for primordial and solar metallicity gas. Above this boundary cooling is effective, enabling catastrophic collapse. The dashed diagonal lines correspond to constant gas mass. The horizontal dotted lines indicate the characteristic density of virialized halos ($200\times\rho_{\rm crit}$). Because halos at higher redshift are intrinsically denser, gas within them is more likely to be in the effective cooling regime. For example, a gas mass of 10^8 $M_\odot$ resides in the inefficient region at z=0 but can cool effectively at z=5. (Adapted from: Mo et al. 2010)

temperature floor and continue its collapse. In the absence of metals, the only significant coolant below 10.000 K is molecular hydrogen (H_2), which is fragile and easily destroyed by UV radiation. The presence of metals therefore provides a far more robust and efficient cooling pathway in the low-temperature regime with cooling rates orders of magnitude higher than for primordial gas. These fine-structure cooling lines are at the core of the work presented in this thesis.

1.2.2 *Cooling Effectiveness*

To understand whether gas can collapse to form stars, we must compare two critical timescales: the cooling time ($t_{\rm cool}$) and the free-fall time ($t_{\rm ff}$).

The cooling time is the timescale over which the gas can radiate away its internal thermal energy (in the absence of heating), and it is defined as the ratio of the gas's thermal energy density to its cooling rate per unit volume. The cooling time scales as $t_{\rm cool} \propto T/n$. Notably, the cooling time decreases with increasing density. In contrast, the free-fall time represents the characteristic timescale for a cloud to collapse under its own gravity, which scales as $t_{\rm ff} \propto n^{-1/2}$ (e.g. Mo et al. 2010).

Cooling is considered "effective" when the cooling time is shorter than the free-fall time ($t_{\rm cool} < t_{\rm ff}$). In this regime, the gas loses its pressure support faster than it can dynamically respond to the change. This triggers a runaway process known as catastrophic cooling: as the gas cools and loses pressure, it gets compressed by gravity. Its density increases, which in turn shortens both the cooling time and the free-fall time, accelerating the collapse until stars are formed. The redshift of the universe plays a critical role here. The characteristic density of a virialized halo is tied to the critical density of the universe at that epoch, which scales as $(1+z)^3$. Halos at high redshift are therefore intrinsically much denser, which dramatically shortens their free-fall times and makes the condition for effective cooling much easier to satisfy.

Figure 1.2 provides a powerful visualization of this concept, plotting gas density against temperature. The solid lines delineate the critical boundary where $t_{\rm cool} = t_{\rm ff}$ for both primordial (Z=0) and solar-metallicity gas ($Z=Z_\odot$). The region to the upper-left of these lines is where cooling is effective. The dashed diagonal lines show the virial temperature and density for halos of a given mass. The figure shows that at high redshifts, virtually all halos massive enough to form stars reside in this catastrophic cooling regime.

This leads to an interesting and well-known issue: the "overcooling problem" (Benson et al. 2003). A naive interpretation of the physics above predicts that nearly all the baryonic gas accreted onto dark matter halos should have cooled, collapsed, and been converted into stars long ago. However, observations reveal a starkly different picture, where only a small fraction of the available baryons in a typical halo have actually formed stars. This discrepancy implies that heating and momentum injection must counteract cooling and regulate collapse. These processes are collectively known as feedback.

1.2.3 *Feedback Processes and the Need for Numerical methods*

Feedback processes inject the energy and momentum into the ISM that is necessary to regulate the formation of stars to match the galaxies we observe. These processes can either enhance star formation (positive feedback) or suppress it (negative feedback).

Observations indicate that the integrated efficiency with which halos convert their available baryons into stars varies strongly with halo mass (e.g. right panel of Figure 1.1). In the local universe this is most clearly observed in the relation between the halo mass and stellar mass of galaxies. This efficiency peaks at a halo mass of approximately $10^{12}\,M_\odot$ and decreases toward both higher and lower masses. (e.g. Moster et al. 2013). Different feedback mechanisms are generally invoked to explain the declining efficiencies below and above this characteristic halo mass.

Unfortunately, these processes are highly nonlinear and have complex interactions between themselves. This makes the problem too complex to solve analytically and numerical models are necessary. Two principal modeling approaches are used: semi-analytic models (SAMs) and cosmological hydrodynamical simulations.

Semi-analytical models are built on dark-matter-only simulations. These dark-matter simulations provide the underlying foundation of dark matter haloes and how they evolve. The baryonic physics is then implemented using different "recipes" that describe the gas cooling, star formation, chemical enrichment and feedback processes. This is computationally very efficient, but generally provides limited spatial information and significantly simplifies all the complex processes happening in a galaxy.

In contrast, (Cosmological) hydrodynamical simulations directly solve the equations of gravity, hydrodynamics, and thermodynamics on Eulerian grids, moving mesh methods or using Lagrangian particle methods (e.g., Smoothed Particle Hydrodynamics or moving-mesh codes). Modern suites such as IllustrisTNG and EAGLE (Vogelsberger et al. 2014; Schaye et al. 2015) allow for a much more detailed look at the processes happening inside galaxies.

However, because the physical scales of the relevant processes that impact star formation are separated by orders of magnitude, both approaches ultimately rely on assumptions and "subgrid" recipes that determine how they model the formation and evolution of galaxies. Moreover, these recipes need to be calibrated on observed data and cannot be derived from first principles.

Currently, most models implement two primary modes of feedback[2]. The first mode is driven by stellar sources, both stellar winds and radiation from massive stars, but most importantly energy injected by supernova explosions. Stellar feedback is especially influential in low-mass halos because, in sufficiently low-mass systems, the energy released by even a small num-

[2] This is in addition to feedback driven by environment (e.g. ram-pressure stripping and strangulation) and galaxy-galaxy interactions.

ber of supernovae can become comparable to the binding energy of the interstellar gas (e.g. Mo et al. 2010).

For massive haloes, however, supernova feedback is insufficient to prevent overcooling and it is expected that a different mechanism becomes dominant. This second mode of feedback is driven by Active Galactic Nuclei (AGN), which are fueled by the accretion of gas onto the Super Massive Black Holes (SMBHs) that are expected to be in the nucleus of every galaxy. The infall of gas onto an SMBH converts a substantial fraction of the accreted rest-mass energy into radiation, winds, and jets, which can happen in either short-lived extreme bursts (quasar mode) or a slower sustained mode (radio-mode).

However, both for supernova feedback and AGN feedback, the exact way in which they couple to the gas and drive the feedback is still unknown and remains one of the major open questions in galaxy formation. This is where simulations provide useful guidance, as each simulation implements these feedback mechanisms and other subgrid physics in unique ways and they can subsequently be compared to observations across cosmic history. Testing these models requires observational constraints on gas density, temperature, ionization, and chemical enrichment, many of which are obtained through spectroscopy of the high-redshift ISM.

1.3 PROBING THE ISM AT HIGH REDSHIFTS

1.3.1 *Emission Lines as tracers of the ISM*

To understand which mechanisms are responsible for this critical regulation of star formation, it is essential to characterize the physical conditions in the ISM of galaxies. This perspective is enabled through the study of emission lines.

The conditions in the ISM, such as chemical abundance, temperature, density and properties of the ionizing spectrum drive the strength of different emission lines and the continuum. Therefore, by measuring and comparing the strength of emission lines and the continuum, and testing these against models for the ISM, it is possible to gain critical insights into the physical conditions inside galaxies.

In the FIR, there is a large variety of detectable emission lines originating from all phases of the ISM that are relevant for star formation, as illustrated in Figure 1.3. This can be complemented with strong emission lines from the rest-frame UV and optical parts of the spectrum. However, because of the higher energies of optical and rest-UV photons, these

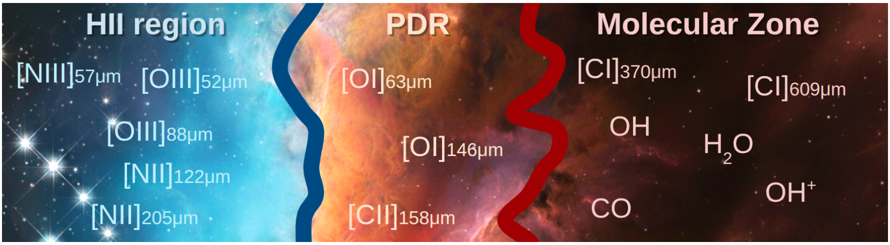

Figure 1.3. A schematic overview of some of the strongest emission lines available in the far-infrared. All phases of the ISM surrounding a star-forming region can be studied with several emission lines. These lines enable a unique view of the physical processes that dominate these regions.

lines predominantly originate from the hottest phases of the ISM ($\gtrsim$10.000 K). Therefore, in normal galaxies, optical and UV lines mostly originate from HII regions, which means that FIR lines offer a unique perspective on other colder/neutral phases of the ISM such as PDR regions and molecular clouds.

This thesis is focused on two of the strongest FIR lines that we can detect with current facilities, the [CII]158μm line and the [OIII]88μm. In the next sections, we will explore the physics governing these lines as well as the underlying dust continuum.

1.3.2 *The [CII]158μm line*

1.3.2.1 *Where does [CII] originate in the ISM?*

Due to its low ionization potential compared to hydrogen (11.3 eV versus 13.6 eV) and low critical density ($n_e \sim 10 - 45$ cm^{-3} at 100K and 8000K respectively (e.g. Goldsmith et al. 2012)), [CII] can be emitted from all major phases of the ISM. In particular the ionized phase (HII regions and diffuse ionized gas), the warm and cold neutral medium (WNM, CNM), photon-dominated regions (or photodissociation regions; PDRs (Hollenbach & Tielens 1999)) and the edges of molecular clouds[3] (Pineda et al. 2013) all contribute to the total [CII] luminosity. We discuss the relative contribution of these phases to the total [CII] luminosity in the context of high redshift galaxies below.

[3] In particular those regions where neutral hydrogen (HI) has already been transformed into H_2 (protected by self-shielding), but the column densities are low enough for that C^+ has not yet transitioned to C^0 and CO (e.g. Madden 2000; Langer et al. 2010) (also referred to as CO-dark H_2 gas (Pineda et al. 2013)).

For the [CII] luminosity originating in the WNM and CNM, the CNM dominates (>95%) due to the low density of the WNM (Wolfire et al. 2010; Vallini et al. 2013). Large-scale Herschel surveys have found that for the Milky Way, the contribution of the CNM to the total [CII] luminosity is about 21% (Pineda et al. 2013), however this contribution is expected to be substantially lower in high redshift galaxies ($z > 4.5$) due to the increasing temperature of the CMB background. When CMB temperature becomes similar to the spin temperature of [CII] in the CNM, the [CII] emission from the CNM is attenuated by >80-90% (Vallini et al. 2013; Lagache et al. 2018). It is thus expected that the CNM and WNM only contribute a negligible amount to the total [CII] luminosity of high redshift galaxies.

In the Milky Way it has been found that the ionized component contributes only 4% to the total [CII] luminosity (Pineda et al. 2013), however, studies of a broader sample of local galaxies have found average contributions of $\sim 20 - 30\%$ (Parkin et al. 2013; Hughes et al. 2017; Díaz-Santos et al. 2017; Croxall et al. 2017; Cormier et al. 2015, 2019). Studies at higher redshifts give similar results (e.g. Stacey et al. 2010; Decarli et al. 2014; Gullberg et al. 2015). This is corroborated by simulations of high redshift galaxies, which also find that ionized gas can contribute around $\sim 20-40\%$ to the total [CII] luminosity (Accurso et al. 2016; Olsen et al. 2017). Currently observational constraints at $z > 5$ are unfortunately nonexistent, so it cannot be ruled out that a substantial fraction of the total [CII] luminosity of high redshift galaxies originates from ionized regions. However, it is probably quite low. In particular, studies of local galaxies found that the fraction coming from ionized regions in local (U)LIRGs anti-correlates with dust temperature (Díaz-Santos et al. 2017). In local dwarf galaxies, it was found that the contribution from ionized regions is lower at lower metallicities and higher ionization parameters (Cormier et al. 2019), something that has also been corroborated in simulations (e.g. Lupi & Bovino 2020). Hotter dust temperatures, lower metallicities and higher ionization parameters are precisely the conditions we expect in high-redshift galaxies (e.g. Stark et al. 2016; J. Bouwens et al. 2016; Sommovigo et al. 2020). It is therefore likely that the contribution from ionized regions to the total [CII] luminosity in high redshift galaxies most likely is quite limited (<10%). However, more observations are essential to properly constrain this, for example using the $[NII]_{122\mu m}$ and/or $[NII]_{205\mu m}$ lines (Oberst et al. 2006; Hughes et al. 2017).

This means that most likely the majority of [CII] emission (>60%−90%) in high redshift galaxies originates from PDRs and the edges of molecular clouds. This is already the case in the Milky Way, where ∼75% of the total [CII] luminosity originates from these regions: ∼47% originates from dense PDR regions and ∼28% from CO-dark H_2 clouds (Pineda et al. 2013), consistent with observations in a broad range of local galaxies (Díaz-Santos et al. 2017; Croxall et al. 2017; Parkin et al. 2013; Hughes et al. 2017; Cormier et al. 2015, 2019). This is also seen in simulations of high redshift galaxies, for which the majority of [CII] emission comes from the PDR and molecular phases (Accurso et al. 2016; Olsen et al. 2017; Pallottini et al. 2019). Hence, modeling the physical processes in PDR regions is essential to understanding the origin of [CII] (Ferrara et al. 2019).

1.3.2.2 *Primary physical processes influencing [CII] from PDR regions*

The luminosity of the [CII] line from PDR regions is subject to a complex interplay of physical effects. Below we give a brief review of the parameters which are most often discussed in the literature in the context of high-z galaxies.

One of the primary parameters often used to explain a possible evolution in the luminosity of [CII] compared to the ongoing star formation, is the metallicity. Carbon abundance scales linearly with metallicity and subsequently does the [CII] luminosity at a fixed (hydrogen) column density ($L \propto Z$). Lower metallicities would thus result in lower [CII] luminosities. However, if the total column density is large and shielding is dominated by dust (and assuming a fixed dust-to-metal ratio), the PDR column density scales inversely proportional to the metallicity ($L \propto 1/Z$). In that case, both effects cancel each other and the [CII] luminosity is independent of metallicity ($L \propto Z \times 1/Z \propto constant$) (Pallottini et al. 2019; Ferrara et al. 2019; Harikane et al. 2020). Whether this is the case for high redshift galaxies depends on their metallicity and the total gas column densities of their PDR regions. For lower metallicities, the column densities will need to be increasingly large to compensate for the decreasing carbon abundance. This only works until the dust opacity at the total column density becomes smaller than unity ($\tau_{dust} < 1$) and PDR becomes density bounded, after this point you run out of gas before running out of photons and [CII] becomes sensitive to metallicity (e.g. Vallini et al. 2015; Olsen et al. 2017; Lagache et al. 2018; Pallottini et al. 2019; Ferrara et al. 2019).

A lower dust-to-metals ratio (at fixed metallicity) can also impact the [CII] emission. In most cases, the outer boundary of PDR regions is primarily determined by the dust opacity. Decreasing the dust-to-metals ratio increases the size of PDR regions, which in turn increases the [CII] luminosity. It has been found that the dust-to-metals ratio decreases for lower metallicities (e.g. De Cia et al. 2016; Wiseman et al. 2017; De Vis et al. 2019), possibly due to more efficient dust destruction in those conditions (e.g. Triani et al. 2020). The same reasoning applies to a lower dust-to-gas ratio at fixed metallicities. Lower dust-to-metal or dust-to-gas ratios can increase the [CII] emission from high redshift galaxies.

The ionization parameter can also have a large impact on the [CII] luminosity. Increasing the ionization parameter increases the size of HII regions, but does not impact the outer boundary of the PDR regions, since that is determined by the dust opacity. For a gas cloud or galaxy with a total fixed column density, this effectively shrinks the size of the PDR region and this consequently decreases the [CII] luminosity (e.g. Ferrara et al. 2019). One of the main drivers of a higher ionization parameter is bursty star formation, which is abundant in the early universe (e.g. Stark et al. 2016).

Geometric effects can also impact the [CII] emission. Normally, models often assume that the complete HII region is surrounded by a PDR region (and ultimately embedded in a molecular cloud), but this is not necessarily the case in actual galaxies. One way to model the effects of a more complex geometry is through the PDR coverage factor. A low PDR coverage factor could, for example, be caused by outflows that blow away neutral gas or when the HII regions are primarily density bounded, in particular when the whole galaxy becomes ionized. Decreasing the PDR coverage factor can drastically lower the [CII] emission of high redshift galaxies (e.g. Cormier et al. 2019; Harikane et al. 2020).

Particle density is another parameter that impacts [CII] luminosities. Increasing the density at a fixed ionizing photon flux decreases the ionization parameter, which increases the [CII] luminosity. However, it also changes the size of HII regions and the outer boundary of PDR regions at different rates. In addition, collisional de-excitation also starts playing a role when the density approaches the critical density ($n_e = 3000 cm^{-3}$ for H^0 at 100K (Goldsmith et al. 2012)). Finally, carbon chemistry is also important as carbon is stored away in CO with increasing efficiency at higher densities (e.g. Popping et al. 2019). Harikane et al. (2020) modeled these effects for ionization-bounded PDR regions using CLOUDY and found that increasing the density results in lower [CII] luminosities. This is consistent with other studies (e.g. Popping et al. 2019), which also find that increasing the external ISM pressure surrounding molecular clouds (which increases their density) decreases the [CII] emission.

Finally, the CMB background can also have a significant effect on some regions that emit [CII], like the CNM as discussed above. However, for regions with $T > 100K$ and $n_e \gtrsim 100$, where we expect the majority of the [CII] emission to originate, the CMB effects are negligible (e.g. Pallottini et al. 2019; Laporte et al. 2019). Lastly, more exotic effects like thermal saturation of the upper quantum level, grain charging, and X-ray ionization from AGN activity might play an important role in more extreme conditions (e.g. Smith & Edge 2017; Rybak et al. 2019).

1.3.3 *The [OIII]88μm and [OIII]5007Å lines*

In contrast to singly ionized carbon (C+; [CII]), doubly ionized oxygen (O++; [OIII]) requires a significantly higher energy of 35.1 eV to form from O+, an energy level substantially greater than the 13.6 eV needed to ionize hydrogen. Consequently, [OIII] emission is exclusively produced in the ionized phases of the ISM. These phases primarily consist of dense HII regions surrounding young, massive star clusters and the more diffuse Warm Ionized Medium (WIM). However, the contribution from the WIM to the total [OIII] luminosity is generally considered negligible. This is due to the WIM's very low density compared to HII regions and the scarcity of photons with sufficient energy to doubly ionize oxygen far from their stellar sources. Therefore, both the rest-frame optical [OIII]5007Å nebular line and the far-infrared [OIII]88μm fine-structure line are generally accepted to originate almost entirely from the dense, ionized gas within HII regions (e.g. Tielens 2005).

The luminosity of the [OIII] lines is governed by the physical conditions within these HII regions. On a fundamental level, the strength of oxygen emission lines is tied to the abundance of oxygen. For a given ionizing radiation field, a higher gas-phase metallicity provides more oxygen atoms available for ionization, thus leading to potentially more luminous [OIII] emission. The detection of a bright oxygen line in galaxies at cosmic dawn can therefore indicate that rapid chemical enrichment has already occurred in the early universe.

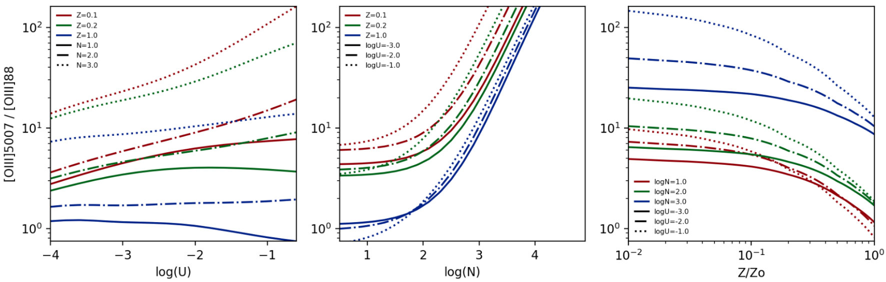

Figure 1.4. The dependence of the [OIII]5007Å/[OIII]88μm line ratio on the dominant ISM properties from Cloudy modelling, ionization parameter (log(U)), density (log(N)) and metallicity ($Z/Z_\odot$). The line ratio is most sensitive to the density, as visible from the center panel. The metallicity also has some impact, due to its impact on electron temperature. (Figure is based on CLOUDY models from Witstok et al. 2023.)

Due to its high energy requirement, the production of O++ is also sensitive to the ionization parameter (U), as well as the hardness of the incident radiation field. Environments with high ionization parameters and hard ionizing spectra, typically produced by very young (<10 Myr), massive stellar populations, create larger zones of doubly ionized oxygen, thereby boosting [OIII] emission.

Finally, the density also impacts the line emission of O++; specifically the strength of the [OIII]88μm is suppressed compared to [OIII]5007Å at higher densities. This makes the [OIII]5007Å/[OIII]88μm line ratio a uniquely useful diagnostic of electron density (e.g. Fujimoto et al. 2024).

1.3.3.1 *The [OIII]5007Å/[OIII]88μm Line Ratio*

The ratio of the [OIII]5007Å and [OIII]88µm emission lines serves as a powerful diagnostic of the physical conditions within HII regions, primarily due to their significantly different critical densities for collisional de-excitation. The far-infrared 88µm fine-structure line has a critical density of approximately 500 cm^{-3}, whereas that of the optical 5007Å nebular line is much higher, around 7×10^5 cm^{-3}. Below its critical density, a line's emissivity scales with the square of the electron density (n^2), as nearly every collision leads to a radiative decay. Above the critical density, however, collisional de-excitations become dominant, and the emissivity scales only linearly with density (n) (e.g. Tielens 2005). Consequently, in the density regime between these two values ($\sim 10^2$ - 10^5 cm^{-3}), the 5007Å emission grows more rapidly with increasing density than the 88μm emission. This makes their ratio a sensitive probe of the electron density, as illustrated in the central panel of Figure 1.4.

As is also evident from the figure, the line ratio exhibits secondary dependencies on both the gas-phase metallicity and the ionization parameter. Both of these are a consequence of the ratio's dependence on electron temperature (T_e) within the HII regions. A lower metallicity gas contains fewer heavy elements, which are the primary coolants in ionized gas. This results in less efficient cooling and therefore higher equilibrium electron temperatures. Similarly, a higher ionization parameter is also associated with elevated electron temperatures.

This impacts the resulting line ratio because the collisional excitation of the upper energy level for the 5007Å transition requires significantly more energy (2.5 eV) than that of the 88μm transition (0.016 eV). Consequently, the emissivity of the 5007Å is much more sensitive to the electron temperature than the 88μm line. In hotter, lower-metallicity environments, the [OIII]5007Å line is preferentially enhanced relative to the [OIII]88μm line, resulting in a higher overall line ratio.

1.3.4 *Dust Continuum*

Beyond the gaseous components, dust is a crucial ingredient of the ISM. Dust consists of solid, often sub-micron sized particles, primarily composed of heavy elements (metals) such as silicates and carbon, which can condense in various environments. Dust grains are highly effective at absorbing short-wavelength ultraviolet (UV) and optical radiation, which is subsequently re-radiated as thermal emission at longer, far-infrared (FIR) wavelengths. This process of absorption and re-emission significantly impacts what we observe in different parts of the spectrum. On one hand, it means that dust obscures star formation at rest-frame UV and optical wavelengths, necessitating corrections to derive the total star formation rate. On the other hand, the thermal FIR emission provides a direct tracer of this obscured star formation, offering a complementary window into the star-forming activity of galaxies.

Dust is not merely a passive screen, however; it plays an active role in governing the physical processes within the ISM. The surfaces of dust grains act as crucial catalysts for the formation of molecular hydrogen (H_2), the primary fuel for star formation, a process that is otherwise highly inefficient in the gas phase. Furthermore, dust can be an important coolant in dense gas, aiding in the fragmentation of molecular clouds and thereby directly influencing the formation of stars. Perhaps its most critical role in the context of FIR diagnostics is in heating the neutral ISM. Far-ultraviolet (FUV) photons (between 6.0 and 13.6 eV) can strike dust grains and eject energetic electrons via the photoelectric effect. These photoelectrons then heat the surrounding neutral gas through collisions. This heating mechanism is the primary energy source for photodissociation regions (PDRs) and is essential for powering the strong far-infrared cooling lines, especially the [CII] 158μm line (e.g. Tielens 2005).

The production of dust is governed by a few key formation channels. The primary stellar sources are broadly divided into two categories, operating on vastly different timescales. The first, and most rapid, channel is through core-collapse supernovae (SNe). These explosions mark the end of the lives of massive, short-lived stars, injecting newly synthesized dust into the ISM on timescales of just a few tens of millions of years. Given the short timescales involved, SNe are expected to be the dominant dust production mechanism in the early universe (e.g. Michałowski 2015). However, the net dust yield from SNe is still a subject of significant debate, as a substantial fraction of the newly formed grains could be destroyed by the supernova's own reverse shock as it propagates through the surrounding medium.

The second stellar channel involves the stellar winds of asymptotic giant branch (AGB) stars. These are lower-mass, longer-lived stars that enrich the ISM on much longer timescales, typically hundreds of millions of years or more. Consequently, while AGB stars are a major source of dust in the local universe, they are not expected to be a significant contributor to the dust budget of galaxies at the high redshifts explored in this thesis, because at those high redshifts the universe is sufficiently young that not enough time has passed for AGB stars to be a major contributor to the dust budget (e.g. Michałowski 2015).

Finally, in addition to direct stellar production, dust mass can also increase through grain growth within the interstellar medium itself. This process, which involves the accretion of gas-phase metals onto the surfaces of pre-existing 'seed' grains, can operate on either short or very long timescales depending on the local ISM conditions (e.g. Dayal & Ferrara 2018). It could potentially be an important channel for dust mass buildup in the dense, metal-enriched environments of early star-forming galaxies.

A complete understanding of the cosmic dust budget requires considering not only these formation sources but also the processes that remove or destroy dust. Grains can be shattered or sputtered by energetic supernova shocks propagating through the ISM, or they can be permanently removed from a galaxy via powerful galactic outflows. The net amount of dust observed in any galaxy is therefore a complex balance between these sources and sinks, a balance that is crucial for interpreting the properties of high-redshift galaxies.

1.3.5 *Observing the ISM with ALMA and JWST*

The previous sections highlighted how studying the dust continuum emission and emission lines, either in the FIR or UV/optical, is invaluable to gain insight into the properties of galaxies. To study this emission in practice, only a few facilities are sensitive enough and have the wavelength coverage to detect these faint features from distant galaxies.

For the FIR, the Atacama Large Millimeter/submillimeter Array (ALMA) is the most capable instrument, being able to detect the [CII] line in less than an hour in bright $z{\sim}7$ galaxies and [OIII] in a few hours in the brightest $z{\sim}14$ galaxy. It should be noted, however, that detecting the dust continuum is generally more difficult than detecting emission lines.

For rest-frame optical lines, at higher redshifts ($z{\gtrsim}6$), the atmospheric absorption increasingly becomes a problem. For these lines, observations from space are essential, which have become possible with the launch of the James Webb Space Telescope (JWST). This facility has rapidly become the most important tool to study galaxies in the early universe.

1.4 **THIS THESIS**

The overarching goal of studying galaxies at cosmic dawn and the Epoch of Reionization is to understand how the first dark matter haloes were populated with baryonic matter, how they formed stars, and how they subsequently enriched their interstellar media. Within this broad context, several key open questions continue to drive observational efforts: What fraction of early star formation is obscured by dust? How do we robustly identify and characterize galaxies in an increasingly neutral universe? And what are the specific physical conditions—such as ionization state, chemical abundance, and feedback efficiency—within the first generation of galaxies? While a single thesis cannot resolve these fundamental questions, the work presented here provides pieces to this puzzle by leveraging the unique capabilities of ALMA.

Chapter 2 of this thesis addresses the first of these challenges, focusing on early dust buildup and obscured star formation. We utilized the dust continuum to uncover the star formation activity hidden from rest-frame UV view. We targeted a sample of 15 luminous Lyman-break galaxies at z∼7-8 with sensitive ALMA continuum observations, detecting dust emission in six sources and effectively doubling the number of known dust-detected galaxies at z>6.5 at the time. By combining these measurements with deep optical photometry, we constrained the relationship between infrared excess and the UV-continuum slope (IRX–β), finding that these early systems favor a steeper attenuation curve consistent with rapid dust production mechanisms such as supernovae; we also explore the impact of the assumed dust temperature on this result. Crucially, these results demonstrated that even among UV-selected populations, approximately one-third of the star formation is obscured by dust, necessitating significant corrections to the cosmic star formation rate density during the Epoch of Reionization.

Chapter 3 is focused on confirming and characterizing galaxies in the Epoch of Reionization. Before JWST was available, one of the critical bottlenecks in studying high-redshift galaxies was the sheer difficulty of obtaining spectroscopic redshifts. This was made difficult by the lack of strong lines available to ground-based spectroscopy, which at z>6.5 is mostly limited to Lyman-α. Unfortunately, the increasingly neutral universe at these redshifts strongly absorbs this line. Despite its relatively small instantaneous redshift coverage, especially compared to optical spectroscopy, we demonstrate the efficacy of blindly searching for redshifts with ALMA by stitching together multiple observations. Building on the work of Smit et al. (2018), we targeted a sample of six luminous Lyman-break galaxies at z∼7, selected from the COSMOS/UltraVISTA field based on tight photometric redshift constraints derived from Spitzer/IRAC colors. By scanning for the [CII] 158μm line, we achieved reliable detections for 50% of the sample, confirming that this method was highly efficient for UV-bright sources. Beyond providing precise redshifts, these observations enabled a characterization of the ISM and kinematics of these early systems, revealing a surprisingly diverse mix of dynamical states ranging from ordered rotation to complex mergers. These findings confirmed that the [CII] properties of z∼7 galaxies are largely consistent with local scaling relations and validated the observational strategy that laid the groundwork for the REBELS Large Program.

The launch of JWST has spectacularly shifted the observational frontier to the cosmic dawn (z>10), allowing us to directly probe the physical conditions of the very first galaxies. *Chapter 4* presents the ALMA detection of [OIII] 88μm in JADES-GS-z14-0. This observation yields a robust spectroscopic redshift of z=14.179, making it the most distant confirmation achieved with ALMA to date. The detection reveals a surprisingly chemically enriched system (Z$\sim$0.1-0.2 $Z_\odot$) just 300 million years after the Big Bang, while the non-detection of the dust continuum places strict constraints on early dust production mechanisms. These results demonstrate that even in the JWST era, ALMA remains an indispensable tool for characterizing the physical state and rapid evolution of the earliest known galaxies.

Finally, addressing the open question of how feedback regulates early galaxy formation, *Chapter 5* delves deeper into the physical state of this primordial galaxy through deep ALMA observations targeting the [CII] 158μm line. In contrast to the bright [OIII] emission, [CII] remained undetected, placing a lower limit on the [OIII]/[CII] ratio (>3.5) consistent with an interstellar medium characterized by extreme ionization conditions and surprisingly low gas densities. By using the [CII] limit as a tracer for the neutral gas reservoir, we inferred a relatively low gas fraction (f_{gas} <0.77), which stands in contrast to the gas-rich nature expected at these redshifts. When combined with the absence of dust continuum, these results suggest that strong feedback from a recent starburst may have efficiently expelled much of the fuel from the galaxy, painting a picture of JADES-GS-z14-0 as a rapidly evolving system caught in a violent "post-outflow" phase.

REFERENCES

Accurso, G., Saintonge, A., Bisbas, T. G., & Viti, S. 2016, Monthly Notices of the Royal Astronomical Society, 464, 3315–3330.

Benson, A., Bower, R., Frenk, C., et al. 2003, The Astrophysical Journal, 599, 38–49.

Carniani, S., Hainline, K., D'Eugenio, F., et al. 2024, Nature, 633, 318

Cormier, D., Madden, S. C., Lebouteiller, V., et al. 2015, Astronomy & Astrophysics, 578, A53.

Cormier, D., Abel, N. P., Hony, S., et al. 2019, Astronomy & Astrophysics, 626, A23.

Croxall, K. V., Smith, J. D., Pellegrini, E., et al. 2017, The Astrophysical Journal, 845, 96.

Dayal, P., & Ferrara, A. 2018, PhR, 780, 1

De Cia, A., Ledoux, C., Mattsson, L., et al. 2016, Astronomy amp; Astrophysics, 596, A97.

De Vis, P., Jones, A., Viaene, S., et al. 2019, Astronomy amp; Astrophysics, 623, A5.

Decarli, R., Walter, F., Carilli, C., et al. 2014, The Astrophysical Journal, 782, L17.

Dekel, A., Birnboim, Y., Engel, G., et al. 2009, Nature, 457, 451

Díaz-Santos, T., Armus, L., Charmandaris, V., et al. 2017, The Astrophysical Journal, 846, 32.

Ferrara, A., Vallini, L., Pallottini, A., et al. 2019, Monthly Notices of the Royal Astronomical Society, 489, 1–12.

Fujimoto, S., Ouchi, M., Nakajima, K., et al. 2024, The Astrophysical Journal, 964, 146.

Goldsmith, P. F., Langer, W. D., Pineda, J. L., & Velusamy, T. 2012, The Astrophysical Journal Supplement Series, 203, 13.

Gullberg, B., De Breuck, C., Vieira, J. D., et al. 2015, Monthly Notices of the Royal Astronomical Society, 449, 2883–2900.

Gunn, J. E., & Gott, III, J. R. 1972, ApJ, 176, 1

Harikane, Y., Ouchi, M., Inoue, A. K., et al. 2020, The Astrophysical Journal, 896, 93.

Harikane, Y., Ouchi, M., Oguri, M., et al. 2023, ApJS, 265, 5

Hollenbach, D., & Tielens, A. 1999, Reviews of Modern Physics, 71, 173

Hughes, T. M., Ibar, E., Villanueva, V., et al. 2017, Astronomy & Astrophysics, 602, A49.

J. Bouwens, R., Aravena, M., Decarli, R., et al. 2016, The Astrophysical Journal, 833, 72.

Lagache, G., Cousin, M., & Chatzikos, M. 2018, Astronomy & Astrophysics, 609, A130.

Langer, W. D., Velusamy, T., Pineda, J. L., et al. 2010, Astronomy and Astrophysics, 521, L17.

Laporte, N., Katz, H., Ellis, R. S., et al. 2019, Monthly Notices of the Royal Astronomical Society: Letters, 487, L81–L85.

Lupi, A., & Bovino, S. 2020, Monthly Notices of the Royal Astronomical Society, 492, 2818–2827.

Madden, S. C. 2000, New Astronomy Reviews, 44, 249–256.

Michałowski, M. J. 2015, Astronomy amp; Astrophysics, 577, A80.

Mo, H., van den Bosch, F. C., & White, S. 2010, Galaxy Formation and Evolution, doi:10.1017/CBO9780511807244

Moster, B. P., Naab, T., & White, S. D. M. 2013, MNRAS, 428, 3121

Oberst, T. E., Parshley, S. C., Stacey, G. J., et al. 2006, The Astrophysical Journal, 652, L125–L128.

Olsen, K., Greve, T. R., Narayanan, D., et al. 2017, The Astrophysical Journal, 846, 105.

Pallottini, A., Ferrara, A., Decataldo, D., et al. 2019, Monthly Notices of the Royal Astronomical Society, 487, 1689–1708.

Parkin, T. J., Wilson, C. D., Schirm, M. R. P., et al. 2013, The Astrophysical Journal, 776, 65.

Pineda, J. L., Langer, W. D., Velusamy, T., & Goldsmith, P. F. 2013, Astronomy & Astrophysics, 554, A103.

Planck Collaboration, Akrami, Y., Ashdown, M., Aumont, J., et al. 2020, Astronomy amp; Astrophysics, 641, A11.

Popping, G., Pillepich, A., Somerville, R. S., et al. 2019, The Astrophysical Journal, 882, 137.

Press, W. H., & Schechter, P. 1974, ApJ, 187, 425

Revaz, Y., Jablonka, P., Sawala, T., et al. 2009, A&A, 501, 189

Rybak, M., Rivera, G. C., Hodge, J. A., et al. 2019, The Astrophysical Journal, 876, 112.

Schaye, J., Crain, R. A., Bower, R. G., et al. 2015, Monthly Notices of the Royal Astronomical Society, 446, 521

Smit, R., Bouwens, R. J., Carniani, S., et al. 2018, Nature, 553, 178

Smith, R. J., & Edge, A. C. 2017, Monthly Notices of the Royal Astronomical Society: Letters, 471, L66–L70.

Sommovigo, L., Ferrara, A., Pallottini, A., et al. 2020, Monthly Notices of the Royal Astronomical Society, 497, 956–968.

Stacey, G. J., Hailey-Dunsheath, S., Ferkinhoff, C., et al. 2010, The Astrophysical Journal, 724, 957–974.

Stark, D. P., Ellis, R. S., Charlot, S., et al. 2016, Monthly Notices of the Royal Astronomical Society, 464, 469–479.

Tielens, A. G. G. M. 2005, The Physics and Chemistry of the Interstellar Medium

Triani, D. P., Sinha, M., Croton, D. J., Pacifici, C., & Dwek, E. 2020, Monthly Notices of the Royal Astronomical Society, 493, 2490–2505.

Vallini, L., Gallerani, S., Ferrara, A., & Baek, S. 2013, Monthly Notices of the Royal Astronomical Society, 433, 1567.

Vallini, L., Gallerani, S., Ferrara, A., Pallottini, A., & Yue, B. 2015, The Astrophysical Journal, 813, 36.

Vogelsberger, M., Genel, S., Springel, V., et al. 2014, Monthly Notices of the Royal Astronomical Society, 444, 1518

Weibel, A., Oesch, P. A., Barrufet, L., et al. 2024, Monthly Notices of the Royal Astronomical Society, 533, 1808.

Wiseman, P., Schady, P., Bolmer, J., et al. 2017, Astronomy amp; Astrophysics, 599, A24.

Witstok, J., Jones, G. C., Maiolino, R., Smit, R., & Schneider, R. 2023, Monthly Notices of the Royal Astronomical Society, 523, 3119.

Wolfire, M. G., Hollenbach, D., & McKee, C. F. 2010, The Astrophysical Journal, 716, 1191.

Chapter 2

Significant Dust-Obscured Star Formation in Luminous Lyman-break Galaxies at $z \sim 7-8$

We make use of ALMA continuum observations of 15 luminous Lyman-break galaxies at $z \sim$ 7-8 to probe their dust-obscured star-formation. These observations are sensitive enough to probe to obscured SFRs of 20 $M_{\odot}$/yr (3σ). Six of the targeted galaxies show significant ($\geq 3\sigma$) dust continuum detections, more than doubling the number of known dust-detected galaxies at $z > 6.5$. Their IR luminosities range from 2.7×10^{11} $L_{\odot}$ to 1.1×10^{12} $L_{\odot}$, equivalent to obscured SFRs of 25 to 101 $M_{\odot}$/yr. We use our results to quantify the correlation of the infrared excess IRX on the UV-continuum slope β_{UV} and stellar mass. Our results are most consistent with an SMC attenuation curve for intrinsic UV-slopes $\beta_{UV,intr}$ of -2.63 and most consistent with an attenuation curve in-between SMC and Calzetti for $\beta_{UV,intr}$ slopes of -2.23, assuming a dust temperature T_d of 50 K. Our fiducial IRX-stellar mass results at $z \sim$ 7-8 are consistent with marginal evolution from $z \sim 0$. We then show how both results depend on T_d. For our six dust-detected sources, we estimate their dust masses and find that they are consistent with dust production from SNe if the dust destruction is low (<90%). Finally we determine the contribution of dust-obscured star formation to the star formation rate density for UV luminous ($H<-21.5$ mag: $\gtrsim 1.7L^*_{UV}$) $z \sim$ 7-8 galaxies, finding that the total SFR density at $z \sim 7$ and $z \sim 8$ from bright galaxies is $0.20^{+0.10}_{-0.10}$ dex and $0.23^{+0.06}_{-0.09}$ dex higher, respectively, i.e. $\sim\frac{1}{3}$ of the star formation in $\gtrsim 1.7L^*_{UV}$ galaxies at $z \sim$ 7-8 is obscured by dust.

Schouws, Stefanon, Bouwens, Smit, Hodge, Labbé, Algera,
Boogaard, Carniani, Fudamoto, Holwerda, Illingworth,
Maiolino, Maseda, Oesch, and van der Werf
ApJ, 928, 31 (2022)

2.1 INTRODUCTION

One major uncertainty in our understanding of galaxy formation during the Reionization Epoch concerns the role of early dust build-up. Deep surveys in the rest-frame UV with both ground and space-based facilities have enabled the identification of large samples of galaxies at $z > 2$ and measurement of their UV-based star formation rates up to redshift $z \sim 11$ (e.g., Bouwens et al. 2011, 2014, 2015, 2016a, 2017; Ellis et al. 2012; Laporte et al. 2012; McLure et al. 2013; Schenker et al. 2013; Finkelstein et al. 2015; Kawamata et al. 2018; Oesch et al. 2014, 2015, 2018; McLeod et al. 2016). The rest-frame UV view only accounts for unobscured star formation and could be significantly impacted by the presence of dust in galaxies. Fortunately, accurate measurements of the dust-obscured star formation rates in galaxies to $z < 3$ have been available for the past ten years, thanks to deep and wide-field far-infrared (FIR) observations from *Herschel* and *Spitzer* (Reddy et al. 2006; Daddi et al. 2007; Magnelli et al. 2009, 2013, 2020; Karim et al. 2011; Cucciati et al. 2012; Schreiber et al. 2015; Álvarez-Márquez et al. 2016).

Less is known however about star formation in $z > 3$ galaxies that might be obscured by dust (e.g., Bouwens et al. 2016b; Dunlop et al. 2016; Casey et al. 2018; Wang et al. 2019; Williams et al. 2019). Because of the limited sensitivity and increasing source confusion suffered by *Herschel* and *Spitzer*, the obscured star formation in $z > 3$ galaxies could initially only be studied in the most luminous systems (e.g. Riechers et al. 2013; Oteo et al. 2016; Marrone et al. 2018). Consequently, studies of the star formation rate density at $z > 3$ often account for the impact of obscured star formation based on the UV light alone. Especially useful in this regard has been the empirical relation between the UV continuum slope β_{UV} and the infrared excess (IRX=L_{IR}/L_{UV}). In the local universe, the IRX has been found to show a good correlation with β_{UV} for star forming galaxies (Meurer et al. 1999; Takeuchi et al. 2010; Overzier et al. 2010; Casey et al. 2014). Moreover, this same correlation seems to hold up to at least $z \sim 3$ (Reddy et al. 2006, 2010, 2011; Daddi et al. 2009; Overzier et al. 2010; Sklias et al. 2014; Pannella et al. 2015; Bouwens et al. 2016b; Álvarez-Márquez et al. 2016; Whitaker et al. 2017; Fudamoto et al. 2017, 2019a; Fudamoto et al. 2020; McLure et al. 2018).

The availability of new observations from sub-millimeter facilities like the Atacama Large Millimeter/submillimeter Array (ALMA) and the NOrthern Extended Millimeter Array (NOEMA) which have much better sensitivity and resolution than previous facilities, have had an especially important impact on studies of obscured star formation and dust in $z > 3$ galaxies (e.g. Hodge & da Cunha 2020). Most importantly, these facilities have enabled the detection of obscured star formation in normal main sequence star forming galaxies at $z >3$ by utilizing deep field observations (Aravena et al. 2016, 2020; Bouwens et al. 2016b; Bouwens et al. 2020; Dunlop et al. 2016; McLure et al. 2013) and targeted studies (e.g. Capak et al. 2015; Willott et al. 2015; Knudsen et al. 2017; Laporte et al. 2017; Bowler et al. 2018; Hashimoto et al. 2019; Tamura et al. 2019; Fudamoto et al. 2020), but the majority of observed high redshift sources remain undetected in the dust continuum (e.g Maiolino et al. 2015; Bouwens et al. 2016b; Carniani et al. 2017, 2018; Smit et al. 2018; Bowler et al. 2018; Matthee et al. 2017, 2019; Hashimoto et al. 2018). This indicates that star formation in normal $z > 3$ galaxies may be less obscured than in the local universe, especially in normal and small galaxies, and previous corrections to the UV derived star formation rates to determine the cosmic star formation history may be overestimated (e.g. Bouwens et al. 2016b; Capak et al. 2015; Willott et al. 2015; Barisic et al. 2017; Faisst et al. 2017, 2020; Fudamoto et al. 2017, 2019a,b). This is corroborated by recent findings from Fudamoto et al. (2020), who find that the infrared excess of $z \sim$ 4-6 galaxies from ALPINE (Le Fèvre et al. 2020) can be much better explained with a steeper attenuation curve like SMC than with greyer attenuation curves like Calzetti.

Despite the significant amount of progress in detecting obscured star formation in galaxies to redshifts $z \sim 6.5$, much less is known about the dust properties and obscured star formation rates of galaxies at $z > 6.5$, with only 4 dust-continuum detections thus far identified in normal star-forming galaxies at $z \sim$ 7-8 (Watson et al. 2015; Knudsen et al. 2017; Laporte et al. 2017; Bowler et al. 2018; Hashimoto et al. 2019; Tamura et al. 2019). Additionally, there have also been a modest number of prominent dust continuum detections in more extreme ULIRG-type (Ultra-Luminous InfraRed Galaxy: defined as $L_{IR} > 10^{12} L_\odot$) sources (Marrone et al. 2018) and QSOs at $z > 6.5$ (Venemans et al. 2012, 2015a,b, 2017, 2018; Bañados et al. 2015; Mazzucchelli et al. 2017).

Further insight can be obtained into the dust properties of luminous $z > 6$ galaxies by increasing the number of such galaxies targeted with sensitive dust-continuum observations. In this spirit, we successfully proposed for ALMA continuum observations on a significant sample of luminous $z \sim 8$ galaxies to study the dust-continuum emission from luminous high-redshift galaxies. In addition, we also obtained sensitive ALMA-continuum observations on seven other bright $z \sim 7$ galaxies as part of two other programs aimed at probing the 157.74μm [CII] line (hereafter $[CII]_{158\mu m}$). Eight of these galaxies were identified as part of the Stefanon et al. (2017, 2019) study of bright star-forming galaxies at $z \gtrsim 8$ in the COSMOS/UltraVISTA field, while the $z \sim 7$ galaxies were primarily part of a similar selection of bright galaxies at $z \sim 7$ (Schouws et al. *in prep*). Focus on the brightest and most massive galaxies in the early universe is especially promising for the study of obscured star formation and dust, given the prevalence of dust in such galaxies at lower redshift (e.g., Hodge & da Cunha 2020), and the observability of such sources with ALMA and NOEMA.

In this paper, we make use of these new ALMA continuum observations to characterize the dust properties of some of the most massive galaxies in the $z \sim$ 7-8 universe. Our new observations significantly add to the ALMA continuum observations currently available for galaxies at $z > 6$, allowing us to quantify in much more detail both the dust emission and obscured star formation in these massive sources. In addition, the new observations allow us to constrain the dust attenuation law for high-redshift sources more accurately and increase the sample of sources where we have estimates of dust masses, which is essential for studying the build-up of dust early after the Big Bang.

The layout of this paper is as follows. In §2, we describe both the selection of our sources and the ALMA observations. In §3, we present our new ALMA-continuum results and then combine these results with the available UV observations to derive the IR luminosities and infrared excesses for individual sources. In §4, we use our new measurements to constrain the form of IRX-M_* and IRX-β relations, look at spatial offsets between UV and dust-continuum light, and consider dust build-up in galaxies to $z \sim 7$. In §5, we briefly discuss our results, and finally, in §6, we summarize our conclusions. Throughout this paper we assume a standard cosmology with $H_0 = 70$ km s^{-1} Mpc^{-1}, $\Omega_m = 0.3$ and $\Omega_\Lambda = 0.7$. Magnitudes are presented in the AB system (Oke & Gunn 1983). For star formation rates and stellar masses we adopt a Chabrier IMF (Chabrier 2003).

Table 2.1. Observational parameters of the ALMA observations

Source Name	RA	DEC	Beamwidth[a] (arcsec)	Integration time[b] (min.)	Achieved Sensitivity (μJy: 1σ)	Central Frequency (GHz)	Project Code
			$z \sim 7$ Sample				
UVISTA-Z-001	10:00:43.36	02:37:51.3	1.47" ×1.21"	78.36	17.9	234.0	2018.1.00085.S
UVISTA-Z-007	09:58:46.21	02:28:45.8	1.40" ×1.19"	65.52	17.4	245.7	2018.1.00085.S
UVISTA-Z-009	10:01:52.30	02:25:42.3	1.38" ×1.20"	65.52	19.0	245.7	2018.1.00085.S
UVISTA-Z-010	10:00:28.12	01:47:54.5	1.44" ×1.18"	78.36	14.7	234.0	2018.1.00085.S
UVISTA-Z-013	09:59:19.35	02:46:41.3	1.45" ×1.18"	78.36	15.0	234.0	2018.1.00085.S
UVISTA-Z-019	10:00:29.89	01:46:46.4	1.39" ×1.18"	65.52	18.0	245.7	2018.1.00085.S
COS-3018	10:00:30.19	02:15:59.8	1.63" ×1.49" [c]	766.08	7.0	233.5	2017.1.00604.S
			$z \sim 8$ Sample				
UVISTA-Y-001	09:57:47.90	02:20:43.7	1.17" ×0.96"	37.50	13.4	203.1	2018.1.00236.S
UVISTA-Y-002	10:02:12.56	02:30:45.7	1.17" ×0.96"	37.50	13.3	203.1	2018.1.00236.S
UVISTA-Y-003	10:00:32.32	01:44:31.3	0.60" ×0.52"	33.26	19.1	230.4	2017.1.01217.S
UVISTA-Y-004	10:00:58.49	01:49:56.0	1.03" ×0.94"	91.73	9.3	231.3	2017.1.01217.S & 2018.A.00022.S
UVISTA-Y-005	10:00:31.89	01:57:50.2	1.17" ×0.96"	37.50	12.9	203.1	2018.1.00236.S
UVISTA-Y-006[f]	10:00:12.51	02:03:00.5	1.17" ×0.96"	37.50	13.2	203.1	2018.1.00236.S
UVISTA-Y-007[d]	09:59:02.57	02:38:06.1	0.60" ×0.53"	34.78	17.9	230.4	2017.1.01217.S
UVISTA-Y-009[ef]	09:59:09.62	02:45:09.7	0.60" ×0.53"	34.78	17.9	230.4	2017.1.01217.S

NOTE— [a]Beamsize as measured in the naturally weighted continuum images. [b]Corresponds to the total integration time in case of multiple tunings. In total, 25.7 hours of integration time on source is included in this analysis. [c]For this dataset we use a 1.5 arcsecond tapered continuum image, the full ~0.25 arcsecond resolution data will be presented in Smit et al. (*in prep*). [d]Source name in ALMA observations is Y8. [e]Source name in ALMA observations is Y10. [f]UVISTA-Y-006 and UVISTA-Y-009 are estimated to be magnified by a factor ~0.27 dex and ~0.29 dex respectively due to lensing from foreground galaxies (Stefanon et al. 2019). Given the large uncertainty in the lensing magnification factor, the luminosities and fluxes for these sources are not corrected for lensing.

2.2 TARGETS AND ALMA OBSERVATIONS

The purpose of this Section is to provide a brief summary of the deep ALMA continuum observations and bright $z \sim$ 7-8 targets we analyze in this study as part of five separate ALMA programs. A summary of the observations we describe in this Section is provided in Table 2.1.

2.2.1 *ALMA Continuum Observations of Bright $z \sim 7$ Galaxies*

As part of an effort to better characterize the physical properties of very luminous galaxies at $z \sim 7$, we used an ALMA cycle-6 program (2018.1.00085.S: P.I. Schouws) to observe six luminous $z \sim 7$ galaxies. The observations were designed to use spectral scans to search for the $[CII]_{158\mu m}$ line, while simultaneously probing the dust-continuum emission from sources. This paper focuses on the dust-continuum properties of these sources, while we defer the discussion on the $[CII]_{158\mu m}$ emission to a companion study (Schouws et al. (*in prep.*)). That paper also details the manner in which six bright $z \sim 7$ sources were selected for targeting and our identification of [CII] (SNR>9) in three of them.

The six sources in the program were identified using the very deep optical, near-IR, and *Spitzer*/IRAC observations obtained over the 2 deg^2 COSMOS/UltraVISTA field from significant survey programs within COSMOS (Scoville et al. 2007; Capak et al. 2007), CFHT-LS (Erben et al. 2009; Hildebrandt et al. 2009), UltraVISTA (McCracken et al. 2012), SPLASH (Capak et al. 2013), and SMUVS (Caputi et al. 2017; Ashby et al. 2018).

Each of the sources was selected to show a strong break across the Y and z filters ($z - Y > 2$ mag), show blue UV-continuum slopes, and show moderately blue or red *Spitzer*/IRAC [3.6]-[4.5] colors, i.e., < -0.3 or ≥ 0.3. Significantly red or blue Spitzer/IRAC colors not only provide evidence for substantial $[OIII]_{5007Å}$+Hβ line emission in the sources (e.g., equivalent widths EW($[OIII]_{5007Å}$+Hβ)$\gtrsim$500Å Smit et al. (2015)), but also indicate to which IRAC band the line emission contributes. By combining this information with that available from the Lyman break, accurate redshift constraints can be derived $\Delta z \lesssim 0.15$ (see also Smit et al. 2015; Roberts-Borsani et al. 2016) on the six targeted galaxies, making it possible for us to efficiently scan for $[CII]_{158\mu m}$. A more extensive description of the source selection is included in Schouws et al. (*in prep.*).

All six targets were observed in band-6 as part of ALMA program #2018.1.00085.S using the most compact configuration for maximal sensitivity (C43-1: ∼1.3 arcseconds resolution). The spectral setup was chosen to enable a scan for $[CII]_{158\mu m}$ over essentially the full frequency range expected on the basis of our precise redshift constraints. We were able to execute this scan using just two separate tunings with three spectral windows each. The full bandwidth for each scan was therefore 10.75 GHz in total. Approximately 40 minutes were required in each tuning to reach a sensitivity of 0.25 mJy per 66 km/s, which was chosen to ensure detection of $[CII]_{158\mu m}$ based on previous studies (e.g., Smit et al. 2018). The precipitable water vapor during the executed observations ranged from 1.6 to 3.5 mm. We refer to Table 2.1 for a detailed overview of the parameters of our observations.

Additionally, we also utilize the sensitive, higher spatial resolution band-6 observations we obtained of $z = 6.853$ source COS-3018555981 (Smit et al. 2018) (hereafter abbreviated to COS-3018). The purpose of those observations was to characterize in detail the kinematics of a $z \sim 7$ galaxy with relatively luminous $[CII]_{158\mu m}$ line and to determine if the kinematics were more consistent with simple rotation or a merging system. COS-3018 was one of two $z \sim 6.8$ sources featured in Smit et al. (2018) and found to show prominent differential motion across the detected $[CII]_{158\mu m}$ profile. Thanks to the depth of the band-6 observations on this source, these observations can also used to characterize the IRX in this source.

In interpreting the ALMA results obtained for our $z \sim 7$ galaxy targets, it is worthwhile asking whether our selection criteria for our targets might bias our results. After all, our selection of $z \sim 7$ targets required that their $[OIII]_{5007Å}$+Hβ nebular emission lines be sufficiently strong to narrow the redshift likelihood distribution for sources. As we will discuss in Schouws et al. (*in prep*), the median source in our $z \sim 7$ selection only had a $[OIII]_{5007Å}$+Hβ EW of ∼1000Å. Since this is roughly consistent with the median EW (759^{+112}_{-113} Å) derived by Endsley et al. (2021) for the $z \sim 7$ population of luminous galaxies, we can conclude that our $z \sim 7$ results appear to be representative.

2.2.2 *ALMA Continuum Observations of Bright $z \sim 8$ Galaxies*

We additionally targeted the eight most luminous Lyman Break Galaxies at $z \sim 8$ in UltraVISTA to obtain sensitive continuum constraints on their far-IR emission and obscured star formation. The targeted sources were identified as part of a search for bright Lyman-break galaxies at $z \sim 8$ (Stefanon et al. 2017, 2019), where sources were required to have $Y - (J + H)/2$ colors redder than 0.75 mag, to show a blue UV-continuum slope redward of the Balmer break, and a low-probability of being a low-redshift galaxy based on SED fits.

The eight sources were targeted as part of two ALMA programs #2017.1.01217.S (P.I. Stefanon) and #2018.1.00236.S (P.I. Stefanon) and observed for ∼35 minutes each. To optimize the probability for detection for $[CII]_{158\mu m}$, we used band-6 to obtain continuum observations of those sources whose best-fit photometric redshifts were $z < 8$ and band-5 to obtain continuum observations for those whose best-fit redshifts were $z > 8$. As a result of the relatively large photometric redshift uncertainties on the Stefanon et al. (2019) $z \sim 8$ sources and the cost of pursuing spectral scans, we elected to use a single spectral setup to maximize the continuum sensitivity. We also obtained 58 minutes of follow-up observations (#2018.A.00022.S: P.I. Schouws) on one source from ALMA program #2017.1.01217, UVISTA-Y-004, in an effort to confirm a tentative 2.5σ dust-continuum detection of that source.

We note that two sources from in sample, UVISTA-Y-006 and UVISTA-Y-009, are estimated to be magnified by a factor ∼0.27 dex and ∼0.29 dex

Table 2.2. Physical and Measured Characteristics of the Bright $z \sim$ 7-8 Galaxies Targeted with ALMA Observations

Sourcename	Redshift[†]	m_{UV}	$\beta^{\ddagger}_{UV}$	L_{UV} ($10^{11} L_{\odot}$)	$\log(M_*)^{\ddagger}$ ($M_{\odot}$)	$S_\nu{}^b$ (μJy)	$L_{IR}{}^d$ ($10^{11} L_{\odot}$)
UVISTA-Z-001	7.0611[a]	23.9 ±0.1	$-1.88^{+0.22}_{-0.07}$	$2.9^{+0.1}_{-0.1}$	$9.58^{+0.09}_{-0.35}$	104^{+43}_{-43}	$5.0^{+2.1}_{-2.1}$
UVISTA-Z-007	6.7498[a]	24.5 ±0.1	$-2.02^{+0.22}_{-0.22}$	$1.5^{+0.2}_{-0.2}$	$9.57^{+0.35}_{-0.44}$	$<$ 52.2	$<$ 2.2
UVISTA-Z-009	$6.90^{+0.10}_{-0.06}$	24.6 ±0.1	$-1.88^{+0.21}_{-0.51}$	$1.6^{+0.2}_{-0.2}$	$9.40^{+0.32}_{-0.29}$	$<$ 57.0	$<$ 2.4
UVISTA-Z-010	$7.07^{+0.09}_{-0.07}$	24.6 ±0.1	$-2.39^{+0.35}_{-0.28}$	$1.1^{+0.2}_{-0.2}$	$8.88^{+0.28}_{-0.09}$	$<$ 44.1	$<$ 2.1
UVISTA-Z-013	$7.02^{+0.06}_{-0.02}$	24.9 ±0.2	$-2.24^{+0.36}_{-0.15}$	$1.4^{+0.4}_{-0.3}$	$10.72^{+0.03}_{-0.10}$	$<$ 45.0	$<$ 2.2
UVISTA-Z-019	6.7544[a]	25.1 ±0.2	$-1.51^{+0.29}_{-0.15}$	$1.0^{+0.1}_{-0.1}$	$9.51^{+0.19}_{-0.18}$	66^{+23}_{-23}	$2.7^{+0.9}_{-0.9}$
COS-3018	6.8540[a]	24.9 ±0.1	$-1.22^{+0.51}_{-0.51}$	$1.3^{+0.1}_{-0.1}$	$9.14^{+0.18}_{-0.06}$	65^{+13}_{-13}	$3.0^{+0.6}_{-0.6}$
UVISTA-Y-001	$8.53^{+0.53}_{-0.62}$	24.8 ±0.1	$-1.37^{+0.36}_{-0.44}$	$2.1^{+0.3}_{-0.3}$	$10.0^{+0.9}_{-0.4}$	73^{+20}_{-20}	$3.5^{+1.0}_{-1.0}$
UVISTA-Y-002	$8.21^{+0.50}_{-0.49}$	24.8 ±0.2	$-2.60^{+0.58}_{-0.51}$	$1.9^{+0.4}_{-0.3}$	$9.0^{+0.3}_{-1.2}$	$<$ 39.9	$<$ 2.3
UVISTA-Y-003	$7.62^{+0.14}_{-0.28}$	25.0 ±0.1	$-1.88^{+0.80}_{-0.73}$	$1.3^{+0.2}_{-0.2}$	$9.9^{+0.6}_{-0.3}$	241^{+30}_{-30}	$10.7^{+1.3}_{-1.3}$
UVISTA-Y-004	$7.42^{+0.19}_{-0.20}$	24.9 ±0.2	$-1.80^{+0.29}_{-0.29}$	$1.5^{+0.4}_{-0.3}$	$9.9^{+0.5}_{-0.2}$	65^{+17}_{-17}	$2.9^{+0.8}_{-0.8}$
UVISTA-Y-005	$8.60^{+0.58}_{-0.65}$	24.9 ±0.2	$-1.59^{+1.24}_{-0.58}$	$1.8^{+0.5}_{-0.4}$	$9.0^{+0.4}_{-1.1}$	$<$ 38.7	$<$ 2.5
UVISTA-Y-006	$8.32^{+0.66}_{-0.92}$	25.3 ±0.3	$-1.70^{+0.70}_{-0.80}$	$1.2^{+0.3}_{-0.3}$	$9.7^{+1.1}_{-0.5}$	$<$ 39.6	$<$ 2.5
UVISTA-Y-007	$8.47^{+0.73}_{-0.72}$	25.5 ±0.3	$-2.00^{+0.70}_{-0.50}$	$1.1^{+0.4}_{-0.3}$	—[e]	$<$ 53.7	$<$ 2.5
UVISTA-Y-009	$7.69^{+0.99}_{-0.71}$	25.4 ±0.3	$-2.60^{+0.90}_{-0.60}$	$1.0^{+0.4}_{-0.3}$	—[e]	$<$ 53.6	$<$ 2.5
Stack at z∼7[c]	$6.95^{+0.07}_{-0.08}$	24.6 ±0.2	$-1.99^{+0.25}_{-0.25}$	$1.5^{+0.2}_{-0.2}$	$9.6^{+0.6}_{-0.4}$	33^{+21}_{-24}	$1.4^{+1.0}_{-1.0}$
Stack at z∼8[c]	$7.87^{+0.20}_{-0.23}$	25.1 ±0.2	$-2.13^{+0.21}_{-0.21}$	$1.5^{+0.1}_{-0.1}$	$9.3^{+0.5}_{-0.9}$	27^{+14}_{-12}	$1.3^{+0.6}_{-0.5}$
Stack of non-detections	$7.72^{+0.40}_{-0.42}$	24.9 ±0.2	$-2.16^{+0.22}_{-0.22}$	$1.4^{+0.3}_{-0.3}$	$9.2^{+0.3}_{-0.7}$	$<$ 23.5	$<$ 1.2

Note—[†]Quoted redshifts are based on the photometric redshift estimates given in Schouws et al. (*in prep*) or Stefanon et al. (2019). [‡]UV-continuum slopes β_{UV} and stellar masses are from Stefanon et al. (2019) or use the methodology described in Stefanon et al. (2019) for these estimates, assuming a 0.2 $Z_{\odot}$ metallicity, a constant star formation prescription, and a Calzetti et al. (2000) dust law. [a]Spectroscopic redshifts are from the $[CII]_{158\mu m}$ line (Schouws et al. *in prep* and Smit et al. 2018 for COS-3018). [b]Integrated flux derived with UVMULTIFIT (not corrected for CMB effects: see §2.3.1). Upper limits on non detections are 3σ. [c]Stack fluxes and errors are determined using a bootstrapping analysis (see section 2.3.2). [d]Total infrared luminosity integrated from 8-1000μm assuming a modified black body SED with a dust temperature of 50 K and a dust emissivity index β_{dust}=1.6 after correcting for CMB effects (see §2.3.1). [e]Due to the challenges in measuring the flux of these sources in the *Spitzer*/IRAC data caused by confusion from bright neighbouring sources (Stefanon et al. 2019), no stellar masses are estimated for these sources.

respectively due to lensing from foreground galaxies (Stefanon et al. 2019). However, the exact value of the magnification factor is relatively uncertain and model dependent. We also note that lensing does not impact our measurement of IRX because this is defined as a ratio of two luminosities which are magnified by the same factor. The impact of differential lensing is likely minimal due to the minimal offsets we observe between the dust-continuum and rest-frame UV emission (typically <0.2"; see section 2.3.3), which are much smaller than the distances to the lensing galaxies (>3"; Stefanon et al. (2019)). Moreover, both sources are not detected in the continuum and therefore do not impact our discussion on the mechanisms of dust build-up (see section 2.3 and 2.4). We therefore do not explicitly correct the fluxes and luminosities of these sources to account for the magnification.

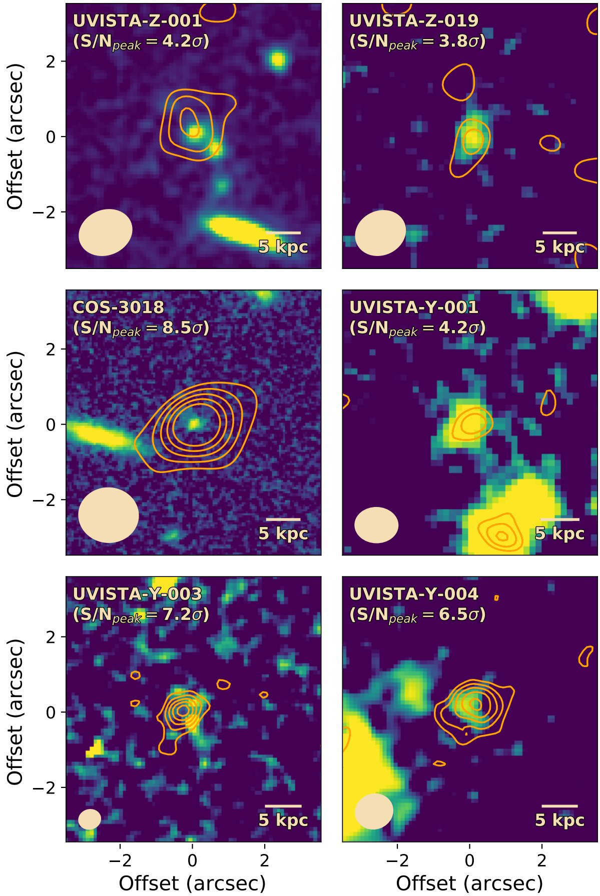

Figure 2.1. An overlay of band-6 dust-continuum observations (1.2μm) with ALMA on the available near-IR imaging observations for 6 $z \sim$ 7-8 sources detected in the dust continuum. For UVISTA-Z-001, UVISTA-Y-003 and COS-3018, near-IR imaging observations are from 1-orbit HST F140W, F160W, and F160W exposures, respectively, and for the remaining sources, from stacked J+H+K_s imaging from UltraVISTA. Contours are drawn at (2, 3, 4, 5, 6)$\times\sigma$ using the sensitivities from Table 2.1 (typically $\sigma \approx 15\mu$Jy beam^{-1}). The ALMA contours presented here are from the natural weighted imaging except for COS-3018 where a 1.5" taper is used (see Section 2.2.3). The synthesized beam for the dust-continuum observations is indicated in the lower-left corner of each panel. The significance of the dust detections for each source is stated below the source-name (peak-S/N). In Figure 2.12, we show the continuum results for sources lacking a clear detection.

2.2.3 *ALMA Data Reduction*

The ALMA data were reduced and calibrated using CASA version 5.4.1 following the standard ALMA pipeline procedures. The imaging was performed using the TCLEAN task in CASA, applying natural weighting to maximize signal to noise. Any channels containing line emission from the $[CII]_{158\mu m}$ line were carefully excluded from the continuum imaging. All significant continuum sources in the field were masked and cleaned conservatively to 3σ. A range of *(u,v)*-tapers from 1.0 to 2.0 arcseconds were applied, but it was found that the images without any *(u,v)*-tapering had the highest SNR. Therefore we use the setup without any *(u,v)*-tapering for the remainder of this paper unless specified otherwise. We reduce the observations for COS-3018 in a similar way except applying a 1.5 arcsecond taper to the visibility data; the full resolution results will be presented in Smit et al. (*in prep*).

To examine in more detail the relative morphologies of galaxies in terms of their far-IR dust-continuum emission and in the rest-frame UV, we also re-imaged the sources using Briggs-weighting with robustness parameter 0.3, where a robustness parameter of -2 corresponds to uniform weighting (which maximizes the spatial resolution of the continuum signal) and 2 to natural weighting (which maximizes the S/N). Our choice of 0.3 for the robustness parameter was made as a compromise between resolution and S/N. In particular, for the most luminous source (UVISTA-Y-003) we used Briggs weighting to decrease the size of our beam from 0.60"$\times$0.52" beam to a 0.45"$\times$0.37". This is useful to constrain the physical alignment between the UV and FIR, which will be further discussed in Section 2.3.3.

2.2.4 *Near-IR Imaging Observations*

In interpreting the dust-continuum observations for our $z \sim$ 7-8 sources, it is helpful to compare against the sensitive imaging observations that are available for these targets in the near-IR. All 14 of our targets have available sensitive $YJHK_s$ imaging observations from the UltraVISTA program, albeit with limited (FWHM$_{PSF}$ $\sim$0.8$''$) spatial resolution. For a few sources, higher spatial resolution imaging observations exist from HST, in particular for UVISTA-Z-001 (1-orbit in F140W: Bowler et al. 2017), UVISTA-Y-003 (1-orbit in F160W, DASH: Momcheva et al. 2016) and COS-3018 (1.3-orbits in F160W, CANDELS: Grogin et al. 2011).

To ensure good registration of the available near-IR observations with our new ALMA-continuum observations, we took advantage of the high astrometric accuracy of the GAIA DR2 catalog (Gaia Collaboration et al. 2018) to make minor (<0.1") adjustments to the astrometry of the near-infrared imaging observations available for the COSMOS field from UltraVISTA or HST (if available). As a further check on the astrometric accuracy of the near-IR imaging data, we compared the position of eight lower-redshift dust-continuum detections in our ALMA data with their position in the near-IR imaging data and found good agreement (<0.2").

2.3 RESULTS

2.3.1 *Individual Detections*

The new ALMA observations we have obtained on a significant sample of 15 bright $z \sim$ 7-8 galaxies provide us with essential new information on the obscured star formation and dust-continuum emission in these sources.

Using naturally-weighted reductions of the continuum observations, we performed a systematic search for 3σ peaks within 1" of the rest-frame UV positions of our 15 targeted sources. We find a significant dust continuum detection for six of the sources, as is illustrated in Figure 2.1, which shows the 2, 3, 4, 5, 6σ dust-continuum contours overlaid on the rest-frame UV emission. The continuum detections show <0.5" spatial offsets from the UV positions. We note that allowing for large spatial offsets (e.g., to 3") does not increase the number of detected sources.

To measure continuum fluxes for the detected sources, the complex visibilities were fitted using UVMULTIFIT (Martí-Vidal et al. 2014), applying a 2D Gaussian model with a single component. By fitting in the *(u,v)*-plane, the results are independent of the imaging parameters. The fluxes measured in this way are consistent with measurements in the image plane and measured fluxes range from 75^{+6}_{-10} μJy to 302^{+45}_{-35} μJy, comparable with previous studies at $z \gtrsim 7$ (Watson et al. 2015; Willott et al. 2015; Laporte et al. 2017; Knudsen et al. 2017; Bowler et al. 2018; Tamura et al. 2019; Hashimoto et al. 2019). In the case of non-detections, we provide 3σ upper limits derived from the noise measured in the natural weighted imaging. For convenience, we summarize the results in Table 2.2. The fluxes in this Table have not been corrected for effects arising from the Cosmic Microwave Background (CMB). For derived quantities (L_{IR}, M_{dust} etc.) we correct the measured fluxes for the reduced contrast due to the higher temperature of the CMB at high redshifts using Eq. (18) of da Cunha et al. (2013).

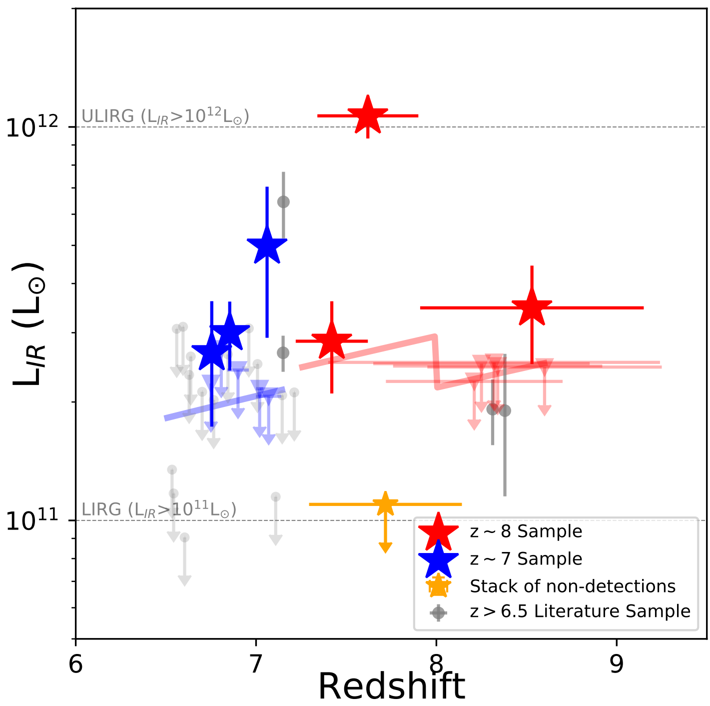

Figure 2.2. IR luminosities and redshifts for $z \sim 7$ and $z \sim 8$ galaxies detected in ALMA continuum observations analyzed here (*blue and red stars*, respectively). The redshifts at which sources are shown are either from detected $[CII]_{158\mu m}$ lines (Schouws et al. *in prep*) or from the computed photometric redshifts. The blue and red plotted downward pointing triangles correspond to 3σ upper limits on the IR luminosities for the four $z \sim 7$ and five $z \sim 8$ sources undetected in our ALMA observations. Also shown are previous dust-continuum detections from the literature at $z > 6$ (*solid grey circles*: Watson et al. 2015; Laporte et al. 2017; Bowler et al. 2018; Tamura et al. 2019)) and upper limits (*grey arrows*: Bradač et al. 2017; Ota et al. 2014; Matthee et al. 2017, 2019; Pentericci et al. 2016; Maiolino et al. 2015; Hashimoto et al. 2018). The thick blue and red lines show the 3σ-limiting IR luminosities we probe given the integration times for our ALMA observations.

For comparison with other results in the literature and lower redshift studies, it is convenient to estimate the total infrared luminosities for the sources in our sample. Following previous studies, we adopt a modified single-temperature black body dust spectral energy distribution and integrate the SED between 8-1000μm to calculate L_{IR}. For the dust emissivity

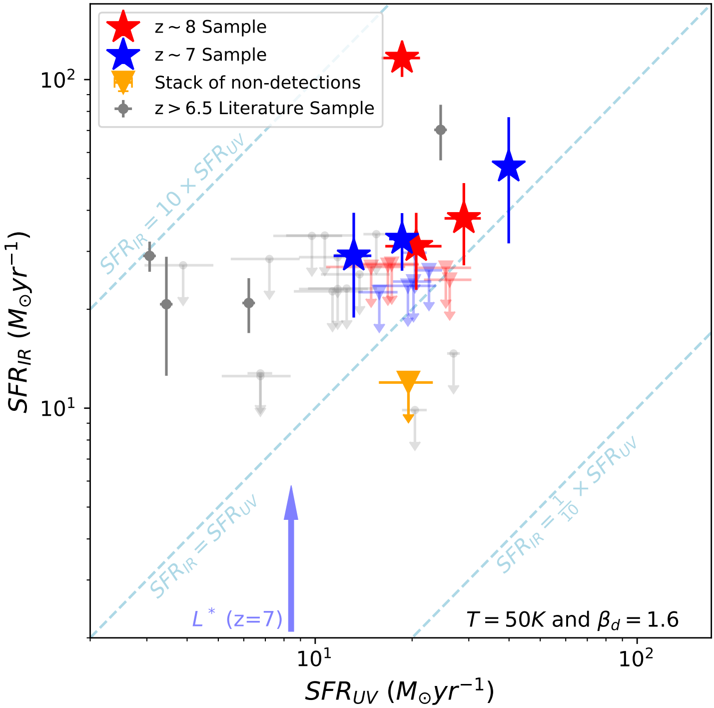

Figure 2.3. A comparison of the un-obscured (SFR_{UV}) and obscured (SFR_{IR}) star formation rates inferred from our observations of luminous $z \sim 7$ and $z \sim 8$ galaxies (*blue and red colored stars and upper limits*, respectively). Previous results for $z > 6.5$ galaxies are shown with the gray symbols and upper limits (see Figure 2.2 for references). Upper limits are 3σ. For reference, the typical *UV* star formation rate of L* galaxies at $z = 7$ (Bouwens et al. 2015) is indicated with the blue arrow. For the *UV* luminous sources we analyzed here, the obscured SFRs appear to be comparable to the unobscured SFRs.

index we assume β_d=1.6, which is the best-fitting value for local infrared luminous galaxies (Casey et al. 2014).

Dust temperatures in typical star-forming galaxies in the local universe are around ∼35 K (Casey et al. 2014; Rémy-Ruyer et al. 2015), but it has been shown using stacking of *Herschel* observations that dust temperatures increase with redshift (Béthermin et al. 2015; Schreiber et al. 2015, 2018; Faisst et al. 2017, 2020). Other observational (e.g., Bouwens et al. 2016b; Coppin et al. 2014; Knudsen et al. 2017; Capak et al. 2015; Watson et al.

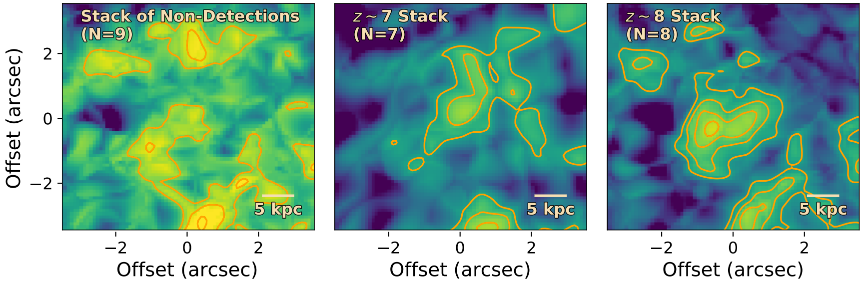

Figure 2.4. *Left:* Median stacking of all non-detections (number of sources in the stack; N=9) does not result in a significant detection of the dust continuum. Contours are drawn at (1, 2, 3, 4, 5, 6)$\times\sigma$ where $\sigma = 7.8\mu$Jy beam^{-1}. *Middle and Right:* Median stacks combining the ALMA observations for all $z{\sim}7$ (middle, N=7) and $z{\sim}8$ (right, N=8) galaxies from our sample (including detections and non-detections) to study the typical properties of our sample. These stacks are marginally detected at 3.0σ (σ = 8.5μJy beam^{-1}) and 3.8σ ($\sigma = 6.9\mu$Jy beam^{-1}) respectively (peak-SNR). See Section 2.3.2 and 2.4.2 for a discussion of these results.

2015; Bouwens et al. 2020) and theoretical (Behrens et al. 2018; Liang et al. 2019; Sommovigo et al. 2021) studies also suggest such a trend. We note however that there seems to be a large scatter in the dust temperatures at high redshift, with evidence for very hot (T>80 K) (Bakx et al. 2020; Laporte et al. 2019) and relatively cold temperatures (T∼25 K) (Harikane et al. 2020) in individual sources. We therefore adopt a dust temperature of 50 K for our analysis (this is the dust temperature after any CMB heating).

To put our dust continuum detections in context, we show the IR luminosities we have inferred for the sources in our samples against redshift in Figure 2.2 and then compare these detections with IR luminosities inferred for other dust-detected galaxies at $z > 6$. Interestingly enough, one of our $z > 7$ galaxies has an IR luminosity in excess of $10^{12}\ L_\odot$, which places the source in the ULIRG category and is the most IR-luminous galaxy known at $z > 7$. For context, we have also estimated the limiting luminosities to which we would have succeeded in detecting bright $z \sim 7$ and $z \sim 8$ galaxies, given the integration times for sources in the two samples.

We estimate SFR_{UV} and SFR_{IR} for sources following Madau & Dickinson (2014), with conversion factors $SFR_{UV} = \kappa_{UV} \cdot L_{UV}$ and $SFR_{IR} = \kappa_{IR} \cdot L_{IR}$ where $\kappa_{UV} = 2.5 \cdot 10^{-10} M_\odot yr^{-1} L_\odot^{-1}$ and $\kappa_{IR} = 1.73 \cdot 10^{-10} M_\odot yr^{-1} L_\odot^{-1}$ and we convert from a Salpeter IMF to Chabrier IMF with $SFR_{Cha} = 0.63 \cdot SFR_{Sal}$ (Madau & Dickinson 2014). We compare these SFR estimates for our sources to previous detections and

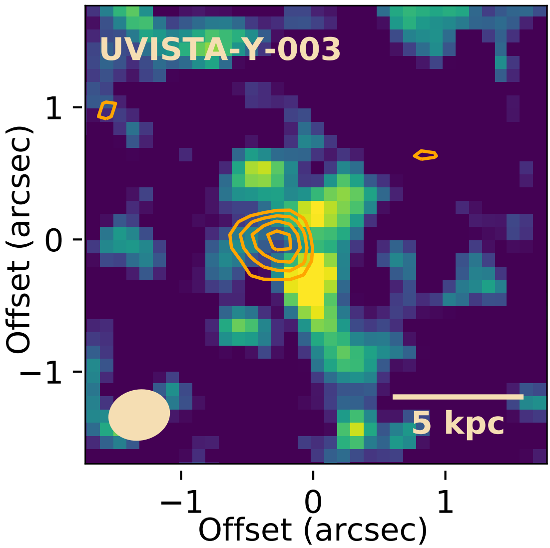

Figure 2.5. Higher spatial resolution image of the dust-continuum emission from the bright $z \sim 8$ galaxy UVISTA-Y-003 shown relative to the rest-frame UV imaging we have of the source with HST in the F160W band (1.6μm; ∼1900Å rest-frame) (3.5”×3.5” FOV). The presented imaging of UVISTA-Y-003 used a Briggs weighting with robustness parameter 0.3 to bring out the high-spatial resolution structure (Beam: 0.45”×0.37”). Contours are drawn at (2.0, 2.5, 3.0, 3.5)$\times\sigma$ where $\sigma = 23\mu$Jy. Interestingly enough, the UV-continuum emission from UVISTA-Y-003 appears to be divided into three separate clumps (see Stefanon et al. 2019). All of these rest-frame UV clumps show a clear spatial offset from the dust-continuum emission. It therefore seems very likely that there is a high star-formation region in UVISTA-Y-003, which is entirely obscured in the rest-frame UV, much like one commonly observes in ULIRGs at both $z \sim 0$ and $z \sim$ 1-3. It is unclear whether the multiple rest-frame UV components are indicative of merger activity or clumpy star forming regions.

upper limits at $z >$6.5 (Ota et al. 2014; Maiolino et al. 2015; Watson et al. 2015; Pentericci et al. 2016; Inoue et al. 2016; Knudsen et al. 2017; Bradač et al. 2017; Laporte et al. 2017; Bowler et al. 2018; Carniani et al. 2018; Hashimoto et al. 2018; Smit et al. 2018; Hashimoto et al. 2019; Tamura et al. 2019; Matthee et al. 2019) in Figure 2.3.

Interestingly enough, we find that the obscured star formation rates SFR_{IR} for sources are fairly similar to the unobscured star formation rates SFR_{UV}, in cases where the dust is detected. This is consistent with previous results in the literature which include a few prominent detections where $SFR_{IR} > SFR_{UV}$ (Knudsen et al. 2017; Laporte et al. 2017; Bowler et al. 2018; Hashimoto et al. 2019; Tamura et al. 2019) and many sources which lack prominent dust detections and $SFR_{IR} < SFR_{UV}$ (Ota et al. 2014; Maiolino et al. 2015; Watson et al. 2015; Pentericci et al. 2016; Matthee et al. 2017, 2019).

The infrared excess ($IRX = L_{IR}/L_{UV}$) is discussed in detail in sections 2.3.4 and 2.3.5, but we note here that for equal obscured and un-obscured SFRs ($SFR_{UV} = SFR_{IR}$), $\log_{10}(IRX)$=0.10. The derived $\log_{10}(IRX)$ increases or decreases by 1.0 for corresponding factors of 10 increases and decreases, respectively, in the obscured SFR relative to the un-obscured SFR.

2.3.2 *Stacking analysis*

Nine of the bright $z \sim$ 7-8 galaxies targeted by our ALMA programs are not individually detected in our continuum observations. To better characterize dust-continuum emission and obscured star formation in these sources, we can combine the continuum observations on these sources to obtain an average constraint through median-stacking. In addition to stacking those sources which are individually undetected, we repeat the stacking analysis using our entire $z \sim 7$ and $z \sim 8$ samples separately (i.e. both detections and non-detections), to constrain the properties of the hypothetical average galaxy in each sample.

For the stacking, we center sources according to their apparent position in the available HST or UltraVISTA rest-frame UV observations and coadd the ALMA continuum observations after tapering the continuum images with a 1-arcsec taper and and weighting the sources equally. We use tapered images to ensure that we capture all of the dust-continuum flux and to decrease the impact of both (1) the varying resolutions of the ALMA beam and (2) possible offsets between the dust continuum and UV emission on the stack. This is most relevant for the sources that were observed with a smaller beam, i.e., < 1".

The results of the stack of the nine non-detections are presented in both Table 2.2 and Figure 2.4 (*left panel*). No significant (<2σ where $\sigma = 11.8\mu$Jy) detection is found, which translates to a 3σ upper limit of $1.2{\times}10^{11}L_\odot$ (assuming T=50 K and β_d=1.6) on the IR luminosities of the undetected sources (the stack is also not detected when stacking using a noise-weighted mean). In Table 2.2 and Figure 2.4, we also present our stack results for our $z \sim 7$ and $z \sim 8$ samples. A stack of our $z \sim 7$ sample shows a 3.0σ detection and a stack of our $z \sim 8$ sample shows a 3.8σ detection. The mean IR luminosities we infer for bright $z \sim 7$ and $z \sim 8$ is $1.4^{+1.0}_{-1.0}\times10^{11}$ $L_{\odot}$ and $1.3^{+0.6}_{-0.5}\times10^{11}$ $L_{\odot}$, respectively. These results and those presented in Table 2.2 are derived based on a bootstrap resampling procedure, re-stacking sub-sets with replacement of our sources 10.000× and using the median peak flux measured in the stacked images. The uncertainties are based on the derived 68% spread in the stack results.

2.3.3 *Physical alignment between UV and FIR*

An important longstanding question regards the possible presence of spatial offsets between the dust-continuum emission and the rest-frame *UV* emission, as have frequently been found when considering IR luminous galaxies (Smail et al. 2014; Dunlop et al. 2016; Aravena et al. 2016; Laporte et al. 2019). Indeed, one would expect significant spatial offsets between rest-frame *UV* and *IR*-continuum emission in galaxies with a non-uniform dust covering fraction, especially when the optical depths become non-negligible. Such offsets can complicate the interpretation of the infrared excess (IRX) which assumes co-spatial emission and impact SED fitting codes that assume energy-balancing. Cormier et al. (2019) found evidence for such non-uniform covering fractions in local dwarf galaxies, which are often considered to be good analogues for high-redshift galaxies.

To investigate whether similar spatial offsets are found amongst the bright $z \sim$ 7-8 galaxies we observe with ALMA, we reimage the sources using Briggs weighting, as described in §2.3, with a beam of 0.45”×0.37” to examine sources at higher spatial resolution. Figure 2.5 illustrates how our most prominent dust-continuum detection UVISTA-Y-003 compares to the available rest-frame *UV* imaging from HST. We show the results for the remaining detections in appendix B (with the exception of COS-3018, which will be presented in a seperate paper (Smit et al. in prep.)).

For the majority of our sources, the *UV* and FIR continuum seem well aligned, with no major offsets between the *UV* and IR positions (typically smaller than <0.2”). However, UVISTA-Y-003 is a notable exception, showing an offset of ∼0.3” (∼2 kpc: see Figure 2.5). Furthermore, for this source the rest-frame *UV* emission seems to be divided into three separate clumps, each of which are offset from the dust emission. The *UV* clumps are discussed in more detail in Stefanon et al. (2019), who performed simulations to assess the robustness of the clumps and also confirmed high-z solutions for the clumps based on deblended photometry. Because of these offsets between the UV clumps and the dust continuum emission, it seems likely that there is a strongly star-forming region in UVISTA-Y-003, which is almost entirely obscured in the rest-frame UV, similar to what is observed in ULIRGs at $z \sim 0$ and $z \sim$ 1-3. It is unclear whether the three rest-frame UV components indicate the presence of merging activity or not. It is worth emphasizing the value of the high resolution space-based imaging for UVISTA-Y-003 in revealing both the clumpy nature of this source and the offset between the UV and dust continuum emission.

2.3.4 *Infrared Excess versus UV continuum Slope*

The measured infrared excess in galaxies ($IRX = L_{IR}/L_{UV}$) is well established to show a correlation with the UV-continuum slope β_{UV} (where $f_\lambda \propto \lambda^{\beta_{UV}}$). Meurer et al. (1999) showed that the correlation between the infrared excess and β_{UV} could be expressed as follows:

$$A_{1600} = \frac{dA_{UV}}{d\beta_{UV}} \cdot (\beta_{UV} - \beta_{UV,intr}) \tag{1}$$

$$IRX = 1.7 \cdot (10^{0.4 \cdot A_{1600}} - 1) \tag{2}$$

where $dA_{UV}/d\beta_{UV}$ expresses the steepness of the attenuation law, $\beta_{UV,intr}$ represents the unattenuated UV-continuum slope of star-forming galaxies and A_{1600} is the UV attenuation at 1600Å (Meurer et al. 1999). The IRX-β relation has been used as a constraint on the dust attenuation curve of galaxies. In the local universe, starburst galaxies have been shown (Meurer et al. 1999) to be well described by a Calzetti attenuation law (Calzetti et al. 2000), with $dA_{UV}/d\beta_{UV} = 1.99$ with $\beta_{UV,intr} = -2.23$. However, subsequent studies have found that some galaxies at higher redshifts do not follow Calzetti dust law and tend to favour a steeper attenuation curve, similar to the Small Magellanic Cloud (SMC) for which $dA_{UV}/d\beta_{UV} = 1.1$ and $\beta_{UV,intr}$=-2.23 (Reddy et al. 2006, 2018; Siana et al. 2008; Capak et al. 2015; Bouwens et al. 2016b; Barisic et al. 2017; Fudamoto et al. 2020).

In Figure 2.6, we present our measurements for the infrared excess versus the UV continuum slope (β_{UV}) for $z > 6.5$ sources with new measurements from our ALMA programs. For this Figure we assume that the rest-frame UV and dust-continuum emission are co-spatial, which is consistent with the lack of significant spatial offsets that can be constrain based on the current data as discussed in section 2.3.3. An exception is UVISTA-Y-

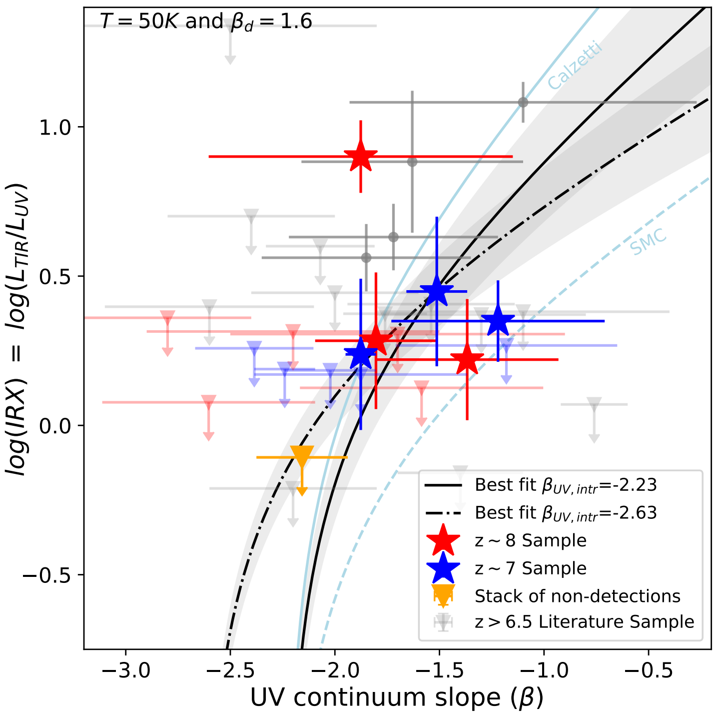

Figure 2.6. The inferred infrared excess of $z > 6.5$ galaxies against their UV-continuum slope β_{UV}. The three blue and three red stars show the infrared excesses inferred for the $z \sim 7$ and $z \sim 8$ galaxies that are detected in the dust continuum. The blue and red downward-pointing triangles show the 3σ upper limits on the inferred infrared excess in the eight $z \sim 7$ and $z \sim 8$ galaxies, respectively, lacking dust-continuum detections. The orange downward pointing triangle shows the 3σ upper limit we infer on the infrared excess stacking the individually undetected $z \sim$ 7-8 galaxies considered here. The grey circles and downward pointing triangles correspond to dust-continuum detections from the literature (see Figure 2.2 for references). For reference, the Calzetti and SMC IRX-β relations are shown with the cyan solid and dashed line, respectively (assuming an intrinsic UV-continuum slope β_{UV} of -2.23).

003, which seems to have a clumpy structure and we note that treating these clumps individually could significantly impact the interpretation of the IRX-β relation. While the current data are not ideal for constraining the properties of individual clumps, future high-resolution studies with ALMA (project code: 2021.1.01603.S, PI: Hodge) and JWST (Stefanon et al. 2021) of this source should enable a more detailed investigation of the individual clump properties.

In determining the best-fit value for $dA_{UV}/d\beta_{UV}$, we consider two different values for $\beta_{UV,intr}$: (1) $\beta_{UV,intr} = -2.23$, as used in modeling the IRX-β relation at $z \sim 0$ (Meurer et al. 1999) and (2) $\beta_{UV,intr} = -2.63$, as expected for a younger, lower-metallicity stellar population (Reddy et al. 2018) seen at higher redshift. For these two values of $\beta_{UV,intr}$ we determine the best-fit value for $dA_{UV}/d\beta_{UV}$ for a dust temperature of 50 K and dust emissivity index $\beta_d = 1.6$. For these fits we use the detections and non-detections described in this paper and a compilation from the literature ($M_{UV} < -21.5$; Maiolino et al. 2015; Pentericci et al. 2016; Inoue et al. 2016; Matthee et al. 2017, 2019; Hashimoto et al. 2019) assuming the same temperature (T=50K) for every source in the sample. We determine the best fit value and errors using a total least squares method which takes account of errors in both dependent and independent parameters. To account for non-detections we measure the maximum peak flux in a 1" radius around the UV-centroid position following Béthermin et al. (2020) and use those flux measurement in the minimalization routine. To test the robustness of our treatment of upper-limits we furthermore use a monte-carlo bootstrap method where we draw random flux measurements from the completeness function. We model the completeness with an error function with μ=4σ_{image} and σ=2σ_{image} where σ_{image} is the RMS measured from the continuum image, consistent with Béthermin et al. (2020) and Inami et al. *(in prep.)*. With these random flux measurements we repeat the fit 10.000× for each temperature. We find that both methods give consistent results within the uncertainties.

In Figure 2.7, we generalize the fit results presented in Figure 2.6 for $dA_{UV}/d\beta_{UV}$ to allow for an arbitrary dust temperature, given the current uncertainties in establishing the typical dust temperatures for $z > 6$ galaxies. The slopes ($dA_{UV}/d\beta_{UV}$) of the SMC and Calzetti attenuation curves are shown with horizontal blue lines. The error on the $dA_{UV}/d\beta_{UV}$ fit is derived from the formal uncertainties from the covariance matrix of the minimalization. On Figure 2.7, we indicate with a black arrow (and dotted vertical line) the fiducial dust temperature we assume 50 K, this is the luminosity-weighted dust temperature. We also indicate with an orange arrow the T_{dust} determination of 54.3±1.6 K that Bouwens et al. (2020) derived by extrapolating the results from Béthermin et al. (2015), Strandet et al. (2016), Knudsen et al. (2017), Schreiber et al. (2018), Hashimoto et al. (2019), Bakx et al. (2020), Béthermin et al. (2020), Harikane et al. (2020), and Faisst et al. (2020). Also shown in Figure 2.7 are where other high-redshift SED templates would lie (Béthermin et al. 2015; Schreiber et al. 2018; Faisst et al. 2020; Michałowski et al. 2010; Rossi et al. 2018), including Haro11, which has been argued by Rossi et al. (2018) to be a good low redshift analogue for LBGs and has a relatively high dust temperature, and the ALPINE SED template (Béthermin et al. 2020), which is based on a stacking analysis of the ALPINE target and analogue galaxies fitted to models from Béthermin et al. (2017). The Michałowski et al. (2010) template is based on the average SED from a sample of submillimeter galaxies (SMGs). Finally we also indicate the approximate conversion factor and dust temperatures found by Faisst et al. (2020) analyzing a small sample of $z \sim 5.5$ galaxies using the Casey et al. (2018) models.

For our fiducial $z \sim 7$ dust temperature of 50 K and assuming $\beta_{UV,intr} = -2.63$, the current results appear to be more consistent (3σ significance) with a SMC-like attenuation law than a Calzetti-like attenuation law, while for a $\beta_{UV,intr} = -2.23$, current results lie somewhere between a Calzetti and SMC-like attenuation law. For much hotter dust temperatures, as suggested by recent observations (Laporte et al. 2019; Bakx et al. 2020), $dA_{UV}/d\beta_{UV}$ would be to be more consistent with a Cazetti attenuation law. We also explored the impact of scatter (0.1 dex) on the dust temperatures of the sample, instead of assuming a uniform temperature, and found minimal changes ($\lesssim$0.05 dex) to the results. The present results are similar to earlier $z > 6.5$ results by Watson et al. (2015), Laporte et al. (2017), Knudsen et al. (2017), Bowler et al. (2018), and Tamura et al. (2019) who also found greater consistency with a Calzetti-like attenuation law when assuming $\beta_{UV,intr} = -2.23$.

2.3.5 *IRX-Stellar Mass relation*

The infrared excess is also known to show a strong correlation with the stellar mass of sources, with an approximately linear power-law dependence on stellar mass (e.g., Bouwens et al. 2016a; Dunlop et al. 2016; McLure et al. 2018). Interestingly enough, little evolution is observed between $z \sim 3$ and $z \sim 0$ in the relationship between the infrared excess and the stellar mass (Pannella et al. 2015; Bouwens et al. 2016b; Whitaker et al. 2017; McLure et al. 2018).

In Figure 2.8 (*upper panel*), we present the infrared excess we derive for our sources against their inferred stellar masses. The blue and red stars

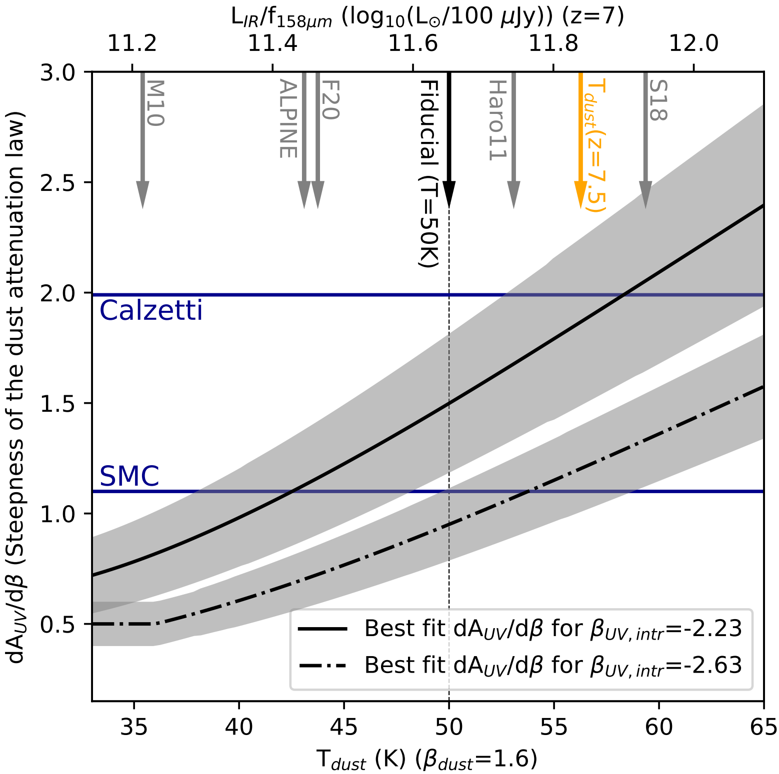

Figure 2.7. Dependence of the slope parameter of the IRX-β relation ($\mathrm{dA}_{UV}/\mathrm{d}\beta_{UV}$) on (luminosity-weighted) dust temperature for two different values for the intrinsic UV-continuum slope $\beta_{UV,intr}$ (*solid and dash-dotted black lines*). The grey regions show the slopes $\mathrm{dA}_{UV}/\mathrm{d}\beta_{UV}$ preferred at 68% confidence. The fit uses all detections and upper limits presented in this paper and the literature ($z > 6.5$ and $\mathrm{M}_{UV} < -21.5$: $\gtrsim 1.7 L^*_{UV}$). The blue lines indicate a reference to slope of the SMC and Calzetti relations, while the orange arrow shows the expected dust temperature of LBG galaxies at $z \sim$ 7-8 extrapolating dust temperature results in the literature (Bouwens et al. 2020). The grey arrows shown along the top x-axis indicate the $L_{IR}/f_{158\mu m}$ conversion factors (at z=7) for a variety of high-redshift dust SED templates from the literature and at the corresponding temperature of the modified black body that has the same conversion factor. Here M10 denotes the FIR-SED model from Michałowski et al. (2010), ALPINE the model from Béthermin et al. (2020), F20 from Faisst et al. (2020), Haro11 from Rossi et al. (2018), and S18 from Schreiber et al. (2018). The black arrow and vertical dotted line indicate the fiducial 50 K temperature we adopt for our analysis. For $\beta_{UV,intr} = -2.23$, we find a much better fit of the observational results for an attenuation curve between Calzetti and SMC, and for a $\beta_{UV,intr} = -2.63$, we find a much better fit to a SMC-like attenuation curve.

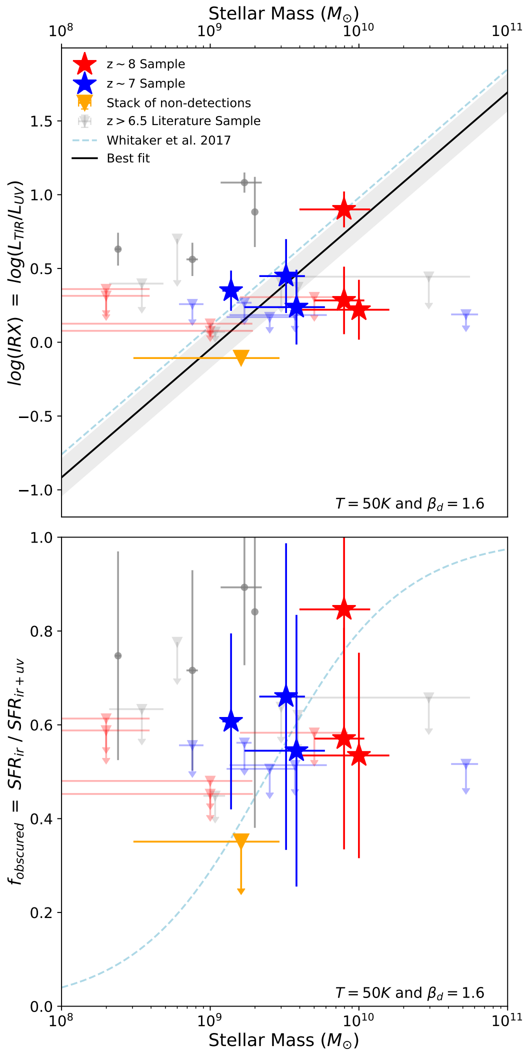

Figure 2.8. (*upper*) IRX-stellar mass relation for a sample of sources at $z > 6.5$, including the detections and non-detections presented in this paper and a compilation of sources from the literature (see Figure 2.2 for references). The local relation (Whitaker et al. 2017) is shown with the dotted line and our best-fit is shown with the black solid line and the grey shaded uncertainty. *(lower)* Fraction of the star formation that is obscured by dust as a function of stellar mass for our sample and sources from the literature. For a modified black body with a dust temperature of 50 K and a dust emissivity of β_{dust}=1.6 (Casey 2012), the $z = 0$ relation (Whitaker et al. 2017) is broadly consistent with the detections seen at high redshift.

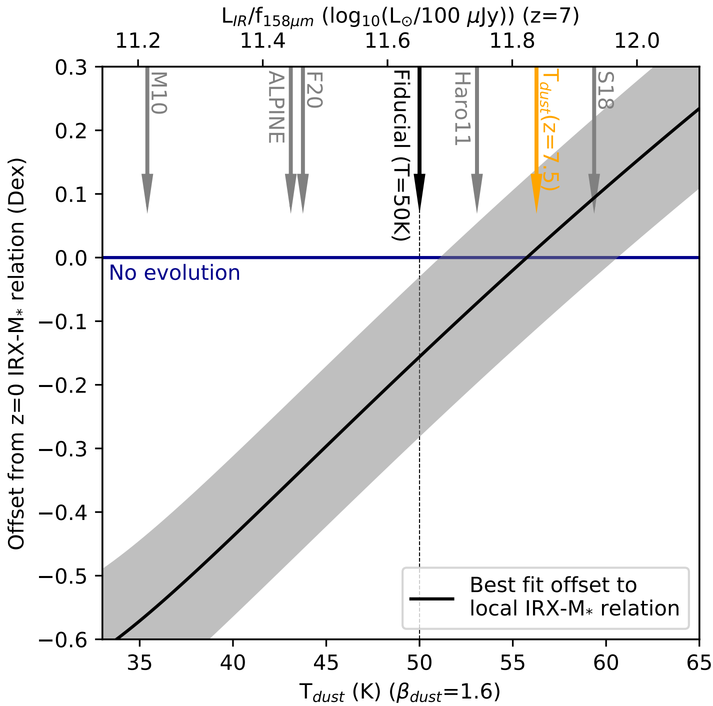

Figure 2.9. Similar to Figure 2.7, this Figure shows the dependence on (luminosity-weighted) dust temperature of the offset with respect to the local IRX stellar mass relation fitted to the detections and upper limits presented in this paper and the literature (z >6.5 and M_{UV} <−21.5 mag: $\gtrsim 1.7 L^*_{UV}$). The black line shows the best-fit offset while the grey-shaded area shows the offsets preferred at 68% confidence. The blue line is a visual reference corresponding to no evolution. For fit values below this line, the implied IRX at $z > 6.5$ is lower than the local relation at a fixed stellar mass. For the current data, this would be the case for dust temperatures below $\lesssim$54K. The top x-axis and the black, grey, and orange arrows are as in Figure 2.7. For dust temperatures of ∼50-55 K, the present IRX-stellar mass results appear to be broadly consistent with the $z \sim 0$ relation (Whitaker et al. 2017).

correspond to $z \sim 7$ and $z \sim 8$ galaxies, respectively, detected in the dust-continuum, while the light blue and light red upper limits correspond to sources which are not detected in the dust continuum ($< 3\sigma$). The grey circles show dust-continuum detections from the literature. Stellar masses for bright $z \sim 8$ sources in our selection are from Stefanon et al. (2019).

Stellar masses for bright $z \sim 7$ sources are inferred using the same SED-fitting assumptions as Stefanon et al. (2019) use at $z \sim 8$, i.e., with a 0.2 $Z_\odot$ metallicity, constant star formation rate, and Calzetti et al. (2000) dust curve. The lower panel in Figure 2.8 shows fraction of obscured star formation against stellar mass. Our results seem broadly consistent with the $z \sim 0$ relation presented in Whitaker et al. (2017) given the sizable uncertainties and large number of upper limits.

Similar to Figure 2.7, we illustrate in Figure 2.9 how the normalization in the IRX-stellar mass relation depends on the assumed dust temperature of $z \sim$ 7-8 galaxies. We quantify the normalization in terms of an offset (in dex) from the low-redshift relation (Whitaker et al. 2017) and fit this offset as a function of dust temperatureusing the same fitting procedure as described in Section 2.3.4. As in Figure 2.7, the vertical orange line indicates the expected temperature for $z \sim$ 7-8 galaxies when extrapolating lower redshift results. At this temperature, the offset we derive is consistent with no evolution from $z \sim 0$. Not surprisingly, for lower and higher values of the dust temperature, the IRX is lower and higher respectively than the $z \sim 0$ relation.

2.4 DISCUSSION

2.4.1 *Constraints on Dust Evolution Models*

Our new observations provide constraints on the build-up of dust in early high-redshift galaxies. In addition to the significant impact dust has on the fraction of UV light seen from star-forming galaxies and that re-emitted in the far-infrared, dust can play a critical role in galaxy evolution (Salim & Narayanan 2020). Significantly, the surfaces of dust grains serve as the main production sites of many molecular species and can catalyze the formation of molecular clouds in which star formation (SF) takes place (e.g., Gould & Salpeter 1963; Cazaux & Tielens 2004; Hirashita & Ferrara 2002; Yamasawa et al. 2011; Chen et al. 2017). Additionally, dust cooling induces fragmentation inside molecular clouds, which has a significant impact on the stellar initial mass function (IMF; Omukai 2000; Omukai et al. 2005; Schneider et al. 2006).

In Figure 2.10, we show estimates for the dust masses of our sources as a function of temperature, and a strong dependence on the assumed dust temperature can be clearly seen. We derive our estimates for the dust masses of our sources following the procedure described in Ota et al.

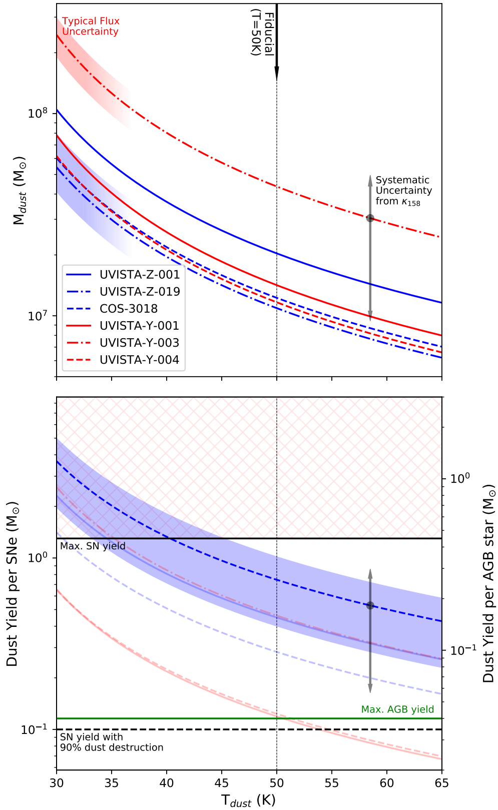

Figure 2.10. (*upper*) Dust masses as a function of dust temperature. The impact of uncertainties on the flux measurements for the z ∼7 and z ∼8 samples are indicated with the blue and red shaded regions, respectively. An indicative systematic uncertainty resulting from the choice of dust mass absorption coefficient is shown with the black arrow. The dotted vertical line indicates the fiducial dust temperature adopted here. (*lower*) Constraint on the dust yield per SNe (*left axis*) or AGB star (*right axis*) as a function of temperature for our sources. We highlight COS-3018 which provides the most demanding constraints on the yields, where the blue shaded region shows the error from the flux measurement and the uncertainty in stellar mass. The black arrow indicates the systematic uncertainty resulting from the choice of dust mass absorption coefficient. The maximum theoretical dust yield from SNe without any dust destruction and after 90% dust destruction are indicated with the solid and dashed black lines respectively. The maximum yield per AGB star is indicated with the green solid line. Note that if the dust yield constraint for a source is above any of these lines, that particular dust production mechanism alone cannot explain the amount of dust we observe. In particular, for dust temperatures below T∼40 K and our assumed value of κ_{158}, SNe, even without dust destruction, cannot explain the observed dust masses (indicated with the red hatched region).

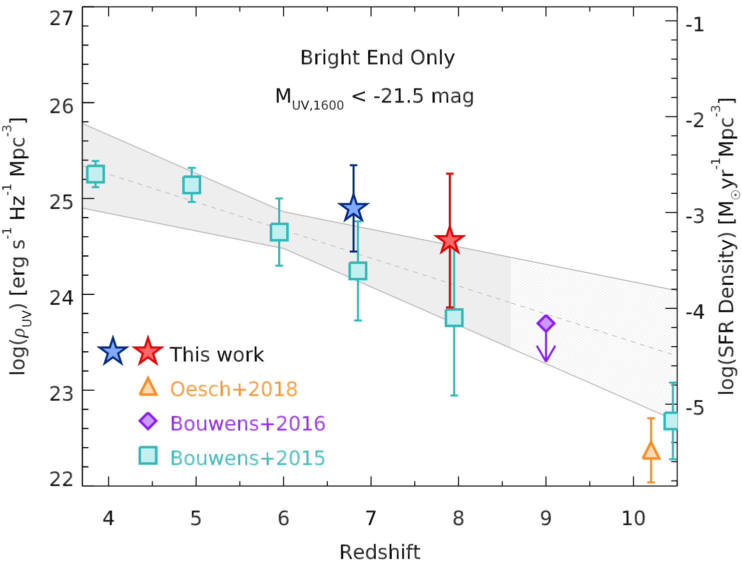

Figure 2.11. The SFR density inferred for especially bright ($M_{UV,AB} < -21.5$ mag: $\gtrsim 1.7L^*_{UV}$) galaxies at $z \sim$ 4-9, based on the rest-frame UV light (blue circles and squares) alone and including the contribution of dust obscured SF at $z \sim 7$ and $z \sim 8$ (*red points*). The shaded grey region indicates the best-fit trend in UV luminosity density (68% confidence intervals) for UV-bright (<-21.5 mag: $\gtrsim 1.7L^*_{UV}$) galaxies against redshift (Stefanon et al. 2019). Our ALMA results suggest that ~25-50% of the star formation activity in such bright $z \sim$ 7-8 galaxies is obscured by dust.

(2014):

$$M_{dust} = \frac{S_{\nu_{rest}} D_L^2}{(1+z)\kappa_d(\nu_{rest}) B_{\nu_{rest}}(T_{dust})} \tag{3}$$

where S_ν is the observed flux density after correction for contrast with the CMB (da Cunha et al. 2013, equation 18), D_L is the luminosity distance, $B_\nu(T_{dust})$ is the Planck function at a rest-frame frequency ν_{rest} and dust temperature T_{dust}, and finally $\kappa_d(\nu_{rest})$ is the dust mass absorption coefficient, which scales as $\kappa_d(\nu_{rest}) = \kappa_0(\nu_{rest}/\nu_{ref})^{\beta_{dust}}$. Here we assume $\kappa_0 = 8.94\ cm^2\ g^{-1}$ at 158 μm which is appropriate for dust ejected from SN after reverse shock destruction (Hirashita et al. 2014), since it is expected that the majority of dust is produced by SN (Michałowski 2015; Leśniewska & Michałowski 2019). Alternatively, values ranging from $\kappa_0 = 28.4\ cm^2\ g^{-1}$ at 158 μm for dust consisting of amorphous carbon to $\kappa_0 = 5.57\ cm^2\ g^{-1}$ at 158 μm for dust condensed in SN before reverse shock destruction (Hirashita et al. 2014) could be considered, leading to an additional ∼0.7 dex systematic uncertainty. Moreover, studies constraining κ_0 directly from observations span a full 3.6-dex range with 0.8 dex scatter (Clark et al. 2019). The impact of these systematic uncertainties (assumed to be 0.7 dex) is shown with the black arrow on Figure 2.10.

Because our data are observed at ∼158 μm rest-frame, which is the same as the reference wavelength of the dust mass absorption coefficient we use from the literature, our choice of β_{dust} introduces minimal uncertainty in the derived dust masses. While most of our galaxies appear consistent with dust masses of $\sim 10^7 M_\odot$, the large systematic uncertainty limits us to inferring that the dust mass lies somewhere in the range $\sim 10^7 M_\odot$ to $10^8 M_\odot$ for our sources (assuming $30 < T_{dust} < 65$).

In the bottom panel of Figure 2.10 we use these dust masses in combination with the stellar mass from SED fitting to derive the required dust yields per SNe or AGB star following the method described by Michałowski (2015). The stellar mass is translated to the number of SNe or AGB stars that could have contributed to the formation of dust assuming a Chabrier (2003) IMF and a maximum age of 500 Myr (corresponding to a maximum formation redshift of $z \gtrsim 18$; Michałowski 2015). This number is subsequently divided by the dust mass to obtain the required yields. We compare the required yields for our observed dust masses to the maximum yield from a single AGB star (∼0.004 $M_\odot$: Morgan & Edmunds 2003; Ferrarotti & Gail 2006; Ventura et al. 2012; Nanni et al. 2014; Schneider et al. 2014) and a single supernova without any dust destruction (approximately ∼1.3 $M_\odot$: Todini & Ferrara 2001; Nozawa et al. 2003). However, it is likely that a large portion of the dust produced by supernovae is destroyed by internal shocks, releasing only $\lesssim 0.1 M_\odot$ into the ISM (Bianchi & Schneider 2007; Cherchneff & Dwek 2010; Gall et al. 2011; Lakićević et al. 2015; Ferrara & Peroux 2021).

From this Figure it is clear that for our sources dust production from supernovae alone could explain the majority of the observed dust, but only when dust destruction is low (less than ∼90%). Production from AGB stars by itself (green line) is insufficient to explain the observed dust masses for all dust temperatures. For low dust temperatures T<40 K even dust production from supernovae without any dust destruction would be insufficient and other mechanism like grain growth (Michałowski 2015; Leśniewska & Michałowski 2019) would be necessary to explain the observed dust masses. Alternatively it is possible that the stellar masses are underestimated, which would lower the required dust yields. Specifically, stellar masses are difficult to measure for sources without a spectroscopic redshifts because the rest-frame optical emission as measured from *Spitzer* IRAC is contaminated by strong nebular emission lines. This contribution is redshift dependent, leading to a 0.6-1.0 dex change in the stellar mass for $\Delta z \sim 0.2$ at $z \sim 7$ (e.g., Schaerer & de Barros 2009; Roberts-Borsani et al. 2020, Topping et al., in prep). Even with spectroscopic redshifts, the contribution of older populations of stars to the stellar mass are difficult to constrain. Rest-frame near infrared data would be invaluable to accurately constrain such contributions, however unfortunately there are currently no instruments that can observe this part of the spectrum with sufficient sensitivity.

2.4.2 *Impact on Measurements of the SFR Density and the IR luminosity function at $z > 6$*

The ALMA observations from our programs have particular value in determining the quantity of the star formation from *UV* bright galaxies at $z \sim$ 7-8 that is obscured by dust. This is particularly useful for gaining a handle on the likely build-up of mass that occurs in the brightest and most massive galaxies with cosmic time.

To estimate the approximate correction that we need to make to the SFR density of bright $z \sim$ 7-8 galaxies to correct for the impact of dust, we compute an effective infrared excess for the entire population of bright $z \sim 7$ and $z \sim 8$ we have targeted as part of multiple programs by dividing the mean SFR_{IR} by the mean SFR_{UV}. Using our bootstrap stacking results from section 2.3.2, we can compute the median ratio and errors (68%) on the obscured and *UV* luminous star formation rates to be $0.6^{+0.4}_{-0.3}$ and $0.7^{+0.2}_{-0.3}$, respectively. This suggests that unobscured SFRs measured from the rest-frame *UV* data should be corrected by factors of $1.6^{+0.4}_{-0.3}$ ($0.20^{+0.10}_{-0.10}$ dex) for $z \sim 7$ and $1.7^{+0.2}_{-0.3}$ ($0.23^{+0.06}_{-0.09}$ dex) for $z \sim 8$.

We can illustrate the impact these corrections have on the estimated SFR densities at $z \sim$ 7-8 from *UV* bright galaxies based on the *UV* LFs derived by Bouwens et al. (2015) and Stefanon et al. (2019) integrated down to -21.5 mag ($\sim$1.7 L^*_{UV}). Applying these corrections to the *UV* luminosity density, Bouwens et al. (2015)) derive at $z \sim 7$ and Stefanon et al. (2019) derive at $z \sim 8$, we show the impact of these corrections on the computed SFR densities at $z \sim$ 7-8 in Figure 2.11. Our ALMA results suggest that $\sim\frac{1}{3}$ of the SFR density in $\gtrsim 1.7L^*$ galaxies is obscured by dust.

This is consistent with the 20-25% fraction of the cosmic star formation rate density that Zavala et al. (2021) infer to be obscured at $z \sim$ 6-7, but it is worth emphasizing that the fraction we infer is for the UV-bright $z \sim 7$ population and the fraction Zavala et al. (2021) derive is with respect to the total.

Finally, we can combine the present constraints on the IR luminosities of sources with the $z \sim$ 7-8 rest-frame UV luminosity function results of Bowler et al. (2017) and Stefanon et al. (2019) to place constraints on the IR LF at $z > 3$ such as discussed in Koprowski et al. (2017), Casey et al. (2018), Gruppioni et al. (2020), and Zavala et al. (2021). We find that the number density of galaxies with $L_{IR} > 10^{11} - 10^{12} L_\odot$ is $\gtrsim 2 \times 10^{-6}$ Mpc^{-3} dex^{-1}. This value is insensitive to the assumed dust temperature, because changing the dust temperature does not change the number of detected galaxies in the range $L_{IR} > 10^{11} - 10^{12} L_\odot$.

The $\gtrsim 2 \times 10^{-6}$ Mpc^{-3} dex^{-1} lower limit is fairly consistent with the dust poor model described in Casey et al. (2018), which is only ~0.5 dex higher ($\sim 6 \times 10^{-6}$ Mpc^{-3} dex^{-1} at $z = 7.5$ and $L_{IR} = 3 \times 10^{11} L_\odot$), while the dust rich model is ~1.7 dex higher ($\sim 1 \times 10^{-4}$ Mpc^{-3} dex^{-1} at $z = 7.5$ and $L_{IR} = 3 \times 10^{11} L_\odot$). Our lower limit is ~0.3 dex higher than the model presented in Zavala et al. (2021) ($\sim 9 \times 10^{-7}$ Mpc^{-3} dex^{-1} at $z = 7.5$ and $L_{IR} = 3 \times 10^{11} L_\odot$). Better agreement with our observational results could be obtained by increasing the volume density of $L_{IR} \sim 10^{11} - 10^{12} L_\odot$ galaxies in this model by $\gtrsim$2× (see also Fudamoto et al. 2021). Finally, our lower limit is significantly higher (~4.5 dex) than the evolution of the IR luminosity function presented in Koprowski et al. (2017) ($\sim 7 \times 10^{-11}$ Mpc^{-3} dex^{-1} at $z = 7.5$ and $L_{IR} = 3 \times 10^{11} L_\odot$). The significant tension with our results primarily derives from the model only be constrained by observations to $z \sim 5$ and the assumption of an exponential decline of the normalization parameter (Φ_*) of the model luminosity function to higher redshifts.

2.5 SUMMARY

We describe the analysis of sensitive ALMA continuum observations we have obtained over 15 bright Lyman-break galaxies at $z \sim$ 7-8. The ALMA continuum observations we consider (in total 25.7 hours on source) are drawn from five distinct ALMA programs (Table 2.1) and allow us to assess the contribution of obscured star formation to the build-up of stellar mass in these galaxies. The observations are sensitive enough to probe down to obscured SFRs of ∼20 $M_{\odot}$/yr (3σ). The bright Lyman-break galaxies we have targeted were drawn from a selection of the brightest $z \sim$ 7-8 galaxies identified over the UltraVISTA (Stefanon et al. 2017, 2019, Schouws et al. *in prep*) and CANDELS COSMOS field (Smit et al. 2015; Smit et al. 2018).

Out of the 15 $z \sim$ 7-8 galaxies we target, we detect six in the dust continuum, with inferred IR luminosities ranging from 2.7×10^{11} $L_{\odot}$ to 1.1×10^{12} $L_{\odot}$, with a median of 3.5×10^{11} $L_{\odot}$. This is equivalent to obscured SFRs of 25 to 101 $M_{\odot}$/yr (Figure 2.1). These dust detections more than double the number of normal star-forming galaxies at $z > 6.5$ which are detected in the IR continuum from four (Watson et al. 2015; Laporte et al. 2017; Tamura et al. 2019; Bowler et al. 2018; Hashimoto et al. 2019) to 10 (Figure 2.2). We find the spatial position of dust-continuum detections to be approximately cospatial with the rest-frame UV light (median offset <0.2"), with UVISTA-Y-003 being a notable exception. For UVISTA-Y-003, the dust-continuum detection is offset by ∼0.3" from three distinct star-forming clumps seen in the rest-frame UV (Figure 2.5).

Using the new dust-continuum detections, we can quantify the relative contribution that obscured and unobscured star formation provide to bright galaxies at $z \sim$ 7-8. For the 6 bright galaxies in our sample which show ALMA continuum detections, we find that obscured SFR in these galaxies is comparable to the unobscured SFR in the median (Figure 2.3). The relation between SFR and $[CII]_{158\mu m}$ luminosity, for those sources with a $[CII]_{158\mu m}$ detection, will be explored in Schouws et al. (*in prep*).

We also use our observations to look at the measured infrared excess IRX (L_{IR}/L_{UV}) in these galaxies and quantify how the infrared excess depends on the UV-continuum slope β_{UV} and the stellar mass. The infrared excess IRX is well known to correlate with both quantities, but there continues to be significant debate regarding the precise trend at $z > 6$ with both β_{UV} and stellar mass.

Our IRX against β_{UV} results show a significant dependence on what we assume for the dust temperature of $z \sim$ 7-8 galaxies as well as what we assume for the unreddened UV slope $\beta_{UV,intr}$ for star-forming galaxies at $z \sim$ 7-8. If we adopt a modified blackbody SED with a dust temperature of 50 K and an opacity index $\beta = 1.6$ as our fiducial far-IR SED, we find current IRX against β results are most consistent with an SMC dust curve if $\beta_{UV,intr} = -2.63$ and lie somewhere between a Calzetti and SMC dust curve if $\beta_{UV,intr} = -2.23$ (Figure 2.6). Adopting the same fiducial SEDs for interpreting IRX trends with stellar mass, we find results (Figure 2.8) which are consistent with no evolution in IRX-stellar mass relation from $z \sim 0$ (Whitaker et al. 2017).

Additionally, we use our new dust detections to estimate the total mass in dust in bright $z \sim$ 7-8 galaxies, for dust ejected from SN after reverse shock destruction. The dust masses we derive are dependent on the assumed dust temperature and range from $\sim 10^8 M_\odot$ for low dust temperatures (T∼30 K) to $\sim 10^7 M_\odot$ for high temperatures (T∼60 K) (Figure 2.10). Combining these dust masses with the estimates for the stellar mass from SED fitting enable constraints on dust formation mechanisms (following Michałowski (2015)). This shows that the our observed dust masses could be most likely be explained by dust production from SNe with low dust destruction (less than ∼90%: see bottom panel of Figure 2.10).

The new measurements we make of the obscured SFRs in bright $z \sim$ 7-8 allow us to improve our estimates of the contribution very luminous bright galaxies make to the SFR density at $z \sim$ 7-8. Incorporating the contribution from obscured star formation for both our bright $M_{UV,AB} < -21.5$ ($\gtrsim 1.7 L^*_{UV}$) $z \sim 7$ and $z \sim 8$ sample to the unobscured SFRs in these galaxies, we measure correction factors of $1.6^{+0.4}_{-0.3}$ ($0.20^{+0.10}_{-0.10}$ dex) and $1.7^{+0.2}_{-0.3}$ ($0.23^{+0.06}_{-0.09}$ dex), respectively. These results clearly illustrate the important role that obscured star formation can play in the early stellar mass build-up of galaxies at $z \geq 7$.

Finally, we use these results to set a lower limit on the IR luminosity function of $z \sim$ 7-8 galaxies, finding $\gtrsim 2 \times 10^{-6}$ Mpc^{-3} dex^{-1} for galaxies with $L_{IR} > 10^{11} - 10^{12}$ $L_\odot$/yr. This limit is most consistent with the dust poor model of Casey et al. (2018), which is ∼0.5 dex higher.

In the future, we expect a significant increase in the number of dust detected galaxies in normal star-forming galaxies at $z \sim$ 7-8 from the ongoing ALMA observations from the REBELS ALMA Large program (2019.1.01634.L). This should allow us to look at the build-up of dust in massive galaxies in much more detail, while allowing for a much more detailed look into how the measured IRX depends on both stellar mass and the UV slope.

ACKNOWLEDGEMENTS

We are greatly appreciative to our ALMA program coordinators Daniel Harsono and Carmen Toribio at ALLEGRO for support with our ALMA programs. This paper makes use of the following ALMA data:
ADS/JAO.ALMA#2017.1.01217.S,
ADS/JAO.ALMA#2017.1.00604.S,
ADS/JAO.ALMA#2018.1.00236.S,
ADS/JAO.ALMA#2018.1.00085.S
and ADS/JAO.ALMA#2018.A.00022.S. ALMA is a partnership of ESO (representing its member states), NSF (USA) and NINS (Japan), together with NRC (Canada), MOST and ASIAA (Taiwan), and KASI (Republic of Korea), in cooperation with the Republic of Chile. The Joint ALMA Observatory is operated by ESO, AUI/NRAO and NAOJ. SS, MS, and RB acknowledge support from TOP grant TOP1.16.057 and a NOVA (Nederlandse Onderzoekschool Voor Astronomie) 5 grant. RS acknowledges support from an STFC Ernest Rutherford Fellowship (ST/S004831/1). JH acknowledges support of the VIDI research programme with project number 639.042.611, which is (partly) financed by the Netherlands Organisation for Scientific Research (NWO). SC acknowledges support from the European Research Council No. 74120 INTERSTELLAR. R.M. acknowledges support by the Science and Technology Facilities Council (STFC) and ERC Advanced Grant 695671 "QUENCH".

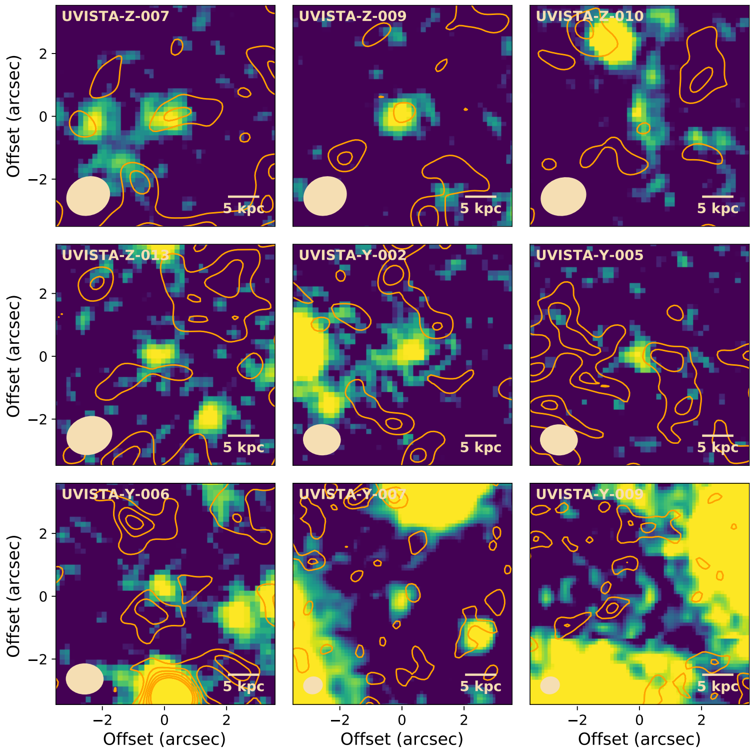

Figure 2.12. Dust-continuum observations (1.2μm) overlaid on the available near-IR imaging observations from UltraVISTA (stacked J+H+K_s). Shown are the 9 $z \sim$ 7-8 sources that were not detected in the dust continuum. Contours are drawn at (1, 2, 3, 4, 5, 6)$\times\sigma$ where $\sigma \approx 15\mu$Jy beam^{-1}. The synthesized beam for the dust-continuum observations is indicated in the lower-left corner of each panel.

A. ALMA OBSERVATIONS OF BRIGHT $Z \sim$ 7-8 GALAXIES THAT ARE UNDETECTED IN THE DUST CONTINUUM

Nine of the 15 bright $z \sim$ 7-8 galaxies (60%) targeted by the ALMA programs considered here did not show 3σ detections in the dust continuum. Figure 2.12 shows rest-frame UV images of those nine sources along with (1, 2, 3, 4, 5)σ contours showing the IR dust continuum emission.

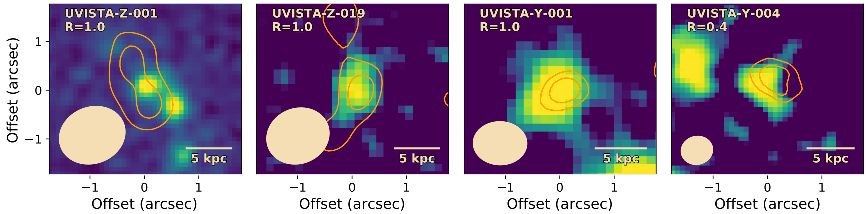

Figure 2.13. The Briggs weighted dust continuum imaging (*orange contours*) overlaid on the rest-frame *UV* imaging (HST F140W for UVISTA-Z-001, ground-based J+H+K for the others) for four targets from our programs with continuum detections. The *robust* parameter we utilize for the imaging is also indicated for each source. We see no significant offset between the dust continuum and rest-frame *UV* emission. The apparent offset (0.28" or ~1.5 Kpc) between the *UV* and IR peaks for UVISTA-Y-004 is not significant, being comparable to the SNR-based astrometric accuracy (~0.2").

Interestingly enough, in the observations we obtain of UVISTA-Y-006, one foreground galaxy in our ALMA beam shows a clear dust-continuum detection (lowest row in Figure 2.12, left panel).

B. BRIGGS WEIGHTED IMAGING OF THE CONTINUUM DETECTED SOURCES

Figure 2.13 shows the Briggs weighted imaging of those targets from our programs with a continuum detection. Briggs weighting changes the relative contributions of long baselines and shorter baselines in the *(u,v)*-plane, which affects the point spread function and subsequently the effective resolution and signal to noise of our observations. The trade-off for increasing the resolution is a decrease in signal to noise. The Briggs weighting is parameterized using the *robust* parameter (R), which varies from -2.0 to $+2.0$. A value of R=-2.0 is equivalent to a uniform weighting, which has the highest resolution but lowest SNR and R=$+2.0$ which is equivalent to natural weighting, corresponding to the lowest resolution and highest SNR.

In the Figure below we use the lowest robust parameter that still results in a $\geq 3\sigma$ peak flux (in steps of ΔR=0.2). Note that due to the loss in signal-to-noise caused by the Briggs weighting, the contours only show the location of the peak of the dust emission, not its extent. For all detections, clear overlap is seen between the dust continuum and rest-frame *UV* emission.

REFERENCES

Álvarez-Márquez, J., Burgarella, D., Heinis, S., et al. 2016, A&A, 587, A122.

Aravena, M., Decarli, R., Walter, F., et al. 2016, The Astrophysical Journal, 833, 68.

Aravena, M., Boogaard, L., Gónzalez-López, J., et al. 2020, The Astrophysical Journal, 901, 79.

Ashby, M. L. N., Caputi, K. I., Cowley, W., et al. 2018, The Astrophysical Journal Supplement Series, 237, 39.

Bakx, T. J. L. C., Tamura, Y., Hashimoto, T., et al. 2020, MNRAS, 493, 4294

Barisic, I., Faisst, A. L., Capak, P. L., et al. 2017, The Astrophysical Journal, 845, 41.

Bañados, E., Decarli, R., Walter, F., et al. 2015, The Astrophysical Journal, 805, L8.

Behrens, C., Pallottini, A., Ferrara, A., Gallerani, S., & Vallini, L. 2018, MNRAS, 477, 552

Béthermin, M., Daddi, E., Magdis, G., et al. 2015, A&A, 573, A113.

Béthermin, M., Wu, H.-Y., Lagache, G., et al. 2017, A&A, 607, A89.

Béthermin, M., Fudamoto, Y., Ginolfi, M., et al. 2020, A&A, 643, A2.

Bianchi, S., & Schneider, R. 2007, Monthly Notices of the Royal Astronomical Society, 378, 973.

Bouwens, R., González-López, J., Aravena, M., et al. 2020, ApJ, 902, 112

Bouwens, R. J., Oesch, P. A., Illingworth, G. D., Ellis, R. S., & Stefanon, M. 2017, The Astrophysical Journal, 843, 129.

Bouwens, R. J., Illingworth, G. D., Oesch, P. A., et al. 2011, The Astrophysical Journal, 737, 90.

Bouwens, R. J., Bradley, L., Zitrin, A., et al. 2014, The Astrophysical Journal, 795, 126.

Bouwens, R. J., Illingworth, G. D., Oesch, P. A., et al. 2015, The Astrophysical Journal, 803, 34.

Bouwens, R. J., Oesch, P. A., Labbé, I., et al. 2016a, The Astrophysical Journal, 830, 67.

Bouwens, R. J., Aravena, M., Decarli, R., et al. 2016b, The Astrophysical Journal, 833, 72.

Bowler, R. A. A., Bourne, N., Dunlop, J. S., McLure, R. J., & McLeod, D. J. 2018, Monthly Notices of the Royal Astronomical Society, 481, 1631.

Bowler, R. A. A., Dunlop, J. S., McLure, R. J., & McLeod, D. J. 2017, Monthly Notices of the Royal Astronomical Society, 466, 3612.

Bradač, M., Garcia-Appadoo, D., Huang, K.-H., et al. 2017, The Astrophysical Journal, 836, L2.

Calzetti, D., Armus, L., Bohlin, R. C., et al. 2000, The Astrophysical Journal, 533, 682.

Capak, P., Aussel, H., Ajiki, M., et al. 2007, The Astrophysical Journal Supplement Series, 172, 99.

Capak, P., Aussel, H., Bundy, K., et al. 2013, SPLASH: Spitzer Large Area Survey with Hyper-Suprime-Cam, Spitzer Proposal, ,

Capak, P. L., Carilli, C., Jones, G., et al. 2015, Nature, 522, 455.

Caputi, K. I., Deshmukh, S., Ashby, M. L. N., et al. 2017, The Astrophysical Journal, 849, 45.

Carniani, S., Maiolino, R., Smit, R., & Amorín, R. 2018, The Astrophysical Journal, 854, L7.

Carniani, S., Maiolino, R., Pallottini, A., et al. 2017, A&A, 605, A42.

Casey, C. M. 2012, Monthly Notices of the Royal Astronomical Society, 425, 3094.

Casey, C. M., Scoville, N. Z., Sanders, D. B., et al. 2014, The Astrophysical Journal, 796, 95.

Casey, C. M., Zavala, J. A., Spilker, J., et al. 2018, The Astrophysical Journal, 862, 77.

Cazaux, S., & Tielens, A. G. G. M. 2004, The Astrophysical Journal, 604, 222.

Chabrier, G. 2003, Publications of the Astronomical Society of the Pacific, 115, 763.

Chen, L.-H., Hirashita, H., Hou, K.-C., et al. 2017, Monthly Notices of the Royal Astronomical Society, 474, 1545.

Cherchneff, I., & Dwek, E. 2010, The Astrophysical Journal, 713, 1–24.

Clark, C. J. R., De Vis, P., Baes, M., et al. 2019, Monthly Notices of the Royal Astronomical Society, 489, 5256.

Coppin, K. E. K., Geach, J. E., Almaini, O., et al. 2014, Monthly Notices of the Royal Astronomical Society, 446, 1293.

Cormier, D., Abel, N. P., Hony, S., et al. 2019, A&A, 626, A23.

Cucciati, O., Tresse, L., Ilbert, O., et al. 2012, A&A, 539, A31.

da Cunha, E., Groves, B., Walter, F., et al. 2013, The Astrophysical Journal, 766, 13.

Daddi, E., Dickinson, M., Morrison, G., et al. 2007, The Astrophysical Journal, 670, 156.

Daddi, E., Dannerbauer, H., Stern, D., et al. 2009, The Astrophysical Journal, 694, 1517.

Dunlop, J. S., McLure, R. J., Biggs, A. D., et al. 2016, Monthly Notices of the Royal Astronomical Society, 466, 861.

Ellis, R. S., McLure, R. J., Dunlop, J. S., et al. 2012, The Astrophysical Journal, 763, L7.

Endsley, R., Stark, D. P., Chevallard, J., & Charlot, S. 2021, MNRAS, 500, 5229

Erben, T., Hildebrandt, H., Lerchster, M., et al. 2009, A&A, 493, 1197.

Faisst, A. L., Fudamoto, Y., Oesch, P. A., et al. 2020, Monthly Notices of the Royal Astronomical Society, https://academic.oup.com/mnras/advance-article-pdf/doi/10.1093/mnras/staa2545/33674766/st staa2545.

Faisst, A. L., Capak, P. L., Yan, L., et al. 2017, The Astrophysical Journal, 847, 21.

Ferrara, A., & Peroux, C. 2021, Monthly Notices of the Royal Astronomical Society, 503, 4537.
Ferrarotti, A. S., & Gail, H. P. 2006, A&A, 447, 553.
Finkelstein, S. L., Ryan, R. E., Papovich, C., et al. 2015, The Astrophysical Journal, 810, 71.
Fudamoto, Y., Oesch, P. A., Schinnerer, E., et al. 2017, Monthly Notices of the Royal Astronomical Society, 472, 483.
Fudamoto, Y., Oesch, P. A., Magnelli, B., et al. 2019a, Monthly Notices of the Royal Astronomical Society, 491, 4724.
—. 2019b, Monthly Notices of the Royal Astronomical Society, 491, 4724.
Fudamoto, Y., Oesch, P. A., Faisst, A., et al. 2020, A&A, 643, A4
Fudamoto, Y., Oesch, P. A., Schouws, S., et al. 2021, Nature, 597, 489–492
Gaia Collaboration, Brown, A. G. A., Vallenari, A., et al. 2018, A&A, 616, A1.
Gall, C., Hjorth, J., & Andersen, A. C. 2011, A&A Rv, 19, 43.
Gould, R. J., & Salpeter, E. E. 1963, ApJ, 138, 393
Grogin, N. A., Kocevski, D. D., Faber, S. M., et al. 2011, The Astrophysical Journal Supplement Series, 197, 35.
Gruppioni, C., Béthermin, M., Loiacono, F., et al. 2020, A&A, 643, A8.
Harikane, Y., Ouchi, M., Inoue, A. K., et al. 2020, ApJ, 896, 93
Hashimoto, T., Laporte, N., Mawatari, K., et al. 2018, Nature, 557, 392.
Hashimoto, T., Inoue, A. K., Mawatari, K., et al. 2019, Publications of the Astronomical Society of Japan, 71, https://academic.oup.com/pasj/article-pdf/71/4/71/29163312/psz049.pdf, 71.
Hildebrandt, H., Pielorz, J., Erben, T., et al. 2009, A&A, 498, 725.
Hirashita, H., & Ferrara, A. 2002, Monthly Notices of the Royal Astronomical Society, 337, 921.
Hirashita, H., Ferrara, A., Dayal, P., & Ouchi, M. 2014, Monthly Notices of the Royal Astronomical Society, 443, 1704.
Hodge, J. A., & da Cunha, E. 2020, Royal Society Open Science, 7, 200556
Inoue, A. K., Tamura, Y., Matsuo, H., et al. 2016, Science, 352, 1559.
Karim, A., Schinnerer, E., Martínez-Sansigre, A., et al. 2011, The Astrophysical Journal, 730, 61.
Kawamata, R., Ishigaki, M., Shimasaku, K., et al. 2018, The Astrophysical Journal, 855, 4.
Knudsen, K. K., Watson, D., Frayer, D., et al. 2017, Monthly Notices of the Royal Astronomical Society, 466, 138.
Koprowski, M. P., Dunlop, J. S., Michałowski, M. J., et al. 2017, Monthly Notices of the Royal Astronomical Society, 471, 4155.
Lakićević, M., van Loon, J. T., Meixner, M., et al. 2015, The Astrophysical Journal, 799, 50.
Laporte, Pelló, R., Hayes, M., et al. 2012, A&A, 542, L31.

Laporte, N., Ellis, R. S., Boone, F., et al. 2017, The Astrophysical Journal, 837, L21.

Laporte, N., Katz, H., Ellis, R. S., et al. 2019, MNRAS, 487, L81

Le Fèvre, O., Béthermin, M., Faisst, A., et al. 2020, A&A, 643, A1

Leśniewska, A., & Michałowski, M. J. 2019, A&A, 624, L13.

Liang, L., Feldmann, R., Kereš, D., et al. 2019, MNRAS, 489, 1397

Madau, P., & Dickinson, M. 2014, ARA&A, 52, 415.

Magnelli, Elbaz, D., Chary, R. R., et al. 2009, A&A, 496, 57.

Magnelli, Popesso, P., Berta, S., et al. 2013, A&A, 553, A132.

Magnelli, Boogaard, L., Decarli, R., et al. 2020, The Astrophysical Journal, 892, 66.

Maiolino, R., Carniani, S., Fontana, A., et al. 2015, Monthly Notices of the Royal Astronomical Society, 452, 54.

Marrone, D. P., Spilker, J. S., Hayward, C. C., et al. 2018, Nature, 553, 51.

Martí-Vidal, I., Vlemmings, W. H. T., Muller, S., & Casey, S. 2014, A&A, 563, A136.

Matthee, J., Sobral, D., Boone, F., et al. 2017, The Astrophysical Journal, 851, 145.

Matthee, J., Sobral, D., Boogaard, L. A., et al. 2019, The Astrophysical Journal, 881, 124.

Mazzucchelli, C., Bañados, E., Venemans, B. P., et al. 2017, The Astrophysical Journal, 849, 91.

McCracken, H. J., Milvang-Jensen, B., Dunlop, J., et al. 2012, A&A, 544, A156.

McLeod, D. J., McLure, R. J., & Dunlop, J. S. 2016, Monthly Notices of the Royal Astronomical Society, 459, 3812.

McLure, R. J., Dunlop, J. S., Bowler, R. A. A., et al. 2013, Monthly Notices of the Royal Astronomical Society, 432, 2696.

McLure, R. J., Dunlop, J. S., Cullen, F., et al. 2018, Monthly Notices of the Royal Astronomical Society, 476, 3991.

Meurer, G. R., Heckman, T. M., & Calzetti, D. 1999, The Astrophysical Journal, 521, 64.

Michałowski, M., Hjorth, J., & Watson, D. 2010, A&A, 514, A67.

Michałowski, M. J. 2015, A&A, 577, A80.

Momcheva, I. G., van Dokkum, P. G., van der Wel, A., et al. 2016, Publications of the Astronomical Society of the Pacific, 129, 015004.

Morgan, H. L., & Edmunds, M. G. 2003, Monthly Notices of the Royal Astronomical Society, 343, 427.

Nanni, A., Bressan, A., Marigo, P., & Girardi, L. 2014, Monthly Notices of the Royal Astronomical Society, 438, 2328.

Nozawa, T., Kozasa, T., Umeda, H., Maeda, K., & Nomoto, K. 2003, The Astrophysical Journal, 598, 785–803.

Oesch, P. A., Bouwens, R. J., Illingworth, G. D., et al. 2015, The Astrophysical Journal, 808, 104.

Oesch, P. A., Bouwens, R. J., Illingworth, G. D., Labbé, I., & Stefanon, M. 2018, The Astrophysical Journal, 855, 105.

Oesch, P. A., Bouwens, R. J., Illingworth, G. D., et al. 2014, The Astrophysical Journal, 786, 108.

Oke, J. B., & Gunn, J. E. 1983, ApJ, 266, 713.

Omukai, K. 2000, The Astrophysical Journal, 534, 809.

Omukai, K., Tsuribe, T., Schneider, R., & Ferrara, A. 2005, The Astrophysical Journal, 626, 627.

Ota, K., Walter, F., Ohta, K., et al. 2014, The Astrophysical Journal, 792, 34.

Oteo, I., Ivison, R. J., Dunne, L., et al. 2016, The Astrophysical Journal, 827, 34.

Overzier, R. A., Heckman, T. M., Wang, J., et al. 2010, The Astrophysical Journal, 726, L7.

Pannella, M., Elbaz, D., Daddi, E., et al. 2015, The Astrophysical Journal, 807, 141.

Pentericci, L., Carniani, S., Castellano, M., et al. 2016, The Astrophysical Journal, 829, L11.

Reddy, N., Dickinson, M., Elbaz, D., et al. 2011, The Astrophysical Journal, 744, 154.

Reddy, N. A., Erb, D. K., Pettini, M., Steidel, C. C., & Shapley, A. E. 2010, The Astrophysical Journal, 712, 1070.

Reddy, N. A., Steidel, C. C., Fadda, D., et al. 2006, The Astrophysical Journal, 644, 792.

Reddy, N. A., Oesch, P. A., Bouwens, R. J., et al. 2018, The Astrophysical Journal, 853, 56.

Rémy-Ruyer, A., Madden, S. C., Galliano, F., et al. 2015, A&A, 582, A121.

Riechers, D. A., Bradford, C. M., Clements, D. L., et al. 2013, Nature, 496, 329.

Roberts-Borsani, G. W., Ellis, R. S., & Laporte, N. 2020, MNRAS, 497, 3440

Roberts-Borsani, G. W., Bouwens, R. J., Oesch, P. A., et al. 2016, The Astrophysical Journal, 823, 143.

Rossi, M. E. D., Rieke, G. H., Shivaei, I., Bromm, V., & Lyu, J. 2018, The Astrophysical Journal, 869, 4.

Salim, S., & Narayanan, D. 2020, ARA&A, 58, 529

Schaerer, D., & de Barros, S. 2009, A&A, 502, 423

Schenker, M. A., Robertson, B. E., Ellis, R. S., et al. 2013, The Astrophysical Journal, 768, 196.

Schneider, R., Omukai, K., Inoue, A. K., & Ferrara, A. 2006, Monthly Notices of the Royal Astronomical Society, 369, 1437.

Schneider, R., Valiante, R., Ventura, P., et al. 2014, Monthly Notices of the Royal Astronomical Society, 442, 1440.

Schreiber, C., Elbaz, D., Pannella, M., et al. 2018, A&A, 609, A30.

Schreiber, C., Pannella, M., Elbaz, D., et al. 2015, A&A, 575, A74.

Scoville, N., Aussel, H., Brusa, M., et al. 2007, The Astrophysical Journal Supplement Series, 172, 1.

Siana, B., Teplitz, H. I., Chary, R.-R., Colbert, J., & Frayer, D. T. 2008, ApJ, 689, 59

Sklias, P., Zamojski, M., Schaerer, D., et al. 2014, A&A, 561, A149.

Smail, I., Geach, J. E., Swinbank, A. M., et al. 2014, The Astrophysical Journal, 782, 19.

Smit, R., Bouwens, R. J., Franx, M., et al. 2015, The Astrophysical Journal, 801, 122.

Smit, R., Bouwens, R. J., Carniani, S., et al. 2018, Nature, 553, 178.

Sommovigo, L., Ferrara, A., Carniani, S., et al. 2021, MNRAS, 503, 4878

Stefanon, M., Labbé, I., Bouwens, R. J., et al. 2017, ApJ, 851, 43

—. 2019, ApJ, 883, 99

Stefanon, M., Aravena, M., Bouwens, R., et al. 2021, A Revolutionary Panchromatic View of Early Galaxy Growth via NIRSpec/IFU Observations of 12 Massive z>6.5 Galaxies with ALMA-derived [CII] redshifts, JWST Proposal. Cycle 1, , .

Strandet, M. L., Weiss, A., Vieira, J. D., et al. 2016, ApJ, 822, 80

Takeuchi, T. T., Buat, V., Heinis, S., et al. 2010, A&A, 514, A4.

Tamura, Y., Mawatari, K., Hashimoto, T., et al. 2019, The Astrophysical Journal, 874, 27.

Todini, P., & Ferrara, A. 2001, Monthly Notices of the Royal Astronomical Society, 325, 726.

Venemans, B. P., Walter, F., Zschaechner, L., et al. 2015a, The Astrophysical Journal, 816, 37.

Venemans, B. P., McMahon, R. G., Walter, F., et al. 2012, The Astrophysical Journal, 751, L25.

Venemans, B. P., Bañados, E., Decarli, R., et al. 2015b, The Astrophysical Journal, 801, L11.

Venemans, B. P., Walter, F., Decarli, R., et al. 2017, The Astrophysical Journal, 851, L8.

Venemans, B. P., Decarli, R., Walter, F., et al. 2018, The Astrophysical Journal, 866, 159.

Ventura, P., Criscienzo, M. D., Schneider, R., et al. 2012, Monthly Notices of the Royal Astronomical Society, 424, 2345.

Wang, T., Schreiber, C., Elbaz, D., et al. 2019, Nature, 572, 211.

Watson, D., Christensen, L., Knudsen, K. K., et al. 2015, Nature, 519, 327.

Whitaker, K. E., Pope, A., Cybulski, R., et al. 2017, The Astrophysical Journal, 850, 208.

Williams, C. C., Labbe, I., Spilker, J., et al. 2019, The Astrophysical Journal, 884, 154.

Willott, C. J., Carilli, C. L., Wagg, J., & Wang, R. 2015, The Astrophysical Journal, 807, 180.

Yamasawa, D., Habe, A., Kozasa, T., et al. 2011, The Astrophysical Journal, 735, 44.

Zavala, J. A., Casey, C. M., Manning, S. M., et al. 2021, The Astrophysical Journal, 909, 165.

Chapter 3

ALMA as a Redshift Machine: Using [CII] to Efficiently Confirm Galaxies in the Epoch of Reionization

The $[CII]_{158\mu m}$ line has long been proposed as a promising line to spectroscopically confirm galaxies in the epoch of reionization. In this paper we present the results of new ALMA observations spectral scanning for [CII] in six particularly luminous Lyman Break Galaxies at $z \sim 7$. The six sources were drawn from a sample of bright $z \sim 7$ galaxies identified using the wide-area optical, near-IR, and *Spitzer*/IRAC data over the COSMOS/UltraVISTA field and were targeted on the basis of tight constraints on their redshifts from their IRAC [3.6]-[4.5] colors. We detect significant ($> 9\sigma$) [CII] lines in three of our six targets (50%) co-spatial with the rest-UV emission from the ground/space-based near-IR imaging. The luminosities of the [CII] lines lie in the range 5.6 to $8.8 \times 10^8 L_\odot$, consistent with the local [CII]-SFR relation. Meanwhile, their $[CII]/L_{IR} \sim 1 - 3 \times 10^{-3}$ ratios are slightly elevated compared to local (U)LIRGS. This could be due to lower dust-to-gas or dust-to-metal ratios. We also find that our sources display a large kinematic diversity, with one source showing signs of rotation, one source a likely major merger and one dispersion dominated source that might contain a bright star-forming clump. Our results highlight the effectiveness of spectral scans with ALMA in spectroscopically confirming luminous galaxies in the epoch of reionization, something that is being be applied on a significantly larger sample in the on-going REBELS large program.

Schouws, Bouwens, Smit, Hodge, Stefanon, Witstok,
Hilhorst, Labbé, Algera, Boogaard, Maseda, Oesch,
Röttgering, and van der Werf
ApJ, 954, 103 (2023)

3.1 INTRODUCTION

Exploring the build-up of galaxies in the $z > 6.5$ universe just a few hundred million years after the Big Bang is a key frontier in extragalactic astronomy. Though 100s of UV-bright galaxy candidates at redshifts $z > 6.5$ (e.g., McLure et al. 2013; Bouwens et al. 2015; Finkelstein et al. 2015; Ishigaki et al. 2018; Bouwens et al. 2021; Harikane et al. 2021) are known, characterization of their physical properties has been difficult. Deriving these properties from optical and near-IR photometry is complicated by uncertainties in the redshifts (e.g., Bouwens et al. 2022; Robertson 2021), dust extinction (e.g., Fudamoto et al. 2020; Schouws et al. 2022; Bowler et al. 2021), and rest-frame optical nebular emission line properties (e.g., Smit et al. 2015; Endsley et al. 2021; Stefanon et al. 2022) of $z > 6$ galaxies.

Fortunately, with ALMA, it is possible to make great progress on the characterization of galaxies at $z > 6$ (e.g., Hodge & da Cunha 2020; Robertson 2021). The [CII]158μm line is especially interesting as it is the strongest cooling line of warm gas ($T < 10^4$ K) in galaxies. This line has already been detected in a significant number of galaxies out to $z \sim$ 7-8 (e.g., Walter et al. 2009; Wagg et al. 2010; Riechers et al. 2014; Willott et al. 2015; Capak et al. 2015; Maiolino et al. 2015; Pentericci et al. 2016; Knudsen et al. 2016; Bradač et al. 2017; Smit et al. 2018; Matthee et al. 2017, 2019; Harikane et al. 2020; Carniani et al. 2020; Le Fèvre et al. 2020; Béthermin et al. 2020; Venemans et al. 2020; Fudamoto et al. 2021). In addition to the immediate utility of [CII] to spectroscopically confirm galaxies in the reionization era and obtain a precise measurement of their redshift, the strength of this line makes it one of the prime features for studying the kinematics of high-z galaxies (e.g., Smit et al. 2018; Hashimoto et al. 2019; Jones et al. 2021). Dynamical masses are particularly interesting in that they give some handle on the masses of galaxies, which can be challenging to do from the photometry alone (e.g., Schaerer & de Barros 2009).

Despite the great utility of [CII] and the huge interest from the community, only a modest number of $z > 6.2$ galaxies had been found to show [CII] emission in the first six years of ALMA operations (e.g., Maiolino et al. 2015; Pentericci et al. 2016; Bradač et al. 2017; Matthee et al. 2017; Smit et al. 2018; Carniani et al. 2018; Hashimoto et al. 2019). Additionally, even in cases where the [CII] line was detected, only modest luminosities were found, i.e., $L_{[CII]} \lesssim 2\times10^8\ L_\odot$. One potentially important factor in the limited success of earlier probes for [CII] at $z > 6$ may have been the almost exclusive targeting of sources with redshifts from the Lyα emission line. At lower redshifts at least, Lyα emission seems to be much more prevalent in lower mass galaxies than it is in higher mass galaxies (e.g., Stark et al. 2010). Additionally, Lyα emitters have been found to be systematically low in their [CII] luminosity-to-SFR ratios (Harikane et al. 2018; Matthee et al. 2019). Both factors would have caused early ALMA observations to miss those galaxies with the brightest [CII] lines.

In a cycle 4 pilot, Smit et al. (2018) demonstrated the effectiveness of spectral scans for the [CII] line in $z > 6$ galaxies which are particularly luminous and which also have well constrained photometric redshifts. One aspect of the $z \sim 7$ galaxies from Smit et al. (2018) that allowed for particularly tight constraints on their redshifts were the high EWs of their strong [OIII]+Hβ emission lines in the *Spitzer*/IRAC bands. This is due to the particular sensitivity of the *Spitzer*/IRAC [3.6]−[4.5] colors to redshift of galaxies for high-EW [OIII]+Hβ emitters (Smit et al. 2015). Remarkably, despite just ∼1 hour of observations becoming available on these targets, the results were nevertheless striking, with 6-8σ [CII] lines found in two targeted sources, with redshifts $z = 6.8075$ and $z = 6.8540$. Additionally, the [CII] luminosities of the two sources were relatively high, being brighter in [CII] than all ALMA non-QSO targets by factors of ∼2-20.

Encouraged by the high efficiency of the Smit et al. (2018) spectral scan results, we successfully proposed for similar observations for 6 other luminous $z \sim 7$ galaxies (2018.1.00085.S: PI Schouws) to add to the results available from the Smit et al. (2018) program and further refine the spectral scan strategy. The purpose of this paper is to present results from this second pilot. Results from this pilot program and an earlier program from Smit et al. (2018) served as the motivation for the Reionization Era Bright Emission Line Survey (REBELS) ALMA large program (Bouwens et al. 2022) in cycle 7. The REBELS program significantly expanded the strategy employed in these pilot programs to a much larger set of targets, while extending the scan strategy to even higher redshift.

The paper is structured as follows. In §2, we detail the selection of targets for this second pilot program, while also describing the set up and reduction of our spectral scan observations. In §3, we describe the [CII] line search and present our new [CII] detections. We place our detections on the [CII]-SFR relation and examine the [CII]/L_{IR} of our sources. We conclude the Section by examining their kinematics. In §4, we discuss the prospect of deploying the described spectral scan observations to a much larger set of $z > 6$ galaxies. Finally in §5, we summarize our conclusions.

Throughout this paper we assume a standard cosmology with $H_0 = 70$ km s^{-1} Mpc^{-1}, $\Omega_m = 0.3$ and $\Omega_\Lambda = 0.7$. Magnitudes are presented in the AB system (Oke & Gunn 1983). For star formation rates and stellar masses we adopt a Chabrier IMF (Chabrier 2003). Error-bars indicate the 68% confidence interval unless specified otherwise.

3.2 HIGH-REDSHIFT TARGETS AND ALMA OBSERVATIONS

3.2.1 *UltraVISTA Search Field and Photometry*

Our source selection is based on ultradeep near-infrared imaging over the COSMOS field (Scoville et al. 2007) from the third data release (DR3) of UltraVISTA (McCracken et al. 2012). UltraVISTA provides imaging covering 1.4 square degrees (McCracken et al. 2012) in the Y, J, H and Ks filters to ∼24-25 mag (5σ), with DR3 achieving fainter limits over 0.7 square degrees in 4 ultradeep strips. The DR3 contains all data taken between December 2009 and July 2014 and reaches $Y = 26.2$, $J = 26.0$, $H = 25.8$, $K = 25.5$ mag (5σ in 1.2″-diameter apertures). The nominal depth we measure in the Y, J, H, and Ks bands for the UltraVISTA DR3 release is ∼0.1-0.2 mag, ∼0.6 mag, ∼0.8 mag, and ∼0.2 mag, respectively, deeper than in UltraVISTA DR2 release.

The optical data we use consists of CFHT/Omegacam in g, r, i, z (Erben et al. 2009) from the Canada-France-Hawaii Legacy Survey (CFHTLS) and Subaru/SuprimeCam in B_J+V_J+g+r+i+z imaging (Taniguchi et al. 2007). This analysis uses Spitzer/IRAC 3.6μm and 4.5μm observations from S-COSMOS (Sanders et al. 2007), the Spitzer Extended Deep Survey (SEDS: Ashby et al. 2013), the Spitzer-Cosmic Assembly Near-Infrared Deep Extragalactic Survey (S-CANDELS: Ashby et al. 2015), Spitzer Large Area Survey with Hyper-Suprime-Cam (SPLASH, PI: Peter Capak), and the Spitzer Matching survey of the UltraVISTA ultra-deep Stripes (SMUVS, PI: K. Caputi: Ashby et al. 2018). Compared to the original S-COSMOS IRAC data, SPLASH provides a large improvement in depth over nearly the whole UltraVISTA area, covering the central 1.2 square degree COSMOS field to 25.5 mag (AB) at 3.6 and 4.5μm. SEDS and S-CANDELS cover smaller areas to even deeper limits. We also make use of data from SMUVS, which provides substantially deeper Spitzer/IRAC data over the deep UltraVISTA stripes.

Source catalogs were constructed using SExtractor v2.19.5 (Bertin & Arnouts 1996), run in dual image mode, with source detection performed on the square root of a χ^2 image (Szalay et al. 1999) generated from the UltraVISTA YJHK$_s$ images. In creating our initial catalog of $z \sim 7$ candidate galaxies, we started from simply-constructed catalogs derived from the ground-based observations. Prior to our photometric measurements, images were first convolved to the J-band point-spread function (PSF) and carefully registered against the detection image (mean RMS$\sim$0.05″). Color measurements were made in small Kron (1980) like apertures (SExtractor AUTO and Kron factor 1.2) with typical radius $\sim$0.35-0.50″).

We also consider color measurements made in fixed 1.2″-diameter apertures when refining our selection of $z \sim 7$ candidate galaxies. For the latter color measurements, flux from a source and its nearby neighbors (12″×12″ region) is carefully modeled; and then flux from the neighbors is subtracted before the aperture photometry is performed. Our careful modeling of the light from neighboring sources improves the overall robustness of our final candidate list to source confusion. Total magnitudes are derived by correcting the fluxes measured in 1.2″-diameter apertures for the light lying outside a 1.2”-diameter aperture. The relevant correction factors are estimated on a source-by-source basis based on the spatial profile of each source and the relevant PSF-correction kernel. Photometry on the Spitzer/IRAC (Fazio et al. 2004) observations is more involved due to the much lower resolution FWHM = 1.7″ compared to the ground-based data (FWHM = 0.7″). The lower resolution results in source blending where light from foreground sources contaminates measurements of the sources of interest. These issues can largely be overcome by modeling and subtracting the contaminating light using the higher spatial resolution near-IR images as a prior. Measurements of the flux in the *Spitzer*/IRAC observations were performed with the mophongo software (Labbé et al. 2006, 2010a,b, 2013, 2015). The positions and surface brightness distributions of the sources in the coadded JHKs image are assumed to appropriate models and, after PSF matching to the IRAC observations, these models are simultaneously fit to the IRAC image leaving only their normalization as a free parameter. Subsequently, light from all neighbors is subtracted, and flux densities were measured in 2″ diameter circular apertures. The IRAC fluxes are corrected to total for missing light outside the aperture using the model profile for the individual sources. The procedure employed here

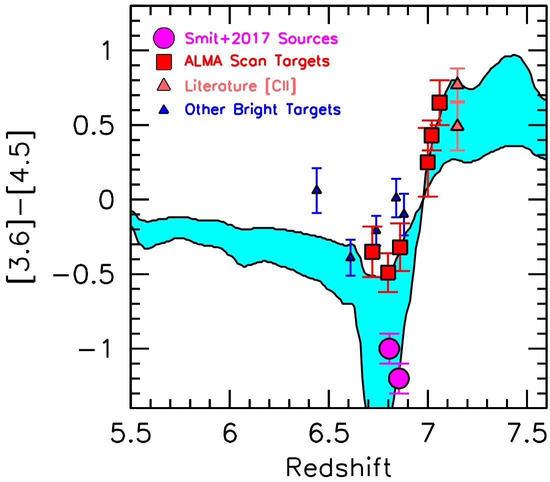

Figure 3.1. Measured [3.6]−[4.5] colors for the bright $z \sim 7$ galaxy candidates we have identified within UltraVISTA. The [3.6]−[4.5] color is largely driven by how high the EWs of the emission lines ([OIII]+Hβ, Hα) that fall in the [3.6] and [4.5] bands are, with the blue colors at $z \sim$ 6.6-6.9 driven by the [OIII]+Hβ lines falling in the [3.6] band, and at $z > 7$ the [OIII]+Hβ lines falling in the [4.5] band. The most promising $z \sim 7$ follow-up targets are indicated by the red squares and correspond to the brightest $H \lesssim 25$ mag sources over COSMOS and show red or blue [3.6]−[4.5] colors, significantly narrowing the width of the redshift likelihood distribution over which [CII] searches are required. The filled magenta circles show the [3.6]−[4.5] colors measured for the two $z \sim 7$ galaxies with [CII] detections reported in Smit et al. (2018), while the solid orange triangles are for sources with [CII] detections in the literature (Matthee et al. 2017; Pentericci et al. 2016; Hashimoto et al. 2019). The blue triangles correspond to those bright ($H \leq 24.5$ mag) $z \sim 7$ galaxies from Appendix A where the redshift is less well constrained based on the [3.6]−[4.5] colors (UVISTA-Z-002, 003, 004, 005, 008). The cyan shaded region shows the expected [3.6]−[4.5] colors for star-forming galaxies vs. redshift assuming a rest-frame equivalent width for [OIII]+Hβ in the range 400Åto 2000Å.

is very similar to those of other studies (e.g., Skelton et al. 2014; Galametz et al. 2013; Guo et al. 2013; Stefanon et al. 2017; Weaver et al. 2022).

3.2.2 *Bright $z \sim 7$ Selection*

In effort to identify a robust set of $z \sim 7$ galaxies from the wide-area UltraVISTA data set for follow-up with ALMA, we require sources to be detected at $>6\sigma$, combining the flux in J, H, Ks, [3.6], and [4.5]-band images (coadding the S/N's in quadrature). The combined UltraVISTA + IRAC detection and SNR requirements exclude spurious sources due to noise, detector artifacts, and diffraction features. We construct a preliminary catalog of candidate z ∼ 7 galaxies using those sources that show an apparent Lyman break due to absorption of UV photons by neutral hydrogen in the IGM blueward of the redshifted Lyα line. This break is measured using simple color criteria. At $z > 6.2$, the z-band flux is significantly impacted by this absorption of rest-UV photons, while at $z > 7.1$, the Y-band flux is impacted. The following criteria were applied:

$$(z - Y > 0.5) \wedge (Y - K < 0.7)$$

where $\wedge$ is the logical AND operator. In case of a non-detection, the z or Y-band flux in these relations is replaced by the equivalent 1σ upper limit.

It is worth emphasizing that our final sample of $z > 6$ bright galaxies shows little dependence on the specific limits chosen here. For each candidate source the redshift probability distribution P(z) is then determined using the EAZY photometric redshift software (Brammer et al. 2008), which fits a linear combination of galaxy spectral templates to the observed spectral energy distribution (SED).

The template set used here is the standard EAZY v1.0 template set, augmented with templates from the Galaxy Evolutionary Synthesis Models (GALEV: Kotulla et al. 2009) which include nebular continuum and emission lines. The implementation of nebular lines follow the prescription of Anders & Fritze-v. Alvensleben (2003), assuming $0.2\,Z_\odot$ metallicity and a large rest-frame EW of Hα = 1300Å. These extreme EW reproduce the observed [3.6]−[4.5] colors for many spectroscopically confirmed $z \sim$ 7-9 galaxies (e.g., Ono et al. 2012; Finkelstein et al. 2013; Oesch et al. 2015; Zitrin et al. 2015; Roberts-Borsani et al. 2016; Stark et al. 2017). A flat prior on the redshift is assumed.

To maximize the robustness of candidates selected for our $z \sim 7$ samples, we require the integrated probability beyond $z = 6$ to be >70%. The use of a redshift likelihood distribution $P(z)$ is very effective in rejecting faint low-redshift galaxies with a strong Balmer/4000Å break and fairly blue colors redward of the break.

The available optical observations are used to reject other low redshift sources and Galactic stars by imposing $\chi^2_{opt} < 4$. χ^2_{opt} is defined as $\chi^2_{opt} = \Sigma_i \mathrm{SGN}(f_i)(f_i/\sigma_i)^2$ where f_i is the flux in band i in a consistent aperture, σ_i is the uncertainty in this flux, and SGN(f_i) is equal to 1 if $f_i > 0$ and −1 if $f_i < 0$. χ^2_{opt} is calculated in both 0.8″-diameter apertures and in scaled elliptical apertures. χ^2_{opt} is effective in excluding z = 1-3 low-redshift

Table 3.1. Main parameters of the ALMA observations used for this study.

Source Name	RA	DEC	Beamwidth[a] (arcsec)	Integration time[b] (min.)	PWV (mm)	Frequency/Redshift Range of the Spectral Scan Percentage of $p(z)^d$ (GHz)
UVISTA-Z-001	10:00:43.36	02:37:51.3	$1.47'' \times 1.21''$	39.31	3.3	228.62 - 239.37 ($z = 6.94$-7.31) (71%)
UVISTA-Z-007	09:58:46.21	02:28:45.8	$1.40'' \times 1.19''$	32.76	1.9	240.28 - 251.02 ($z = 6.57$-6.91) (82%)
UVISTA-Z-009	10:01:52.30	02:25:42.3	$1.38'' \times 1.20''$	32.76	1.9	240.28 - 251.02 ($z = 6.57$-6.91) (65%)
UVISTA-Z-010	10:00:28.12	01:47:54.5	$1.44'' \times 1.18''$	39.31	3.3	228.62 - 239.37 ($z = 6.94$-7.31) (90%)
UVISTA-Z-013	09:59:19.35	02:46:41.3	$1.45'' \times 1.18''$	39.31	3.3	228.62 - 239.37 ($z = 6.94$-7.31) (99%)
UVISTA-Z-019	10:00:29.89	01:46:46.4	$1.39'' \times 1.18''$	32.76	1.9	240.28 - 251.02 ($z = 6.57$-6.91) (95%)

NOTE— [a] Beamsize for the naturally weighted moment-0 images. [b] Corresponds to the average on-source integration time for the two tunings. [c] Average precipitable water vapour during the observations. [d] Percentage of the redshift probability distribution that is covered by the spectral scan.

star-forming galaxies where the Lyman break color selection is satisfied by strong line emission contributing to one of the broad bands (e.g. van der Wel et al. 2011; Atek et al. 2011). Sources which show a 2σ detection in the available ground-based imaging bands (weighting the flux in the different bands according to the inverse square uncertainty in f_ν) are also excluded as potentially corresponding to lower-redshift contaminants. Finally, to minimize contamination by low-mass stars, we fit the observed SEDs of candidate $z \sim 7$ galaxies both with EAZY and with stellar templates from the SpecX prism library (Burgasser et al. 2004). Sources which are significantly better fit ($\Delta\chi^2 > 1$) by stellar SED models are excluded. The SED templates for lower mass stars are extended to 5μm using the known $J - [3.6]$ or $J - [4.5]$ colors of these spectral types (Patten et al. 2006; Kirkpatrick et al. 2011) and the nominal spectral types of stars from the SpecX library. The approach we utilize is identical to the SED-fitting approach employed by Bouwens et al. (2015) for excluding low-mass stars from the CANDELS fields. Combined, these selection requirements result in very low expected contamination rates.

Using the above selection criteria, we select 32 $z \sim 7$ potential candidates for spectral scans over a 1.2 square degrees area in the UltraVISTA field. The sources have an H-band magnitude ranging from 23.8 mag to 25.7 mag and redshifts 6.6 to 7.1. We include a list of the sources we select in Table 3.3 from Appendix A.

3.2.3 *Target Selection for the ALMA Observations*

In an effort to further demonstrate the potential of spectral scans with ALMA to characterize massive star-forming galaxies at $z \sim 7$, we elected to target six sources from the $z \sim 7$ galaxy sample constructed in the previous Section (and which is presented in Appendix A).

We focused on those galaxies which are brightest in the rest-frame UV and have the tightest constraints on their photometric redshifts. UV-bright galaxies are particularly useful to target since those sources have the highest apparent SFRs and should contain particularly luminous [CII] lines, assuming the De Looze et al. (2014) relation holds out to $z > 6$ as Schaerer et al. (2020) find. If there is an additional contribution from obscured star formation, the luminosity of [CII] should be further enhanced.

Additionally, it is useful to target sources with tight constraints on their redshifts from photometry to minimize the number of spectral scan windows that need to be utilized. For this purpose, a useful set of sources to target are those with particularly strong constraints on their photometric redshifts from their *Spitzer*/IRAC colors. One particularly interesting opportunity exists for sources where the broad-band Lyman-break places sources around a redshift $z \sim 7$, as Smit et al. (2015) and Smit et al. (2018) have already demonstrated. This is due to the fact that at $z \sim 7$, the *Spitzer*/IRAC color can reduce the width of the redshift likelihood window for a source by as much as a factor of 2. Due to the dramatic impact the [OIII]+Hβ lines have on the [3.6]−[4.5] colors for star-forming galaxies at $z \sim 7$, the *Spitzer*/IRAC color places robust constraints on the redshift of a source. For sources with a robustly red *Spitzer*/IRAC [3.6]−[4.5] color, we can eliminate the $z < 7$ solution, while for sources with a robustly blue *Spitzer*/IRAC [3.6]−[4.5] color, we can eliminate the $z > 7$ solution.

Following from these arguments, the best targets for the detection of luminous [CII] line emission at $z > 6$ are those sources (1) which are bright ($H < 25$), (2) have photometric Lyman breaks around $z \sim 7$, and (3) have robustly red or blue colors ($|[3.6]-[4.5]| - 1\sigma > 0.0$). We highlight these sources in a *Spitzer*/IRAC [3.6]−[4.5] color vs. redshift diagram in Figure 3.1 as the large red squares.

The [OIII]+Hβ equivalent widths derived from the IRAC colours of our selected sources are shown in table 3.2. Because of the color requirement, the average EW of our sources (1155Å) is significantly higher than the median EW (759^{+112}_{-113} Å) of the population of luminous $z \sim 7$ derived by Endsley et al. (2021).

It should be noted that red rest-frame optical colours could also be driven by strong Balmer breaks resulting from the presence of older stellar

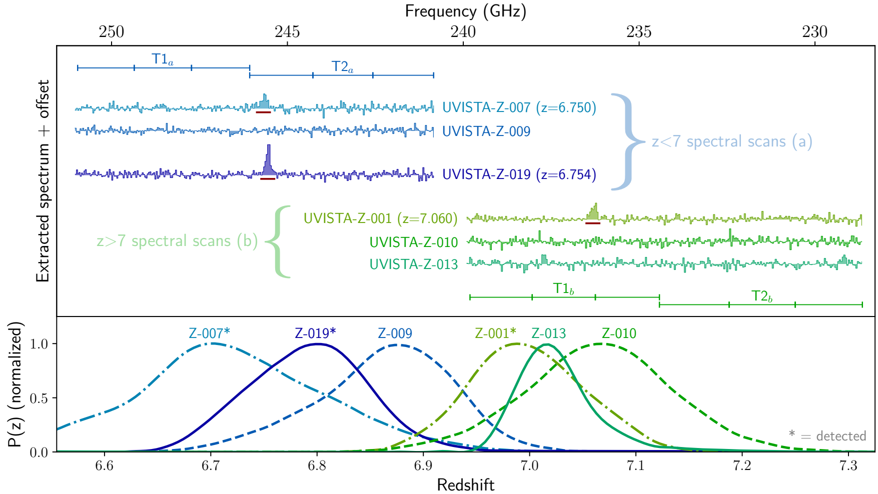

Figure 3.2. *(Top)* Full spectral scans as observed for the six galaxies targeted in this study. The targets are divided in two samples of three galaxies which were observed with different ALMA tunings. For both samples the ALMA tunings are shown above or below the spectral scans. We detect an emission line for 3 targets, indicated with a red line below the location of the emission line in the scans. For clarity, the spectra are binned combining 5 spectral channels. *(Bottom)* Photometric redshift probability distributions for the galaxies targeted in this study (on the same scale as the spectral scans). Galaxies for which an emission line is detected are indicated with an asterisks. The two samples with different ALMA tunings are distinguished with blue and green colors.

populations (Hashimoto et al. 2018; Roberts-Borsani et al. 2020; Strait et al. 2020). However, the presence of a possible Balmer break (rest-frame 3646Å) starts impacting the observed IRAC color from $z \gtrsim 7.6$ after it moves into the 3.6μm channel. Because our galaxies have photometric redshifts below this, we will assume that observed IRAC colours are driven by [OIII]+Hβ emission.

3.2.4 *ALMA Observations and Data Reduction*

A summary of the ALMA data collected for this second pilot program is presented in Table 3.1. ALMA observations were obtained over a contiguous 10.75 GHz range (2 tunings) to scan for [CII] line. For the three targets with photometric redshifts $z \lesssim 7$, the redshift range $z = 6.57$ to 6.91 was scanned (240.28 to 251.02 GHz). For the targets with photometric redshifts $z \gtrsim 7$, the redshift range $z = 6.94$ to 7.31 was scanned (228.62

Table 3.2. Results - UV and ALMA derived properties of the galaxies targeted in this study.

Source Name	z_{phot}	z_{spec}	L_{UV} † ($arcsec$)	log M_* † $M_\odot$	EW OIII+Hβ‡ (Å)	L_{IR} ^{a} ($10^{11} L_\odot$)	$S_\nu \Delta v$ ($Jy\ km/s$)	$L_{[CII]}$ ($10^8 L_\odot$)	FWHM^b (km/s)
UVISTA-Z-001	$7.00^{+0.05}_{-0.06}$	7.0599(3)	$2.9^{+0.1}_{-0.1}$	$9.58^{+0.09}_{-0.35}$	1004^{+442}_{-206}	$5.0^{+2.1}_{-2.1}$	0.57±0.08	6.7 ± 1.2	256 ± 27
UVISTA-Z-007	$6.72^{+0.10}_{-0.09}$	6.7496(5)	$1.5^{+0.2}_{-0.2}$	$9.57^{+0.35}_{-0.44}$	761^{+530}_{-168}	$< 2.2^c$	0.51±0.09	5.6 ± 1.4	301 ± 42
UVISTA-Z-009	$6.86^{+0.07}_{-0.06}$	-	$1.6^{+0.2}_{-0.2}$	$9.40^{+0.32}_{-0.29}$	1012^{+677}_{-257}	< 2.4	-	$<1.6^d$	-
UVISTA-Z-010	$7.06^{+0.07}_{-0.07}$	-	$1.1^{+0.2}_{-0.2}$	$8.88^{+0.28}_{-0.09}$	1706^{+780}_{-807}	< 2.1	-	$<1.7^d$	-
UVISTA-Z-013	$7.02^{+0.03}_{-0.03}$	-	$1.4^{+0.4}_{-0.3}$	$10.72^{+0.03}_{-0.10}$	1821^{+4364}_{-1142}	< 2.2	-	$<1.9^d$	-
UVISTA-Z-019	$6.80^{+0.05}_{-0.06}$	6.7534(2)	$1.0^{+0.1}_{-0.1}$	$9.51^{+0.19}_{-0.18}$	628^{+226}_{-99}	$2.7^{+0.9}_{-0.9}$	0.80±0.06	8.8 ± 0.9	184 ± 15

NOTE— † UV-Luminosities and stellar masses are taken from Schouws et al. (2022) and were derived using the methodology described in Stefanon et al. (2019), assuming a metallicity of 0.2 $Z_\odot$, a constant star formation history and a Calzetti et al. (2000) dust law. ‡ [OIII]+Hβ equivalent widths are taken from Bouwens et al. (2022) and Stefanon et al. (2022, in prep). ^{a} Total infrared luminosity integrated from 8-1000μm assuming a modified black body SED with a dust temperature of 50 K and a dust emissivity index β_{dust}=1.6 after correcting for CMB effects (we refer to Schouws et al. 2022, for details). ^{b} Observed FWHM of the [CII] emission line as measured in the 1d spectrum. ^{c} UVISTA-Z-007 shows dust continuum emission at a level of 2.5σ (corresponding to $L_{IR} \sim 1.8 \times 10^{11} L_\odot$), but we use the 3$\sigma$ upper limit on the luminosity for the remainder of our analysis to be conservative. ^{d} These non-detections are either caused by a [CII] luminosity below our detection limit or because their redshift falls outside of the range scanned in this study (see table 3.1). Denoted is the average limiting luminosity over the scanned redshift range (<5.2σ, assuming 350km/s FWHM[a]), but atmospheric absorption can increase this limiting luminosity with a factor ∼2×, see Figure 3.7.

[a]The limiting luminosity scales with the square root of FWHM, i.e. broader lines are more difficult to detect. We have verified that the assumed FWHM does not significantly impact the results presented in this paper.

to 239.37 GHz). This observing set-up utilizing the same scan windows for multiple targets was chosen to enable a significant reduction in calibration overheads from ALMA by targeting multiple sources in the same science goal. The scan windows utilized are presented in Figure 3.2, along with the redshift likelihood distribution inferred from our photometry. These scan windows cover between 71% to 99% of the estimated redshift likelihood distribution (Table 3.1). The required integration times for the observations were set assuming a similar [CII] luminosity and line width for sources as in pilot program observations of Smit et al. (2018), i.e., $\sim 4\times10^8$ $L_\odot$ and 200 km/s for the FWHM of [CII]. To detect this line at $>5\sigma$, we required achieving a sensitivity of 300 μJy per 66 km/s channel. To achieve this sensitivity, we require ∼ 33 to 39 minutes of integration time with ALMA.

The ALMA data were reduced and calibrated using CASA version 5.4.1 following the standard ALMA pipeline procedures. To reduce the data-size of the visibility measurement set, we averaged the data in bins of 30 seconds after carefully calculating that this bin-size does not impact our data through time-average smearing (e.g. Thompson, Moran & Swenson 2017). We then performed initial imaging of the full data-cube using the TCLEAN task with natural weighting. We clean to a depth of 3σ per channel

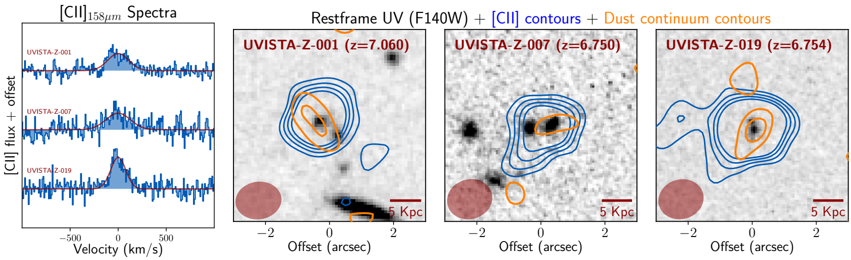

Figure 3.3. Overview of the galaxies detected in [CII] in this study. (*left panel*) 1d extracted spectra of the [CII] line (*blue*) and a Gaussian fit (*red*) for UVISTA-Z-001 (*top*), UVISTA-Z-007 (*middle*) and UVISTA-Z-019 (*bottom*). (*right panels*) The spatial distribution of the [CII] line emission (*blue contours*) relative to rest-UV images of the sources from HST (*F140W*: *background image*) and dust continuum emission (*orange contours*). Contours correspond to 2, 3, 4, and 5× the noise level. The dust continuum is significantly detected in UVISTA-Z-001 and UVISTA-Z-019 and marginally detected in UVISTA-Z-007 (at 2.5σ) (see also Schouws et al. 2022, for an extensive discussion of the continuum properties of these galaxies).

and use automasking[1] to identify regions that contain emission. This initial data-cube was used to do an inital search for [CII] line candidates, details of our line-search procedure are described in the next Section.

If a significant emission line candidate is identified, we use the line properties to carefully mask the channels containing line emission to produce a continuum subtracted visibility data-set using the UVCONTSUB task. This continuum subtracted measurement set is then used to re-image the full data cube, after which we repeat the line search and verify that the same line candidates are obtained.

For each emission line candidate we produce an initial moment-0 image, including channels that fall within 2× the initial FWHM estimate of the line candidate[2]. Using this moment-0 map, we produce a 1d spectrum where we include all pixel-spectra that correspond to $> 3\sigma$ emission in the moment-0 map and we weigh the contribution of each pixel-spectrum by their signal-to-noise level. We then fit a Gaussian line model to this spectrum to extract the central frequency and the FWHM. Next, using this updated estimate for the FWHM, we update the moment-0 image and its associated signal-to-noise weighted 1d spectrum. We perform this 10 times

[1] For the automasking we use the recommended settings for the 12-meter array with compact baselines from the CASA automasking guide: . We verified that the automasking identifies the same emission regions that we would have selected when masking by hand.

[2] Collapsing over all channels that fall within 2× the FWHM captures ~98% of the flux for lines with a Gaussian line-profile.

and note that it converges to a stable solution within a few iterations. The line parameters that we derive with this method are also used to carefully exclude line emission from the continuum imaging used in Schouws et al. (2022).

3.3 RESULTS

3.3.1 *[CII] Line Search*

We performed a systematic search for emission line candidates using the MF3D line search algorithm (Pavesi et al. 2018). MF3D finds line candidates using Gaussian template matching, which accounts for both spectrally and spatially extended emission lines. We used MF3D with 10 frequency templates with line-widths ranging from 50 to 600 km/s and 10 spatial templates ranging from 0 to 4.5 arcseconds. To be considered a reliable detection, we require line candidates to be within 1.5″ of the rest-frame UV position of our sources and have SNR>5.2σ. This criterion was found to result in >95% purity (Schouws et al. in prep.)[3].

We require this high purity because our sources lack a prior spectroscopic redshift. A correct determination of the spectroscopic redshift is of particular importance for potential follow-up studies looking at other emission lines, which would be misguided if the spectroscopic redshift turns out to be incorrect. This strict signal to noise limit however comes at the cost of completeness, missing potential lines that are (just) below the detection limit.

Based on this search, we find reliable emission lines for UVISTA-Z-001 at 12.8σ at 235.80 GHz, for UVISTA-Z-007 at 9.4σ at 245.24 GHz and for UVISTA-Z-019 at 18.3σ at 245.12 GHz. The other datacubes did not contain any line candidates that meet the SNR requirements discussed above. For these non-detections, it is possible that their [CII] luminosity falls below our detection limit ($\sim 2{\times}10^8 L_\odot$, see Figure 3.7) or their redshift falls outside of the range scanned in this study. The results of the line-search are summarized in Figure 3.2, which shows the layout of the full spectral scan and corresponding P(z)'s for all six sources in this study.

For the sources that are not detected in this study, we note that UVISTA-Z-009 has been detected just outside the scan-rage presented in this paper

[3] With a 95% purity we mean that for every 20 detected lines above the SNR threshold, at most one of the line candidates is actually a random noise feature. This threshold is directly derived from the noise statistics of the observed datacubes by comparing the occurrence of negative and positive features at different SNR values (e.g. Béthermin et al. 2020).

at z=6.984 in the REBELS survey (Bouwens et al. 2022, Schouws et al. in prep.). The remaining two non-detections (UVISTA-Z-010 and UVISTA-Z-013) are the sources with the highest [OIII]+Hβ equivalent widths (see Table 3.2). Their high [OIII]+Hβ EWs indicate that these galaxies have a high ionization parameter, which could reduce the abundance of singly ionized carbon to more highly ionized states (e.g. Ferrara et al. 2019). However, studies of [CII] emission from dwarf galaxies in the local universe show that the covering fraction of PDRs and the fraction of [CII] emission from neutral regions increases with ionization parameter (Cormier et al. 2019). Further studies are necessary to explore this for the objects presented in this paper.

For the detected sources we show the contours from the [CII] and dust continuum emission compared to the rest-frame UV morphology and their 1d spectra in Figure 3.3. The rest-frame UV images are in the F140W band at 1.39μm and are from GO-13793 (UVISTA-Z-001, PI:Bowler: Bowler et al. 2017) and GO-16506 (UVISTA-Z-007, UVISTA-Z-019, PI: Witstok; Witstok et al. 2022, in prep). For a detailed description of the procedure we used to produce the moment-0 images and 1d spectra we refer to Section 3.2.4. For the non-detections only ground-based rest-frame UV imaging is available (available in Figure 12 in Schouws et al. (2022) or Figure A1 in Inami et al. (2022).

We measure the integrated flux of the [CII] emission lines from the moment-0 images by fitting the data with a 1-component Gaussian model using the IMFIT task. The resulting flux measurements are shown in Table 3.2. We double-check the measurements from IMFIT with UVMULTIFIT (Martí-Vidal et al. 2014), which we use to fit a Gaussian model in the (u,v)-plane instead of the image-plane. We reassuringly find that both methods produce results consistent within their errorbars. Finally, we convert these [CII] fluxes to luminosities following Solomon et al. (1992) and Carilli et al. (2013):

$$L_{[CII]}/L_{\odot} = 1.04 \times S_{\nu}\Delta\nu \times \nu_{obs} \times D_L^2 \quad (1)$$

with $S_{\nu}\Delta\nu$ the integrated flux density in mJy km/s, ν_{obs} the observing frequency and D_L the luminosity distance.

3.3.2 *The [CII]-SFR Relation*

The large luminosity and favourable atmospheric opacity of [CII] enable detection up to very high redshifts. Local galaxies studies have found a tight correlation between the [CII] luminosity and SFR (De Looze et al.

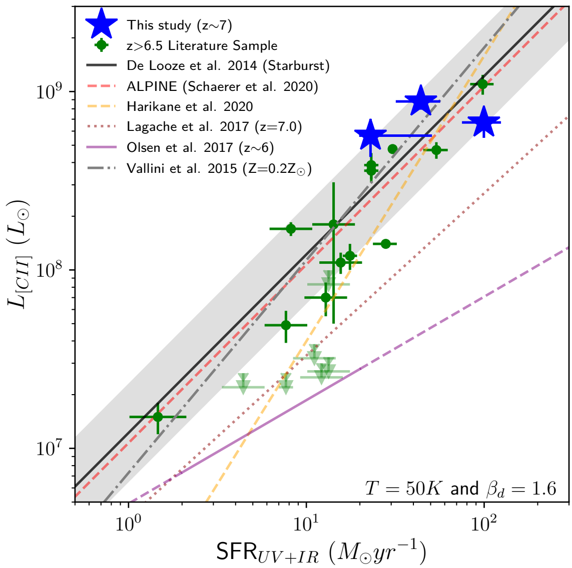

Figure 3.4. [CII]-SFR relation for the galaxies in this study (*solid blue stars*). Our results are consistent with the results from De Looze et al. (2014) for local HII/Starburst galaxies within the scatter (*solid black line and grey shaded region*). For context we show results from previous z>6.5 detections and non-detections (from the compilation by Matthee et al. 2019) (*green data-points and upper-limits*). We also show some fits to the $L_{[CII]}$-SFR relation from the literature for observations (Schaerer et al. 2020; Harikane et al. 2020), semi-analytic models (Lagache et al. 2018, at $z = 7$), and zoom-in simulations by Olsen et al. (2017) and Vallini et al. (2015) (with $Z = 0.2Z_{\odot}$). All SFRs have been scaled to a Chabrier IMF (Chabrier 2003) and IR luminosities are calculated assuming a modified black body curve with $T = 50K$ and $\beta_d = 1.6$ (as described in Schouws et al. 2022).

2011, 2014; Kapala et al. 2014; Cormier et al. 2015; Herrera-Camus et al. 2015; Díaz-Santos et al. 2017), [CII] has therefore been proposed as an efficient and unbiased probe of the SFR at high redshift.

In past few years, this correlation between SFR and $L_{[CII]}$ has been observed out to $z \sim 8$ with an increasing number of detections and upper-limits. Of particular note are the results from the ALPINE large program, which finds little to no evolution in the [CII]-SFR relation in a large sample of normal galaxies at $4.4 < z < 5.9$ (Schaerer et al. 2020). At even higher redshifts the current samples are less uniform, but still seem to be con-

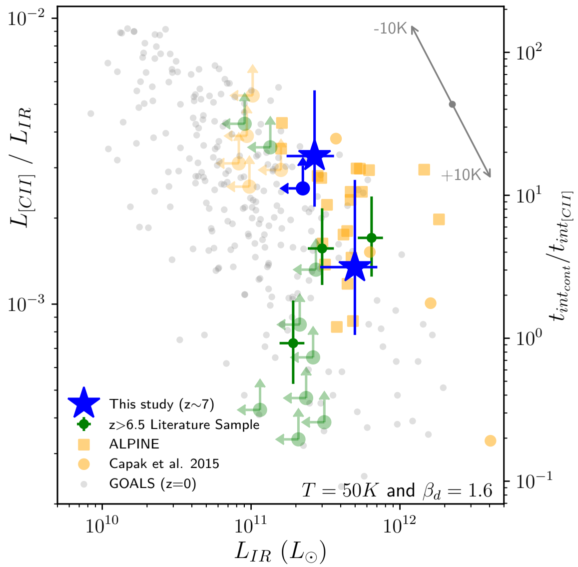

Figure 3.5. Ratio of the observed [CII] luminosity $L_{[CII]}$ to the IR luminosity L_{IR} as a function of L_{IR} for our small $z \sim 7$ galaxy sample (*solid blue stars*, 1σ uncertainties). IR luminosities L_{IR} are estimated assuming a modified blackbody SED with dust temperature 50K and an emissivity index β_d of 1.6. With the grey arrows in the top-right corner we show the effect of changing the assumed dust temperature by $\pm$10K. For context, we also show results from the $z = 0$ GOALS sample (Díaz-Santos et al. 2013, 2017, *grey circles*), the $z \sim$ 4-6 ALPINE sample (Le Fèvre et al. 2020; Béthermin et al. 2020; Faisst et al. 2020, *yellow squares*), and other results from the literature (*green circles*). Lower limits on $L_{[CII]}/L_{IR}$ and upper limits on L_{IR} are 3σ. On the right vertical axis, the ratio of integration times required to detect $[CII]_{158}$ at 5σ to the time required to detect sources in the dust continuum at 3σ is indicated. Our new measurements show slightly higher $L_{[CII]}/L_{IR}$ ratios than the $z = 0$ GOALS results at a given L_{IR} and appear to be qualitatively very similar to the $z \sim$ 4-6 results obtained by ALPINE.

sistent with the local relation, albeit with a larger scatter (e.g., Carniani et al. 2018; Matthee et al. 2019).

Nevertheless, there has been an increasing number of observations of galaxies that fall well below the local relations (e.g., Ota et al. 2014; Matthee et al. 2019; Laporte et al. 2019; Bakx et al. 2020; Binggeli et al. 2021; Uzgil et al. 2021; Rybak et al. 2021; Jolly et al. 2021). Currently, it is not clear what is the driver of this deficit in [CII] luminosity for some high redshift galaxies.

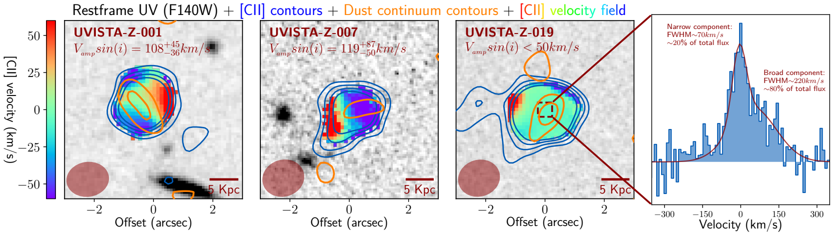

Figure 3.6. (*left three panels*) Low-resolution [CII] kinematics of our sources overlaid on the rest-UV imaging with the [CII] and dust continuum contours, as in Figure 3.3. The velocity gradients for all sources are shown on the same scale, starting at −60 km/s (*blue*) to 60 km/s (*red*). (*rightmost panel*) Zoom-in on the central pixel-spectra of UVISTA-Z-019. The spectrum consists of a narrow component (FWHM $\sim 70km/s$) responsible for $\sim$ 20% of the total flux and a broad component (FWHM $\sim 220km/s$) that accounts for $\sim$ 80% of the total flux.

We show the position of our sources on the [CII]-SFR relation in Figure 3.4, and find that the galaxies targeted in this study are also consistent with the local relation from De Looze et al. (2014) within the expected scatter. The three sources where [CII] remains undetected are not shown on this Figure, since it is unclear whether the [CII] line is below our detection threshold (i.e., $L_{[CII]} < 2 \times 10^8 L_{\odot}$) or whether the true redshift is outside the range of our spectral scan. Because these sources have SFRs between 15 and 25 $M_{\odot}yr^{-1}$ our detection limit falls within the scatter of the local relation (De Looze et al. (2014)). From this Figure, it is clear that most of the $z > 6.5$ galaxies with SFR$\gtrsim 20M_{\odot}yr^{-1}$ are consistent with the local relation, while at lower SFRs a significant fraction of currently observed galaxies seems to fall below the relation.

3.3.3 *[CII] vs. FIR*

It has been found that [CII] can account for up to $\sim$ 1% of the total infrared luminosity of galaxies, however it has also been found that this fraction decreases by $\sim$ 2 orders of magnitude with increasing L_{IR}, leading to a [CII]-deficit in luminous galaxies (e.g., Genzel & Cesarsky 2000; Malhotra et al. 2001; Hodge & da Cunha 2020). Specifically, observed [CII]/FIR ratios range from $\sim 10^{-2}$ for normal z$\sim$0 galaxies to $\sim 10^{-4}$ for the most luminous objects, with a large scatter (e.g., Díaz-Santos et al. 2013).

The reason for this observed [CII]-deficit remains a topic of discussion in the literature, with a large range of possible explanations including optically thick [CII] emission, effects from AGN, changes in the IMF, thermal saturation of [CII], positive dust grain charging and dust-dominated HII region opacities (e.g., Casey et al. 2014; Smith et al. 2016; Ferrara et al. 2019; Rybak et al. 2019; Hodge & da Cunha 2020).

The galaxies in this study have far infrared luminosities of $L_{IR} = 1 - 5 \times 10^{11} L_{\odot}$[4], which puts them in the Luminous Infrared Galaxy (LIRG) classification. Comparing their infrared to their [CII] luminosity we find ratios of $[\mathrm{CII}]/L_{IR} \sim 1 - 3 \times 10^{-3}$ (see Figure 3.5). Compared to local (U)LIRGS from the GOALS survey (Díaz-Santos et al. 2013, 2017), we find that our galaxies are less deficient in [CII] by a factor ∼0.3 dex. This result has a minor dependence on the assumed dust temperature as shown with the grey arrows on Figure 3.5. When assuming higher or lower dust temperatures the data-points move mostly parallel to the trend. Only for substantially higher dust temperatures ($\gtrsim$ 70K) would our measurements be consistent with the local results.

Our measured [CII]/FIR ratios are consistent with other studies at high redshifts, which also find that high redshift galaxies tend to be less [CII] deficient (e.g., Capak et al. 2015; Schaerer et al. 2020). A possible explanation for this lack of [CII]-deficit in high redshift galaxies could be different dust conditions. Specifically, a lower dust-to-gas ratio at a fixed far infrared luminosity could increase the [CII] luminosity with respect to the infrared (Capak et al. 2015).

3.3.4 *[CII] Kinematics*

Due to its high intrinsic luminosity, [CII] is an efficient tracer of the kinematics of high redshift galaxies (e.g., Neeleman et al. 2019). To investigate the kinematics of our sources, we derive the velocity maps of our galaxies by fitting Gaussians to the pixel-spectra in our cube, including all pixels for which the uncertainty on the velocity is less than 50 km/s. The resulting velocity fields are shown in Figure 3.6. Despite the low (∼1.3″, see Table 3.1) resolution of our observations, some of our sources show significant velocity gradients.

In particular, we find that both UVISTA-Z-001 and UVISTA-Z-007 display a significant velocity gradient, with velocity amplitudes of $v_{amp} \sin(i) = 108^{+45}_{-36}$ km/s and $v_{amp} \sin(i) = 119^{+87}_{-50}$ km/s respectively[5].

[4] To calculate the far infrared luminosities we assume a modified black body dust-SED with $T = 50$K and $\beta = 1.6$, see Schouws et al. (2022) for details.

[5] We derive $v_{amp} \sin(i)$ by fitting a rotating thin disk model to the 3D datacube using forward modeling with our kinematics fitting code Skitter (Schouws et al., in prep.). The maximum

If we compare the observed rotational velocities assuming no correction for inclination ($i = 0$, hence $v_{obs} = v_{amp} \sin(i)$) to the total line-width of the 1d spectrum (σ_{obs}) (see Table 3.2 and Figure 3.6), we find that the v_{obs}/σ_{obs} are $1.0^{+0.6}_{-0.4}$ and $0.9^{+0.9}_{-0.5}$ respectively. This would mean that both sources should most likely be classified as rotation dominated (defined as $v_{obs}/\sigma_{obs} > 0.8$ as utilized in e.g. Förster-Schreiber et al. 2009). This calculation does not assume a correction for the inclination of the system, which would increase v_{obs}/σ_{obs}. The observed velocity gradient could however also be caused by close mergers. At the current resolution, rotating disks are indistinguishable from mergers (e.g. Jones et al. 2021, Schouws et al., in prep).

In particular, we find indications that UVISTA-Z-007 could be a merger. The HST F140W imaging (Witstok et al. in prep.) shows clearly that this source consists of two distinct components (see Figure 3.3). The observed velocity gradient is in the same direction as the two UV components (as shown in Figure 3.6), making it likely that the observed velocity gradient in the [CII] is in fact due to the merger of these two components.

The HST F140W imaging of UVISTA-Z-001 also consists of 2 components with consistent photometric redshifts (Bowler et al. 2017). However, for this source the observed velocity gradient is perpendicular to the direction of the two components. Moreover, it seems that the [CII] emission, as well as the dust continuum emission primary originate from the northern most component. This is despite the similarity of their rest-frame UV properties (Bowler et al. 2017). The reason for this discrepancy between the FIR properties of both components will require more detailed observations.

For UVISTA-Z-019 we do not observe a significant velocity gradient and constrain the maximum rotation velocity to $v_{amp} sin(i) < 50$ km/s, implying that this system is either dominated by dispersion or a face-on system ($i = 0$). A more detailed look at the pixel-spectra within the cube indicates that in the central part of this source, the [CII] emission seems to break down into two distinct components (rightmost panel on Figure 3.6), consisting of a narrow component (FWHM ~ 70 km/s) responsible for $\sim 20\%$ of the total flux and a broad component (FWHM ~ 220 km/s) that accounts for $\sim 80\%$ of the total flux.

velocities on the kinematics maps shown in Figure 3.6 are lower than the actual $v_{amp} \sin(i)$ due to beam-smearing effects.

This interesting spectral feature could be caused by several processes, such as the effect of an outflow. However, this would imply that the majority of the [CII] luminosity originates from the outflow and that the emission from the galaxy would have a very narrow FWHM, implying a low dynamical mass, lower than the stellar mass ($M_{dyn} \sim 9 \times 10^8\ M_{\odot}$[6] versus $M_* \sim 3 \times 10^9\ M_{\odot}$). An alternative explanation for the spectral feature could be a minor-merger, where the narrow component originates from an in-falling galaxy. However, this would mean that the LOS velocity is rather small at only $\Delta V \sim 50$ km/s, despite this likely being one of the final stages of the merger. Indeed, HST morphology tentatively shows two close components separated by ~1.5 kpc (see also Figure 3.3). Finally, the kinematics could also be evidence for a bright clump of intense star formation within a larger system, indicating the complex structure of high redshift sources (e.g., Kohandel et al. 2019, 2020). Hence an alternative interpretation of the clumps in HST imaging could be the presence of multiple star-forming regions in a larger system. Higher spatial resolution ALMA observations or deep rest-frame optical observations with JWST would be invaluable to definitively distinguish between these scenarios.

3.4 THE EFFICIENCY OF SPECTRAL SCANS AND FUTURE PROSPECTS

In this study we have obtained redshifts for three galaxies without a prior spectrocopic redshift. In particular by targeting UV-luminous galaxies with high SFRs, the [CII] lines we detect are also luminous. In Figure 3.7 we show that the [CII] emission of our sources could have been detected at $>5\sigma$ in only ~ 20 minute integrations per tuning with ALMA[7].

Our sources benefit from very tight constraints on the photometric redshift due to the large break in the IRAC colors (see Figure 3.1), which enables us to cover a significant fraction of the $P(z)$ with only 2 tunings. For sources that lack this additional constraint, 3 or 4 tunings would be necessary to cover the $P(z)$ appropriately. Nevertheless, this would still mean that galaxies like the ones targeted in this study could be spectroscopically confirmed in less than < 1.5 hours per source.

[6] We derive dynamical masses following Wang et al. (2013): $\frac{M_{dyn}}{M_{\odot} sin(i)} = 1.94 \times 10^5 \cdot (\frac{FWHM}{km/s})^2 \cdot \frac{r_{1/2}}{kpc}$ where $FWHM$ is the full width half maximum of the [CII] line in km/s and $r_{1/2}$ the [CII] half light radius in kpc. Because the narrow [CII] component is unresolved, we assume a size of $r_{1/2} \sim 1$ kpc (consistent with Bowler et al. 2017).

[7] Based on the ALMA sensitivity calculator: https://almascience.eso.org/proposing/sensitivity-calculator and the ALMA Cycle 8 Technical Handbook: https://almascience.nrao.edu/documents-and-tools/cycle8/alma-technical-handbook

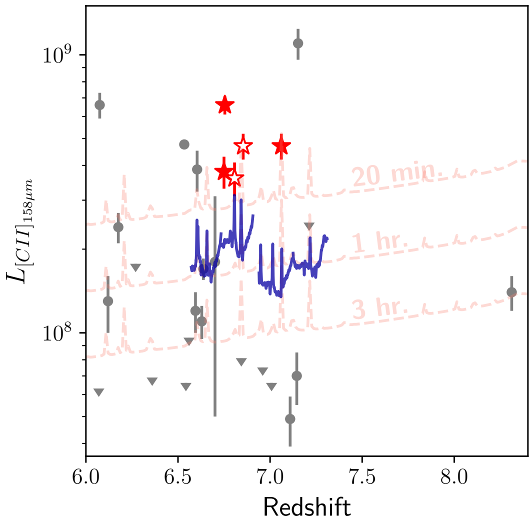

Figure 3.7. In this study we have presented a method to identify and efficiently spectroscopically confirm the redshifts of luminous [CII] emitting galaxies (*solid (this study) and open (Smit et al. 2018) red stars*). We compare the derived luminosities of our sources to the literature (*grey datapoints and upper-limits*). The present compilation is from Matthee et al. (2019) and Bakx et al. (2020). The newly discovered lines are more luminous than most previous detections. The luminosities of those sources without [CII] detections are less clear, but for those sources where our scans cover the full likelihood distribution, it is likely that the lines are fainter and more in line with the typical sources. For context we show the expected limiting luminosities (for a 5.2σ detection and 350 km/s FWHM) that can be achieved with ALMA with 20, 60 and 180 minute integrations (*red dashed lines*) and find that our targets could have been detected in as little as 20 minutes per scan-window. We also indicate the achieved depth of our observations (30-40 minutes) with the *solid blue lines.* This demonstrates the great potential to use ALMA for spectral scans to obtain spectroscopic redshifts of UV-luminous galaxies in the epoch of reionization.

It should be noted though that for sources with a lower SFR (and hence lower [CII] luminosities), spectral scanning becomes expensive quickly. A spectral scan targeting an L_* galaxy ($SFR_{UV} \sim 8M_\odot/yr$ at $z = 7$) would cost $\sim$ 12 hours on source adopting the De Looze et al. (2014) $L_{[CII]}$-SFR relation. Therefore, to study the [CII] emission from $L \leq L_*$ galaxies, either targeting lensed galaxies for spectral scans or following-up galaxies with a prior spectroscopic redshift (e.g. from JWST or ground-based Lyman-α) remain the most suitable options.

One significant advantage of using a spectral scan strategy is the time spent integrating in regions of the spectra not containing prominent ISM cooling lines. These integrations allow us to probe continuum emission from our targets. This is important – since the continuum is much harder to detect than [CII], as one can see from the [CII]/L_{IR} ratios of our sources. This is illustrated in Figure 3.5 (right vertical axis), on which we show the ratio of the integration time needed to detect the dust continuum versus the [CII] line. We find that it is necessary to integrate up to $\sim 20\times$ longer to obtain a 3σ detection of the dust continuum. This means that the time spent observing tunings that do not contain a spectral line is not wasted, but contributes to the necessary sensitivity to detect the faint dust continuum.

Based on the results presented in this paper and Smit et al. (2018), we proposed and were awarded the time to apply the spectral scan method to a significantly larger sample of galaxies, covering a much larger range in galaxy properties and redshift. The result was the on-going Reionization Era Bright Emission Line Survey (REBELS) large program, in which we pursue spectral scans for [CII] or [OIII] in a sample of 40 $z > 6.5$ galaxies (Bouwens et al. 2022).

3.5 SUMMARY

In this paper we present the results of new ALMA spectral scan observations targeting [CII] in a small sample of six luminous Lyman Break Galaxies at $z \sim 7$. The targeted sources were identified from deep, wide-area near-IR, optical, and *Spitzer*/IRAC observations and are particularly luminous. The targeted sources also feature tight constraints on their redshifts leveraging the abrupt changes that occur in the IRAC colour around $z \sim 7$ (where strong line emission from [OIII]+Hβ shifts from the [3.6] to [4.5] band). This improves the efficiency of the spectral scans by $\sim 2\times$ based on a small number of tunings required to cover the inferred $P(z)$. The present results build on the exciting results from Smit et al. (2018), who previously demonstrated the potential of spectral scans for [CII] with just two sources.

Our main results are summarized below:

- We detect ($> 9\sigma$) [CII] lines for three of the six galaxies we target with our spectral scans (shown in Figure 3.2). The [CII] lines are strong with luminosities between $5.6 \times 10^8 L_\odot$ and $8.8 \times 10^8 L_\odot$. We also observe that the [CII], dust and rest-frame UV emission are well aligned within the resolution of our observation (see Figure 3.3).

- Placing our new detections on the [CII]-SFR relation shows that our sources are consistent with the local relation from De Looze et al. (2014) (for HII/starburst galaxies) (shown in Figure 3.4), and we find slightly higher [CII]/$L_{IR} \sim 1-3\times10^{-3}$ compared to local (U)LIRGS (see Figure 3.5), which is consistent with previous studies of high redshift galaxies.

- Although our observations are taken at a relatively low resolution (∼1.3″), we find that our sources display a broad spectrum of kinematic diversity. One of our sources seems to be rotation dominated, one source is most likely a major merger and one source is dominated by dispersion. We also find possible kinematic evidence for a bright star forming clump within the dispersion dominated source (see Figure 3.6). However, higher resolution observations are necessary to confirm our interpretation of the kinematics of our sources.

- We discuss the lack of evolution of the [CII]-SFR relation found for luminous high redshift galaxies by reviewing the literature on the physical effects that drive the [CII] emission in high redshift galaxies. While one would naively expect a trend towards lower [CII]/SFR values with redshift based on the higher ionization parameter, lower metallicities and higher densities of high redshift galaxies, this is not observed. We speculate that a lower dust-to-gas or dust-to-metal ratio, which increases the [CII] emission, could compensate for those effects.

These new results illustrate the tremendous potential spectral scans with ALMA have for characterizing luminous galaxies in the epoch of reionization (see Figure 3.7), including deriving spectroscopic redshifts for sources, and probing the kinematics and dynamical masses of sources, as well as the dust continuum (Schouws et al. 2022). Results from this data set showed the potential (§3.4) and were important in successfully proposing for the REBELS large program in cycle 7 (Bouwens et al. 2022). Future studies (Schouws et al. 2022, in prep) will significantly add to the current science using that considerable data set.

ACKNOWLEDGEMENTS

We are greatly appreciative to our ALMA program coordinator Daniel Harsono for support with our ALMA program. This paper makes use of the following ALMA data: ADS/JAO.ALMA 2018.1.00085.S. ALMA is a partnership of ESO (representing its member states), NSF (USA) and NINS (Japan), together with NRC (Canada), MOST and ASIAA (Taiwan), and KASI (Republic of Korea), in cooperation with the Republic of Chile. The Joint ALMA Observatory is operated by ESO, AUI/NRAO and NAOJ. Sander Schouws and Rychard Bouwens acknowledge support from TOP grant TOP1.16.057 and a NOVA (Nederlandse Onderzoekschool Voor Astronomie) 5 grant. JH acknowledges support of the VIDI research programme with project number 639.042.611, which is (partly) financed by the Netherlands Organisation for Scientific Research (NWO). HSBA acknowledges support from the NAOJ ALMA Scientific Research Grant Code 2021-19A. JW and RS acknowledge support from the ERC Advanced Grant 695671, "QUENCH", and the Fondation MERAC. RS acknowledges support from an STFC Ernest Rutherford Fellowship (ST/S004831/1). The PI acknowledges assistance from Allegro, the European ALMA Regional Center node in the Netherlands.

APPENDIX

A. BRIGHT SAMPLE OF $Z \sim 7$ GALAXIES USED FOR SELECTING OUR SIX FOLLOW-UP TARGETS

For completeness, we provide the coordinates, magnitudes, [3.6]−[4.5] colors, and photometric redshifts for the full selection of bright $z \sim 7$ candidate galaxies we identified (§3.2.2) within the UltraVISTA field in Table 3.3.

Table 3.3. Candidate $z \sim 7$ galaxies in the UltraVISTA DR3 observations

ID	R.A.	Dec	m_{AB}[a]	[3.6]-[4.5]	z_{phot}[b]	z_{spec}	References[c]
Current Selection of Bright Candidate $z \sim 7$ Galaxies							
UVISTA-Z-001	10:00:43.361	2:37:51.33	23.8±0.1	0.3±0.2	$7.00^{+0.05}_{-0.06}$	7.060†	[2]
UVISTA-Z-002[e]	10:02:06.469	2:13:24.18	24.1±0.1	−0.2±0.1	$6.74^{+0.06}_{-0.06}$		[1,10]
UVISTA-Z-003[e]	10:02:06.701	2:34:21.42	24.2±0.1	−0.1±0.1	$6.88^{+0.08}_{-0.08}$		
UVISTA-Z-004[e]	10:01:36.850	2:37:49.10	24.3±0.1	0.0±0.1	$6.84^{+0.09}_{-0.09}$		[2,10]
UVISTA-Z-005[e]	10:01:58.501	2:33:08.22	24.3±0.1	−0.4±0.1	$6.61^{+0.10}_{-0.10}$		[1,10]
UVISTA-Z-006	10:01:40.688	1:54:52.37	24.4±0.1	0.5±0.2	$7.09^{+0.06}_{-0.05}$	7.152*	[2,9]
UVISTA-Z-007	09:58:46.214	2:28:45.75	24.4±0.1	−0.4±0.2	$6.72^{+0.10}_{-0.09}$	7.750†	
UVISTA-Z-008	09:58:39.762	2:15:03.27	24.4±0.1	0.1±0.2	$6.44^{+0.05}_{-0.05}$		
UVISTA-Z-009[e]	10:01:52.304	2:25:42.27	24.5±0.1	−0.3±0.2	$6.86^{+0.07}_{-0.06}$		[2]
UVISTA-Z-010	10:00:28.121	1:47:54.47	24.5±0.1	0.6±0.2	$7.06^{+0.07}_{-0.07}$		[2]
UVISTA-Z-011[e]	10:00:42.125	2:01:57.10	24.6±0.1	−0.1±0.1	$6.55^{+0.05}_{-0.06}$		[2,10]
UVISTA-Z-013[e]	09:59:19.353	2:46:41.31	24.8±0.2	0.4±0.1	$7.02^{+0.03}_{-0.03}$		[10]
UVISTA-Z-014	09:57:35.723	1:44:56.40	24.8±0.1	–[d]	$7.13^{+0.15}_{-0.16}$		
UVISTA-Z-015	10:00:23.772	2:20:36.98	24.8±0.1	0.8±0.1	$7.07^{+0.03}_{-0.03}$	7.154**	[2,3,4,5,6,7]
UVISTA-Z-016	10:01:54.562	2:47:35.79	24.9±0.2	−1.1±0.9	$6.77^{+0.24}_{-0.26}$		
UVISTA-Z-017	10:00:30.188	2:15:59.71	24.9±0.1	−1.3±0.2	$6.78^{+0.04}_{-0.04}$	6.854***	[1,2,3,4,8,10]
UVISTA-Z-018[e]	10:02:03.811	2:13:25.06	25.0±0.2	−0.6±0.3	$6.81^{+0.12}_{-0.10}$		[2]
UVISTA-Z-019	10:00:29.892	1:46:46.37	25.0±0.2	−0.5±0.1	$6.80^{+0.05}_{-0.06}$	7.753†	
UVISTA-Z-020	10:01:57.140	2:33:48.76	25.0±0.2	−0.6±0.3	$6.73^{+0.12}_{-0.11}$		
UVISTA-Z-021	09:57:36.994	2:05:11.28	25.1±0.2	−0.3±0.3	$6.73^{+0.16}_{-0.16}$		[10]
UVISTA-Z-022	09:59:13.206	2:21:52.51	25.1±0.2	−0.1±0.6	$6.52^{+0.14}_{-0.16}$		
UVISTA-Z-023	09:58:45.961	2:39:05.94	25.1±0.2	−3.4±7.3	$6.76^{+0.13}_{-0.13}$		
UVISTA-Z-024	09:59:04.558	2:11:38.10	25.2±0.2	−0.8±0.4	$6.89^{+0.15}_{-0.14}$		
UVISTA-Z-025	09:58:49.216	1:39:09.70	25.3±0.3	−1.6±0.6	$6.70^{+0.12}_{-0.12}$		[10]
UVISTA-Z-026	10:02:05.967	2:06:46.13	25.3±0.2	−1.4±0.4	$6.74^{+0.06}_{-0.06}$		[10]
UVISTA-Z-027	09:59:22.426	2:31:19.45	25.3±0.2	0.1±0.7	$6.69^{+0.11}_{-0.11}$		[10]
UVISTA-Z-028	10:00:54.819	1:50:05.28	25.3±0.2	−0.1±0.2	$6.67^{+0.18}_{-0.16}$		[10]
UVISTA-Z-029	10:00:41.097	2:29:31.13	25.3±0.2	−0.1±0.1	$6.72^{+0.16}_{-0.17}$		
UVISTA-Z-030	10:02:22.458	2:04:45.72	25.3±0.3	−0.1±0.2	$6.61^{+0.11}_{-0.10}$		
UVISTA-Z-031	09:59:01.407	2:28:02.13	25.4±0.2	−0.9±0.4	$6.61^{+0.19}_{-0.23}$		
UVISTA-Z-032	10:00:22.482	1:45:32.62	25.4±0.2	−1.0±0.4	$6.71^{+0.11}_{-0.17}$		

NOTE— [a] UVISTA *H*-band magnitude. [b] 68% confidence intervals derived by EAzY using the SED template set presented in §3.2.2. [c] References: [1] Tilvi et al. (2013), [2] Bowler et al. (2014); Bowler et al. (2017), [3] Bouwens et al. (2015), [4] Smit et al. (2015), [5] Roberts-Borsani et al. (2016), [6] Pentericci et al. (2016), [7] Stark et al. (2017), [8] Smit et al. (2018), [9] Hashimoto et al. (2019), [10] Endsley et al. (2021). [d] This source fell outside the footprint of the IRAC mosaics used for the source selection in this manuscript. [e] These sources are targeted in the REBELS program (Bouwens et al. 2022). † This paper (ADS/JAO.ALMA 2018.1.00085.S). * Detected in dust continuum, [CII] and [OIII] by Hashimoto et al. (2019) (ADS/JAO.ALMA 2016.1.00954.S) and dust continuum by Bowler et al. (2018) (ADS/JAO.ALMA 2015.1.00540.S) (Big Three Dragons/ B14-65666). ** Detected in [CII] by Pentericci et al. (2016) (ADS/JAO.ALMA 2015.1.01105.S) and Lyman-α by Stark et al. (2017). *** Detected in [CII] by Smit et al. (2018) (ADS/JAO.ALMA 2015.1.01111.S).

REFERENCES

Anders, P., & Fritze-v. Alvensleben, U. 2003, A&A, 401, 1063

Ashby, M. L. N., Willner, S. P., Fazio, G. G., et al. 2013, ApJ, 769, 80

—. 2015, ApJS, 218, 33

Ashby, M. L. N., Caputi, K. I., Cowley, W., et al. 2018, The Astrophysical Journal Supplement Series, 237, 39.

Atek, H., Siana, B., Scarlata, C., et al. 2011, ApJ, 743, 121

Bakx, T. J. L. C., Tamura, Y., Hashimoto, T., et al. 2020, Monthly Notices of the Royal Astronomical Society, 493, 4294.

Bertin, E., & Arnouts, S. 1996, A&AS, 117, 393

Béthermin, M., Fudamoto, Y., Ginolfi, M., et al. 2020, A&A, 643, A2.

Binggeli, C., Inoue, A. K., Hashimoto, T., et al. 2021, A&A, 646, A26.

Bouwens, R. J., Illingworth, G. D., Oesch, P. A., et al. 2015, The Astrophysical Journal, 803, 34.

Bouwens, R. J., Oesch, P. A., Stefanon, M., et al. 2021, AJ, 162, 47

Bouwens, R. J., Smit, R., Schouws, S., et al. 2022, The Astrophysical Journal, 931, 160.

Bowler, R. A. A., Bourne, N., Dunlop, J. S., McLure, R. J., & McLeod, D. J. 2018, Monthly Notices of the Royal Astronomical Society, 481, 1631.

Bowler, R. A. A., Cullen, F., McLure, R. J., Dunlop, J. S., & Avison, A. 2021, arXiv e-prints, arXiv:2110.06236

Bowler, R. A. A., Dunlop, J. S., McLure, R. J., & McLeod, D. J. 2017, Monthly Notices of the Royal Astronomical Society, 466, 3612.

Bowler, R. A. A., Dunlop, J. S., McLure, R. J., et al. 2014, MNRAS, 440, 2810

Bradač, M., Garcia-Appadoo, D., Huang, K.-H., et al. 2017, The Astrophysical Journal, 836, L2.

Brammer, G. B., van Dokkum, P. G., & Coppi, P. 2008, ApJ, 686, 1503

Burgasser, A. J., McElwain, M. W., Kirkpatrick, J. D., et al. 2004, AJ, 127, 2856

Calzetti, D., Armus, L., Bohlin, R. C., et al. 2000, The Astrophysical Journal, 533, 682.

Capak, P. L., Carilli, C., Jones, G., et al. 2015, Nature, 522, 455.

Carilli, C. L., Riechers, D., Walter, F., et al. 2013, ApJ, 763, 120

Carniani, S., Maiolino, R., Smit, R., & Amorín, R. 2018, The Astrophysical Journal, 854, L7.

Carniani, S., Ferrara, A., Maiolino, R., et al. 2020, MNRAS, 499, 5136

Casey, C. M., Narayanan, D., & Cooray, A. 2014, PhR, 541, 45

Chabrier, G. 2003, Publications of the Astronomical Society of the Pacific, 115, 763.

Cormier, D., Madden, S. C., Lebouteiller, V., et al. 2015, A&A, 578, A53.

Cormier, D., Abel, N. P., Hony, S., et al. 2019, A&A, 626, A23

De Looze, I., Baes, M., Bendo, G. J., Cortese, L., & Fritz, J. 2011, MNRAS, 416, 2712

De Looze, I., Cormier, D., Lebouteiller, V., et al. 2014, A&A, 568, A62.

Díaz-Santos, T., Armus, L., Charmandaris, V., et al. 2013, The Astrophysical Journal, 774, 68.

—. 2017, The Astrophysical Journal, 846, 32.

Endsley, R., Stark, D. P., Chevallard, J., & Charlot, S. 2021, MNRAS, 500, 5229

Erben, T., Hildebrandt, H., Lerchster, M., et al. 2009, A&A, 493, 1197.

Faisst, A. L., Fudamoto, Y., Oesch, P. A., et al. 2020, Monthly Notices of the Royal Astronomical Society, https://academic.oup.com/mnras/advance-article-pdf/doi/10.1093/mnras/staa2545/33674766/staa2545.pdf, staa2545.

Fazio, G. G., Hora, J. L., Allen, L. E., et al. 2004, ApJS, 154, 10

Ferrara, A., Vallini, L., Pallottini, A., et al. 2019, Monthly Notices of the Royal Astronomical Society, 489, 1.

Finkelstein, S. L., Papovich, C., Dickinson, M. Song, M., et al. 2013, Nature, 502, 524

Finkelstein, S. L., Ryan, R. E., Papovich, C., et al. 2015, The Astrophysical Journal, 810, 71.

Fudamoto, Y., Oesch, P., Faisst, A., et al. 2020, arXiv e-prints, arXiv:2004.10760.

Fudamoto, Y., Oesch, P. A., Schouws, S., et al. 2021, Nature, 597, 489

Förster-Schreiber, N. M., Genzel, R., Bouché, N., et al. 2009, The Astrophysical Journal, 706, 1364.

Galametz, A., Grazian, A., Fontana, A., et al. 2013, ApJS, 206, 10

Genzel, R., & Cesarsky, C. J. 2000, Annual Review of Astronomy and Astrophysics, 38, 761.

Guo, Y., Ferguson, H. C., Giavalisco, M., et al. 2013, ApJS, 207, 24

Harikane, Y., Ouchi, M., Shibuya, T., et al. 2018, ApJ, 859, 84

Harikane, Y., Ouchi, M., Inoue, A. K., et al. 2020, ApJ, 896, 93

Harikane, Y., Ono, Y., Ouchi, M., et al. 2021, arXiv e-prints, arXiv:2108.01090

Hashimoto, T., Laporte, N., Mawatari, K., et al. 2018, Nature, 557, 392.

Hashimoto, T., Inoue, A. K., Mawatari, K., et al. 2019, Publications of the Astronomical Society of Japan, 71, https://academic.oup.com/pasj/article-pdf/71/4/71/29163312/psz049.pdf, 71.

Herrera-Camus, R., Bolatto, A. D., Wolfire, M. G., et al. 2015, The Astrophysical Journal, 800, 1.

Hodge, J. A., & da Cunha, E. 2020, arXiv e-prints, arXiv:2004.00934.

Inami, H., Algera, H. S. B., Schouws, S., et al. 2022, Monthly Notices of the Royal Astronomical Society, 515, 3126.

Ishigaki, M., Kawamata, R., Ouchi, M., et al. 2018, ApJ, 854, 73

Jolly, J.-B., Knudsen, K., Laporte, N., et al. 2021, A&A, 652, A128.

Jones, G. C., Vergani, D., Romano, M., et al. 2021, MNRAS, 507, 3540

Jones, G. C., Vergani, D., Romano, M., et al. 2021, Monthly Notices of the Royal Astronomical Society, 507, 3540.

Kapala, M. J., Sandstrom, K., Groves, B., et al. 2014, The Astrophysical Journal, 798, 24.

Kirkpatrick, J. D., Cushing, M. C., Gelino, C. R., et al. 2011, ApJS, 197, 19

Knudsen, K. K., Richard, J., Kneib, J.-P., et al. 2016, MNRAS, 462, L6

Kohandel, M., Pallottini, A., Ferrara, A., et al. 2020, Monthly Notices of the Royal Astronomical Society, 499, 1250.

—. 2019, Monthly Notices of the Royal Astronomical Society, 487, 3007.

Kotulla, R., Fritze, U., Weilbacher, P., & Anders, P. 2009, MNRAS, 396, 462

Kron, R. G. 1980, ApJS, 43, 305

Labbé, I., Bouwens, R., Illingworth, G. D., & Franx, M. 2006, ApJL, 649, L67

Labbé, I., González, V., Bouwens, R. J., et al. 2010a, ApJL, 708, L26

—. 2010b, ApJL, 716, L103

Labbé, I., Oesch, P. A., Bouwens, R. J., et al. 2013, ApJL, 777, L19

Labbé, I., Oesch, P. A., Illingworth, G. D., et al. 2015, ApJS, 221, 23

Lagache, G., Cousin, M., & Chatzikos, M. 2018, A&A, 609, A130.

Laporte, N., Katz, H., Ellis, R. S., et al. 2019, Monthly Notices of the Royal Astronomical Society: Letters, 487, L81.

Le Fèvre, O., Béthermin, M., Faisst, A., et al. 2020, A&A, 643, A1

Maiolino, R., Carniani, S., Fontana, A., et al. 2015, Monthly Notices of the Royal Astronomical Society, 452, 54.

Malhotra, S., Kaufman, M. J., Hollenbach, D., et al. 2001, The Astrophysical Journal, 561, 766.

Martí-Vidal, I., Vlemmings, W. H. T., Muller, S., & Casey, S. 2014, A&A, 563, A136.

Matthee, J., Sobral, D., Boone, F., et al. 2017, The Astrophysical Journal, 851, 145.

Matthee, J., Sobral, D., Boogaard, L. A., et al. 2019, The Astrophysical Journal, 881, 124.

McCracken, H. J., Milvang-Jensen, B., Dunlop, J., et al. 2012, A&A, 544, A156.

McLure, R. J., Dunlop, J. S., Bowler, R. A. A., et al. 2013, Monthly Notices of the Royal Astronomical Society, 432, 2696.

Neeleman, M., Bañados, E., Walter, F., et al. 2019, The Astrophysical Journal, 882, 10.

Oesch, P. A., Bouwens, R. J., Illingworth, G. D., et al. 2015, The Astrophysical Journal, 808, 104.

Oke, J. B., & Gunn, J. E. 1983, ApJ, 266, 713.

Olsen, K., Greve, T. R., Narayanan, D., et al. 2017, The Astrophysical Journal, 846, 105.

Ono, Y., Ouchi, M., Mobasher, B., et al. 2012, ApJ, 744, 83

Ota, K., Walter, F., Ohta, K., et al. 2014, The Astrophysical Journal, 792, 34.

Patten, B. M., Stauffer, J. R., Burrows, A., et al. 2006, ApJ, 651, 502

Pavesi, R., Sharon, C. E., Riechers, D. A., et al. 2018, ApJ, 864, 49
Pentericci, L., Carniani, S., Castellano, M., et al. 2016, The Astrophysical Journal, 829, L11.
Riechers, D. A., Carilli, C. L., Capak, P. L., et al. 2014, ApJ, 796, 84
Roberts-Borsani, G. W., Ellis, R. S., & Laporte, N. 2020, Monthly Notices of the Royal Astronomical Society, 497, 3440.
Roberts-Borsani, G. W., Bouwens, R. J., Oesch, P. A., et al. 2016, The Astrophysical Journal, 823, 143.
Roberts-Borsani, G. W., Bouwens, R. J., Oesch, P. A., et al. 2016, ApJ, 823, 143
Robertson, B. E. 2021, arXiv e-prints, arXiv:2110.13160
Rybak, M., Rivera, G. C., Hodge, J. A., et al. 2019, The Astrophysical Journal, 876, 112.
Rybak, M., da Cunha, E., Groves, B., et al. 2021, The Astrophysical Journal, 909, 130.
Sanders, D. B., Salvato, M., Aussel, H., et al. 2007, ApJS, 172, 86
Schaerer, D., & de Barros, S. 2009, A&A, 502, 423
Schaerer, D., Ginolfi, M., Béthermin, M., et al. 2020, A&A, 643, A3
Schouws, S., Stefanon, M., Bouwens, R., et al. 2022, The Astrophysical Journal, 928, 31.
Scoville, N., Aussel, H., Brusa, M., et al. 2007, The Astrophysical Journal Supplement Series, 172, 1.
Skelton, R. E., Whitaker, K. E., Momcheva, I. G., et al. 2014, ApJS, 214, 24
Smit, R., Bouwens, R. J., Franx, M., et al. 2015, The Astrophysical Journal, 801, 122.
Smit, R., Bouwens, R. J., Carniani, S., et al. 2018, Nature, 553, 178.
Smith, J. D. T., Croxall, K., Draine, B., et al. 2016, The Astrophysical Journal, 834, 5.
Solomon, P. M., Downes, D., & Radford, S. J. E. 1992, ApJL, 387, L55
Stark, D. P., Ellis, R. S., Chiu, K., Ouchi, M., & Bunker, A. 2010, MNRAS, 408, 1628
Stark, D. P., Ellis, R. S., Charlot, S., et al. 2017, MNRAS, 464, 469
Stefanon, M., Bouwens, R. J., Labbé, I., et al. 2022, The Astrophysical Journal, 927, 48.
Stefanon, M., Yan, H., Mobasher, B., et al. 2017, ApJS, 229, 32
Stefanon, M., Labbé, I., Bouwens, R. J., et al. 2019, arXiv e-prints, arXiv:1902.10713
Strait, V., Bradač, M., Coe, D., et al. 2020, The Astrophysical Journal, 888, 124.
Szalay, A. S., Connolly, A. J., & Szokoly, G. P. 1999, AJ, 117, 68
Taniguchi, Y., Scoville, N., Murayama, T., et al. 2007, ApJS, 172, 9
Tilvi, V., Papovich, C., Tran, K. V. H., et al. 2013, ApJ, 768, 56
Uzgil, B. D., Oesch, P. A., Walter, F., et al. 2021, The Astrophysical Journal, 912, 67.
Vallini, L., Gallerani, S., Ferrara, A., Pallottini, A., & Yue, B. 2015, The Astrophysical Journal, 813, 36.

van der Wel, A., Straughn, A. N., Rix, H. W., et al. 2011, ApJ, 742, 111

Venemans, B. P., Walter, F., Neeleman, M., et al. 2020, ApJ, 904, 130

Wagg, J., Carilli, C. L., Wilner, D. J., et al. 2010, A&A, 519, L1

Walter, F., Riechers, D., Cox, P., et al. 2009, Nature, 457, 699

Wang, R., Wagg, J., Carilli, C. L., et al. 2013, The Astrophysical Journal, 773, 44.

Weaver, J. R., Kauffmann, O. B., Ilbert, O., et al. 2022, ApJS, 258, 11

Willott, C. J., Carilli, C. L., Wagg, J., & Wang, R. 2015, The Astrophysical Journal, 807, 180.

Zitrin, A., Labbé, I., Belli, S., et al. 2015, ApJL, 810, L12

Chapter 4

Detection of $[OIII]_{88\mu m}$ in JADES-GS-z14-0 at z=14.1793

We report the first successful ALMA follow-up observations of a secure $z > 10$ JWST-selected galaxy, by robustly detecting (6.6σ) the $[OIII]_{88\mu m}$ line in JADES-GS-z14-0 (hereafter GS-z14). The ALMA detection yields a spectroscopic redshift of $z = 14.1793 \pm 0.0007$, and increases the precision on the prior redshift measurement of $z = 14.32^{+0.08}_{-0.20}$ from NIRSpec by $\gtrsim 180\times$. Moreover, the redshift is consistent with that previously determined from a tentative detection (3.6σ) of $CIII]_{1907,1909}$ ($z = 14.178 \pm 0.013$), solidifying the redshift determination via multiple line detections. We measure a line luminosity of $L_{[OIII]88} = (2.1 \pm 0.5) \times 10^8\, L_\odot$, placing GS-z14 at the lower end, but within the scatter of, the local $L_{[OIII]88}$-star formation rate relation. No dust continuum from GS-z14 is detected, suggesting an upper limit on the dust-to-stellar mass ratio of $< 2 \times 10^{-3}$, consistent with dust production from supernovae with a yield $y_d < 0.3\, M_\odot$. Combining a previous JWST/MIRI photometric measurement of the [OIII]$\lambda\lambda$4959,5007Å and Hβ lines with Cloudy models, we find GS-z14 to be surprisingly metal-enriched ($Z \sim 0.05 - 0.2\, Z_\odot$) a mere 300 Myr after the Big Bang. The detection of a bright oxygen line in GS-z14 thus reinforces the notion that galaxies in the early Universe undergo rapid evolution.

Schouws, Bouwens, Ormerod, Smit, Algera, Sommovigo,
Hodge, Ferrara, Oesch, Rowland, van Leeuwen, Stefanon,
Herard-Demanche, Fudamoto, Röttgering, and van der Werf
ApJ, 988, 19 (2025)

4.1 INTRODUCTION

The discovery and spectroscopic confirmation of galaxies at $z > 10$ has recently become possible due to the groundbreaking capabilities offered by the James Webb Space Telescope (*JWST*) (e.g. Curtis-Lake et al. 2023; Robertson et al. 2023; Bunker et al. 2023; Carniani et al. 2024; Finkelstein et al. 2024; Zavala et al. 2024). In particular JADES-GS-z14-0 (hereafter GS-z14) was recently spectroscopically confirmed to be the most distant known galaxy at $z_{\rm spec} = 14.32^{+0.08}_{-0.20}$, less than 300 Myr after the Big Bang (Carniani et al. 2024). Notably GS-z14 is also very luminous with $M_{UV} = -20.81 \pm 0.16$, which makes it the second most luminous $z > 8$ galaxy with a spectroscopic redshift; only GN-z11 (Oesch et al. 2016; Bunker et al. 2023) is more luminous by a factor $\sim 2\times$.

Moreover, in contrast to other $z > 10$ galaxies, the rest-frame UV morphology of GS-z14 is extended and not highly concentrated. This implies that the luminosity is dominated by a spatially extended stellar population as opposed to an active galactic nucleus (AGN). The existence of objects like GS-z14 suggests a much more rapid build-up of galaxies in the very early universe than previously expected (Carniani et al. 2024). GS-z14 enables a unique opportunity to study this rapid build-up in detail (Ferrara 2024).

The high luminosity of GS-z14 makes it an exceptional target for multi-wavelength follow-up observations capable of revealing its physical conditions. Here we present new observations of GS-z14 targeting the luminous $[\mathrm{OIII}]_{88\mu m}$ far-infrared line with the the Atacama Large Millimeter/submillimeter Array (ALMA).

The [OIII] 88-micron fine-structure line is one of the dominant coolants of the ISM. It originates from ionized gas in HII regions (Cormier et al. 2015), where ionizing radiation from young, massive stars has stripped electrons from oxygen atoms. Both semi-analytical models (Yang & Lidz 2020; Vallini et al. 2021, 2024) and radiative transfer post-processed large box (Moriwaki et al. 2018), cosmological zoom-in (Katz et al. 2017; Arata et al. 2020; Katz et al. 2022; Pallottini et al. 2022; Kohandel et al. 2023; Nakazato et al. 2023) hydrodynamical simulations have been employed to predict and interpret $[\mathrm{OIII}]_{88\mu m}$ emission in high redshift sources. The consensus is that bright $[\mathrm{OIII}]_{88\mu m}$ emission is generally associated with hard ionisation fields (Yang & Lidz 2020; Pallottini et al. 2022), high ionization parameters (Moriwaki et al. 2018; Arata et al. 2020; Vallini et al. 2024;

Nakazato et al. 2023), and low metallicities (Katz et al. 2019; Vallini et al. 2024). These physical properties are likely to be ubiquitous in very actively star-forming galaxies at high redshifts, making this line the ideal target for ALMA follow-up observations of JWST-selected $z > 10$ galaxies.

In the last two years, ALMA follow-up observations have been performed for several high-redshift galaxy candidates. GHZ2 (Castellano et al. 2022; Naidu et al. 2022; Donnan et al. 2022; Harikane et al. 2023; Bouwens et al. 2023), with a photometric redshift of $z = 11.96 - 12.42$, was targeted with an ALMA Band 6 search for $[\mathrm{OIII}]_{88\mu m}$ by Bakx et al. (2023), who determined a 5σ upper limit of $\log(L_{[\mathrm{OIII}]}/L_{\odot}) < 1.7 \times 10^8$ (see also Popping 2023). GHZ2 was later spectroscopically confirmed at $z = 12.34$ (Castellano et al. 2024), with Zavala et al. (2024) estimating an SFR of $9 \pm 3\, M_{\odot}\,\mathrm{yr}^{-1}$ from the Hα line. Following its spectroscopic confirmation, Zavala et al. (2024) re-examined the ALMA observations of GHZ2 presented in Bakx et al. (2023), but were not able to identify a plausible $>5\sigma$ $[\mathrm{OIII}]_{88\mu m}$ detection at the expected frequency.

An ALMA line scan was also performed on GHZ1, with a photometric redshift of $z \approx 10.6$ (Treu et al. 2023), SFR of $36.3^{+54.5}_{-26.8}\, M_{\odot}\,\mathrm{yr}^{-1}$ and stellar mass $\log(M_{\star}/M_{\odot}) = 9.1^{+0.3}_{-0.4}$ (Santini et al. 2023), yielding a marginal $[\mathrm{OIII}]_{88\mu m}$ signal near its JWST position (Yoon et al. 2023) and an upper limit of $L_{[\mathrm{OIII}]} < 2.2 \times 10^8\, L_{\odot}$ (5σ). Another high-redshift candidate, HD1 at $z = 13.3$ (Harikane et al. 2023) was observed in ALMA Bands 4 and 6 targeting $[\mathrm{CII}]_{158\mu m}$ and $[\mathrm{OIII}]_{88\mu m}$, respectively, but the lines were not detected (Kaasinen et al. 2023). HD1 was later shown to be a low-redshift interloper at $z = 4.0$ (Harikane et al. 2024). Finally, S5-z17-1, identified in JWST ERO data, showed a potential 5.1σ detection at 338.726 GHz, possibly corresponding to $[\mathrm{OIII}]_{52\mu m}$ at $z = 16$ (Fujimoto et al. 2023), suggesting an SFR $< 120\, M_{\odot}\,\mathrm{yr}^{-1}$. However, the high-redshift nature of this galaxy has not been conclusively established.

Overall, these upper limits and non-detections indicate possible lower redshift solutions or insufficient sensitivity in the requested observations (Bakx et al. 2023; Furlanetto & Mirocha 2023; Kaasinen et al. 2023). However, the burstiness of SF in such high-redshift galaxies, as well as the impact of feedback processes on galaxy spectra and visibility, have also been suggested as physical motivations for the lack of ALMA detections at $z > 10$ (Nakazato et al. 2023; Kohandel et al. 2023).

Throughout this paper we assume a standard ΛCDM cosmology with $H_0 = 70$ km s^{-1} Mpc^{-1}, $\Omega_m = 0.3$ and $\Omega_{\Lambda} = 0.7$. Magnitudes are pre-

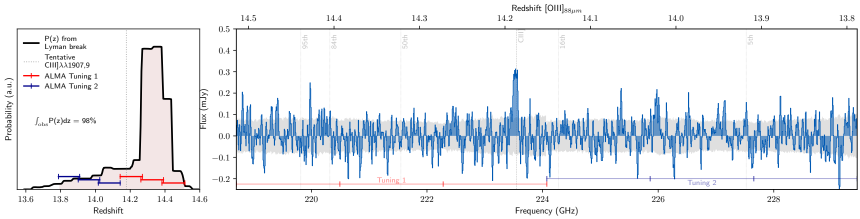

Figure 4.1. *Left Panel:* The ALMA observations cover 98% of the redshift probability distribution derived from the Lyman break as observed by NIRSpec PRISM. We use two tunings with three spectral windows each, tuning 1 and 2 cover 83% and 15% of the probability distribution respectively. *Right Panel:* Flux constraints extracted at the position of GS-z14 (*blue histogram*) vs. frequency from the 2023.A.00037.S spectral scan observations. The grey contours indicate the 1σ uncertainties. For context we show the expected redshift from the tentative CIII]$_{1907,1909}$ line from NIRSpec as well as the 5, 16, 50, 86 and 95th percentiles of the P(z) distribution. There is only one feature in the line scan that can be confidently identified as [OIII]$_{88\mu m}$ line emission and it occurs at a frequency of 223.528±0.009 GHz.

sented in the AB system (Oke & Gunn 1983). For star formation rates and stellar masses we adopt a Chabrier IMF (Chabrier 2003). Error-bars indicate the 68% confidence interval unless specified otherwise. All measured and derived physical quantities are corrected for gravitational lensing by a factor of 1.17× (Carniani et al. 2024). Logarithms use base 10 unless specified otherwise.

4.2 OBSERVATIONS AND DATA-REDUCTION

4.2.1 *JWST*

GS-z14 was discovered in deep imaging of the GOODS-South field obtained by the JWST Advanced Deep Extragalactic Survey (JADES; Eisenstein et al. 2023a) and the First Reionization Epoch Spectroscopic COmplete Survey (FRESCO; Oesch et al. 2023). GS-z14 was initially flagged as a likely low redshift interloper (Hainline et al. 2024; Williams et al. 2024) due to a nearby foreground galaxy at $z = 3.475$ with a separation of only 0.4" and due to its high luminosity. However, further analysis including additional medium-band observations favored a high redshift solution (Robertson et al. 2023).

Deep follow-up spectroscopy with NIRSpec presented in Carniani et al. (2024) shows a strong break at $\sim$1.85μm, consistent with a Lyman break at $z \sim 14$. The profile of the Lyman break is sensitive to absorption of hydrogen along the line of sight, neutral gas in the galaxy and environment, velocity offsets, the presence of Lyman alpha emission and possible ionized bubbles. Accounting for these effects, Carniani et al. (2024) determined a spectroscopic redshift of $z = 14.32^{+0.08}_{-0.20}$.

In contrast to other $z > 10$ sources, the spectrum of GS-z14 does not contain strong rest-frame UV emission lines. Only CIII]$\lambda\lambda$1907,9Å is tentatively detected with a significance of 3.6σ at $z = 14.178 \pm 0.013$, consistent with the redshift obtained from the Lyman Break. Carniani et al. (2024) discuss a number of mechanisms that could be responsible for the lack of strong emission lines in the rest-frame UV, ranging from a sudden quenching of the star formation, very low or high metallicities ($Z<0.05Z_\odot$ or $Z\sim Z_\odot$), a high escape fraction of ionizing photons and a difference in the dominant ionizing flux.

Interestingly, GS-z14 is also detected by MIRI in the F770W filter (Helton et al. 2024). This filter covers the rest-frame optical emission of GS-z14, corresponding to wavelengths of 4.4 to 5.7μm. This part of the spectrum contains the strong [OIII]$\lambda\lambda$4959,5007Å and Hβ emission lines, and indeed the observed flux is significantly stronger than observed in the adjacent F444W filter, implying a significant contribution from the emission lines (constituting about 1/3 of the total F770W flux).

SED fitting of GS-z14 performed by Helton et al. (2024) shows that the photometry is consistent with a stellar mass of $\log(M_*/M_\odot)=8.7^{+0.5}_{-0.4}$. The models estimate that most of this stellar mass was formed relatively recently, with a mass-weighted age of ~20 Myr. Helton et al. (2024) determine the current ($< 10\,$Myr) star formation rate of GS-z14 to be 25^{+6}_{-5} $M_\odot$ yr^{-1}—consistent with the measurement of $22 \pm 6\,M_\odot$ yr^{-1} from Carniani et al. (2024). Combined with the measured size of 260±20 pc, this implies a high star formation rate surface density of ~64 $M_\odot$ yr^{-1} pc^{-2}, comparable to intense starbursting galaxies in the local universe (Genzel et al. 2010). The UV slope $\beta_{UV} = -2.20 \pm 0.07$ indicates the presence of a moderate amount of dust in addition to the very young stellar population, with a visual extinction of $A_V=0.31^{+0.14}_{-0.07}$ (Carniani et al. 2024). Finally, the metallicity is poorly constrained owing to a lack of detected emission lines but is expected to be low ($Z = 0.014^{+0.052}_{-0.012}$ $Z_\odot$; Carniani et al. 2024).

4.2.2 *ALMA*

The ALMA Band 6 follow-up observations targeting the [OIII]$_{88\mu m}$ line were obtained as part of a Cycle 10 Director's Discretionary Time (DDT) program (#2023.A.00037.S, PI: Schouws). An observing set-up using two tunings with three spectral windows each was utilized to maximize the coverage of the redshift likelihood distribution derived from the spectroscopic Lyman break. This results in a continuous frequency coverage ranging from 218.70 GHZ to 229.45 GHz, corresponding to a redshift range of $z = 13.79$ to 14.51. We show in Figure 4.1 that the observing strategy covers 98% of the P(z).

The observations for Tuning 2 were carried out between 15 and 16 August 2024 in good weather conditions (PWV=0.67mm), achieving the requested sensitivity in 2.8 hours. Tuning 1 was observed between 7 and 8 September 2024 for 2.8 hours in excellent conditions (PWV=0.30mm). Both tunings were observed with different array configurations due to scheduling constraints. Tuning 1 was observed in C-4 and Tuning 2 in C-5 with baselines of 15−500 and 15−919 m, resulting in synthesized beams of $1.09'' \times 0.81''$ and $0.57'' \times 0.49''$ respectively when using natural weighting.

The ALMA data were reduced and calibrated following the standard ALMA pipeline procedures with the Common Astronomy Software Applications (v6.5.4-9) (Casa; Hunter et al. 2023). The amplitude and phase calibrations were performed using J0334-4008 and J0348-2749, respectively. Both calibrators are part of the ALMA Calibrator Source Catalogue and are therefore considered reliable for Band 6 observations. Under typical conditions, the absolute flux calibration accuracy for Band 6 is 5–10% (ALMA Technical Handbook 2024). The data were well behaved, with no bad antennas or channels requiring flagging.

The resulting calibrated measurement sets were time-averaged in bins of 30 seconds to reduce the data-size, after carefully verifying that time-average smearing does not impact our results (e.g. Thompson et al. 2017).

Imaging of the calibrated visibilities was performed with natural weighting using the tclean task in Casa, cleaning to a depth of 2σ using automasking (Kepley et al. 2020). We use a pixel scale of $0.076''$ to properly sample the synthesized beam, which has a FWHM of $1.08'' \times 0.80''$ at the frequency of the $[\mathrm{OIII}]_{88\mu m}$ line.

4.2.3 *Line Search*

We perform a blind search for emission lines using an algorithm similar to the one used by Béthermin et al. (2020) for the ALPINE survey (Le Fèvre et al. 2020; Faisst et al. 2020) and Schouws et al. in prep. for the REBELS survey (Bouwens et al. 2022). The algorithm loops over all channels and

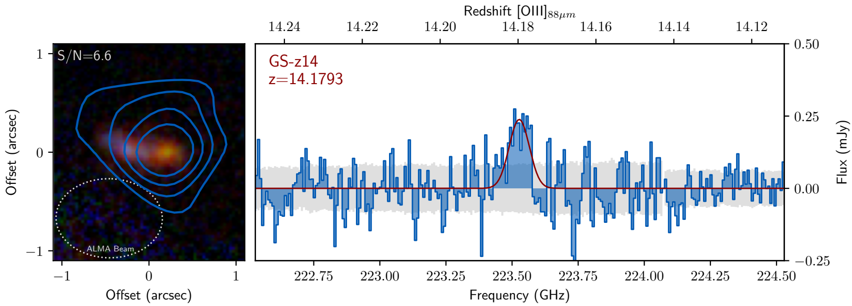

Figure 4.2. Detection of [OIII]$_{88\mu m}$ in GS-z14 at $z = 14.1793 \pm 0.0007$. *Left Panel:* Contours showing the [OIII]$_{88\mu m}$ emission (2, 3, 4 and 5σ) overlaid on an RGB image based on F150W, F200W and F444W imaging (Eisenstein et al. 2023a,b). The object with a bluer colour to the left of GS-z14 is a z=3.475 foreground galaxy (Carniani et al. 2020). The [OIII]$_{88\mu m}$ emission is detected at a peak significance of 6.6σ in the collapsed data-cube and well centered on GS-z14. *Right Panel:* The spectrum of the [OIII]$_{88\mu m}$ line (*blue bars*) extracted from the >3σ emission region in the moment-0 map. The red line shows the Gaussian fit used to measure the spectroscopic redshift and FWHM of the line. The grey shaded region indicates the 1σ uncertainties.

collapses moment maps over a range of 75 to 350 km s^{-1} in steps of 1 channel (~10 km s^{-1}). For each moment map, we identify the significant (>3σ) peaks and add the results to a large list of features. This list is then pruned by removing duplicates within 2×FWHM and 1.5× the beamsize. We also perform the search on the negative moment map, which is useful to characterize the noise properties. In Figure 4.1, we show a blind extraction of the ALMA spectrum at the location of GS-z14 using a 0.5" aperture.

The most significant line candidate we extract within a 0.5" radius of the JWST position of GS-z14 is detected with a peak significance of 6.6σ and separation of 0.12". The candidate line is consistent with being spatially coincident with GS-z14 in the JWST/NIRCam observations given expected 0.18" positional uncertainties following from a 6.6σ line detection and 1.08" beam.[1]

[1] https://help.almascience.org/kb/articles/what-is-the-absolute-astrometric-accuracy-of-alma

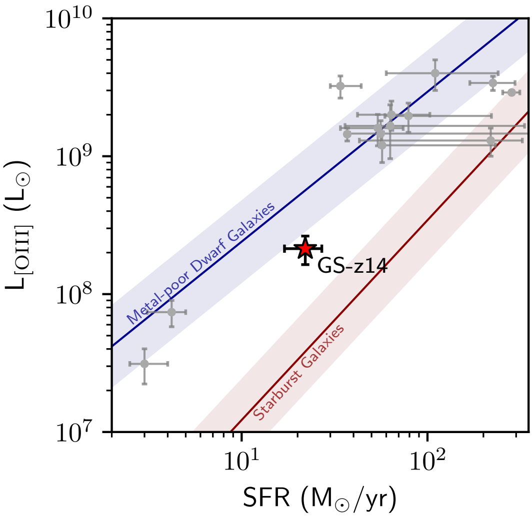

Figure 4.3. The luminosity of $[OIII]_{88\mu m}$ in GS-z14 is consistent with the local relation for metal-poor dwarf galaxies found by De Looze et al. (2014). For context we also show the local relation for starburst galaxies (De Looze et al. 2014) as well as a compilation of $z > 6.5$ galaxies (Bakx et al. 2020; Carniani et al. 2020; Harikane et al. 2020; Akins et al. 2022; Witstok et al. 2022; Algera et al. 2024; Fujimoto et al. 2024). Even as early as $z = 14.1793 \pm 0.0007$ and for high redshift galaxies in general, the relation for metal-poor dwarf galaxies seems to be a good fit (at SFR $\lesssim 100\, M_\odot\, \mathrm{yr}^{-1}$).

4.3 RESULTS

4.3.1 *$[OIII]_{88\mu m}$ in GS-z14*

We have identified an emission line with a signal-to-noise of 6.6σ within $0.12''$ of GS-z14 at 223.528±0.009 GHz. This corresponds to $[OIII]_{88\mu m}$ at $z = 14.1793 \pm 0.0007$, consistent with both the redshift derived from the Lyman break observed by JWST and also the tentative 3.6σ detection of $CIII]_{1907,1909}$ at 2.89μm (Carniani et al. 2024). In particular, the consistency of our new redshift determination from $[OIII]_{88\mu m}$ with the earlier redshift estimate $z = 14.178 \pm 0.003$ from the tentative $CIII]_{1907,1909}$ doublet (Carniani et al. 2024) greatly increases our confidence in the robust-

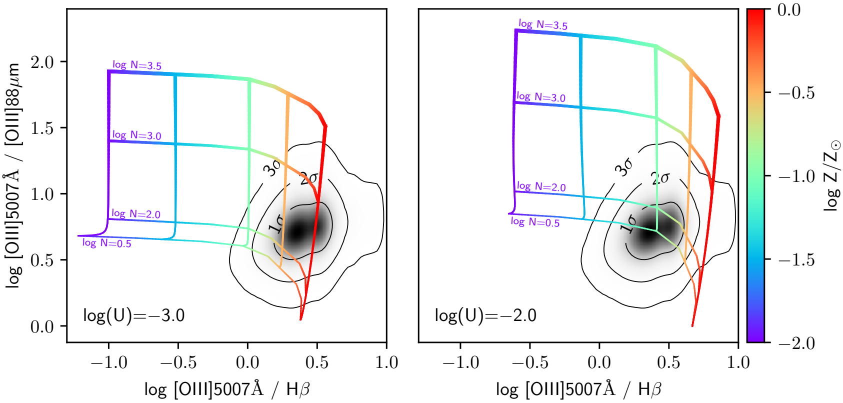

Figure 4.4. The ALMA and MIRI observations constrain the emission line ratios of GS-z14 to the dark shaded region in the figure highlighted by the 1 and 2σ contours. ISM modeling as shown by the coloured grid highlights the dependence on metallicity and density. This indicates that GS-z14 is consistent with a relatively high metallicity ($Z>0.1\ Z_\odot$) and moderate to low density $\log(N) < 3.0\mathrm{cm}^{-3}$. There is a further minor dependence on the ionization parameter that shifts and deforms the grid, but does not impact the conclusions. For context, SED fitting of GS-z14 finds $\log(U) = -2.5 \pm 0.5$ (Helton et al. 2024).

ness of the current redshift determination given the availability of multiple line detections. We show the contours of the $[\mathrm{OIII}]_{88\mu m}$ emission overlaid on an RGB image based on F150W, F200W and F400W imaging and a S/N-optimized extraction of the spectrum in Figure 4.2.

We measure the integrated line flux using the moment-zero map of the emission line, including all channels that fall within 2× the FWHM of the line. The FWHM is determined in an iterative process; starting from an estimate of the FWHM we collapse a moment-zero map and extract a 1d spectrum, which is extracted by including all pixels with $S/N>3\sigma$ on the moment-zero map. A new FWHM is then measured using this 1d spectrum by fitting a Gaussian. This new FWHM is then used to collapse a new moment-zero map for the next iteration. A stable FWHM is achieved in less than 10 steps (Schouws et al. 2022).

The final FWHM we measure is 136±31 km s^{-1}. Assuming that GS-z14 is dispersion-dominated and $r_{[\mathrm{OIII}]} = r_e = 260$ pc, this implies a dynamical mass of $(1.0\pm0.5)\times10^9\ M_\odot(\sin i)^2$. At the current resolution we do not see evidence for a velocity gradient.

We measure an integrated flux of 39±10 mJy·km s^{-1} this corresponds to a [OIII]$_{88\mu m}$ luminosity of $(2.1 \pm 0.5) \times 10^8\,\mathrm{L}_\odot$ (Solomon et al. 1992) (after correction for lensing magnification; Carniani et al. 2024). This places GS-z14 a factor of $\sim 2\times$ below the local relation between $\mathrm{L}_{[\mathrm{OIII}]}$ and SFR for metal-poor dwarf galaxies from De Looze et al. (2014), albeit nearly within the scatter (Figure 4.3). The general consistency with the $z = 0$ relation for a galaxy a mere ~ 300 Myr after the Big Bang suggests that GS-z14 has undergone rapid evolution, as discussed in detail in Section 4.4.1.

4.3.2 *Dust Continuum*

We do not detect the dust continuum from GS-z14, with a formal 90μm continuum limit of $< 15.1\,\mu$Jy beam^{-1} (3σ). We provide an upper limit on its dust mass assuming an optically thin modified black body with a dust temperature of $T_\mathrm{d} = 60\,\mathrm{K}$ and $\beta_\mathrm{IR} = 2.03$ for the dust SED. The assumed temperature is consistent with extrapolations from theoretical models (e.g., Liang et al. 2019; Sommovigo et al. 2022a) and observational trends (e.g., Schreiber et al. 2018; Faisst et al. 2020; Sommovigo et al. 2021, 2022a,b; Witstok et al. 2023a) to $z \approx 14$. We note that the precise evolution of dust temperature is still uncertain and debated (e.g. Sommovigo et al. 2022b). However, our assumption of a relatively high dust temperature is also supported by the inverse correlation between metallically and dust temperature noted by Sommovigo et al. (2022b) and increasing temperature of the CMB background at high redshift[2].

We follow Ferrara et al. (2024) by adopting the Weingartner & Draine (2001) dust model with $\kappa_{88} = 34.15\,\mathrm{cm}^{-2}\,\mathrm{g}^{-1}$ at rest-frame 88 μm. This yields a (lensing-corrected) upper limit on the dust mass and infrared luminosity (integrated across $8 - 1000\,\mu$m) of $\log(M_\mathrm{d}/M_\odot) < 6.0$ and $\log(L_\mathrm{IR}/L_\odot) < 11.1$, respectively. The latter corresponds to an obscured SFR of $\mathrm{SFR_{IR}} < 14\,M_\odot\,\mathrm{yr}^{-1}$ which, combined with the unobscured SFR of GS-z14 inferred by Carniani et al. (2024), implies an obscured fraction of $f_\mathrm{obs} < 0.66$. Finally, using the stellar mass of GS-z14 inferred by Helton et al. (2024), we infer a dust-to-stellar mass ratio $\xi_d \equiv M_\mathrm{d}/M_\star < 1.9\times10^{-3}$.

The above estimates require the assumption of a dust temperature. Assuming a lower temperature of $T_\mathrm{d} = 45\,\mathrm{K}$, which would imply no significant evolution of the dust temperature from $z \sim 4$ (e.g. Faisst et al. 2020), results in a dust mass of $\log(M_\mathrm{d}/M_\odot) < 6.8$. Meanwhile, a significantly

[2] For context, the CMB background at $z = 14.2$ has a temperature of $T_\mathrm{CMB} = 41.4\mathrm{K}$.

higher temperature temperature of $T_\mathrm{d} = 100\,\mathrm{K}$ would result in a dust mass of $\log(M_\mathrm{d}/M_\odot) < 5.3$. In Section 4.4.2, we discuss this in further detail, focusing on the Attenuation Free Model by Ferrara et al. (2024) which self-consistently predicts a dust temperature for GS-z14 based on the observed V-band attenuation and the spatial extent of the dust.

4.4 DISCUSSION

4.4.1 *Constraints on the ISM of GS-z14*

Luminosity ratios of emission lines are invaluable diagnostic tools to probe the conditions of the ISM in galaxies. Although the NIRSpec spectroscopy of GS-z14 does not show significant emission lines, its detection in the MIRI F770W band places a constraint on the combined [OIII]$\lambda\lambda$4959,5007Å+Hβ flux. Following Helton et al. (2024) we assume that the flux excess in F770W is 27.5±5.6 nJy based on a flat underlying continuum emission.

The [OIII]λ5007Å luminosity (hereafter [OIII]) can subsequently be calculated based on an assumed [OIII]/Hβ ratio and be compared to the luminosity of OIII as measured by ALMA. We repeat this calculation $10^6\times$, drawing random [OIII]/Hβ ratios from probability distribution from the SED fitting by Helton et al. (2024), where we combine the probability distributions from the three star formation history assumptions. This distribution has a median ratio of $2.5^{+0.9}_{-0.6}$. As noted by Helton et al. (2024), this is lower than the median [OIII]/Hβ at $z \sim 8.0$ which is $6.0^{+2.4}_{-2.9}$ in JADES (Helton et al. 2024), 6.4±0.9 in FRESCO (Meyer et al. 2024) and $7.2^{+2.6}_{-2.4}$ in PRIMAL (Heintz, K. E. et al. 2025).

In this process we also account for the uncertainty in the line luminosities from ALMA and JWST by drawing random values from a Gaussian error distribution.

The resulting constraints on the [OIII]/[OIII]$_{88\mu m}$ versus [OIII]/Hβ line ratios are shown in Figure 4.4. For context we show a grid of ISM models for a large range of conditions based on Cloudy models (Ferland et al. 2017). The models consist of an HII region that smoothly transitions to a Photo Dissociation Region (PDR) until a fixed optical depth (A_V=10) in a plane parallel geometry. For more details on the model we refer to Witstok et al. (2022). We note that the ionization parameter of GS-z14 has been loosely constrained by Helton et al. (2024) to be $\log(U_\mathrm{ion}) = -2.5 \pm 0.5$, and we therefore show two sets of Cloudy models bracketing this range, at a fixed $\log(U_\mathrm{ion}) \in (-3.0, -2.0)$. We focus on the grid with an ionization parameter $\log(U_{\rm ion}) = -2$, as Kohandel et al. (2023) predict the most $[\rm OIII]_{88\mu m}$-luminous galaxies at $z \gtrsim 10$ have high ionization parameters. Moreover, if the assumed [OIII]/Hβ is underestimated, the observed line ratios can only be reproduced by higher values of the ionization parameter.

While the uncertainties are substantial, given the existence of only a photometric detection of the [OIII]$\lambda\lambda$4959,5007Å line, the Witstok et al. (2022) models suggest a relatively high metallicity of $Z \sim 0.1\,Z_\odot$, in combination with a moderate-to-low electron density ($\log N \lesssim 10^{2.5}$). This is on the low end of, albeit still consistent with, the distribution of electron densities found for $z \gtrsim 5$ galaxies, which typically show values of $\log(N) \sim 2-3$ (e.g., Isobe et al. 2023). However, for more accurate constraints on the ISM conditions of GS-z14, direct spectroscopic detections of additional oxygen lines are crucial, for example through MIRI spectroscopy.

Intriguingly, the detection of $[\rm OIII]_{88\mu m}$ at $z = 14.1793 \pm 0.0007$ is consistent within 1σ with the tentative detection of CIII]$\lambda\lambda$1907,9Å reported by Carniani et al. (2024) at $z = 14.178 \pm 0.013$. Carniani et al. (2024) derive a CIII]$\lambda\lambda$1907,9Å rest-frame equivalent width ($\rm EW_0$) of 8.0±2.3 Å, which is relatively high compared to the $\rm EW_0$([OIII]+Hβ) of 370^{+360}_{-130} Å estimated by Helton et al. (2024), albeit consistent with the distribution found for galaxies at $z \sim 0-4$ (e.g. Maseda et al. 2017; Ravindranath et al. 2020; Tang et al. 2021), see Figure 4.5. The measured equivalent widths are in agreement with predictions from Cloudy at a metallicity of $Z \sim 0.05 - 0.2\,Z_\odot$, and with an ionization parameter of $\log(U) \sim -2.5$, in agreement with Helton et al. (2024).

Moreover, Jones et al. (2020) derive a calibration for the oxygen abundance using the $[\rm OIII]_{88\mu m}$ line and star-formation rate. Using their calibration we derive $12 + \log \rm O^{++}/H^{+}$=$7.66^{+0.19}_{-0.21}$ (∼6-14% solar metallicity, using the solar abundance from Asplund et al. (2009)). In Figure 4.6 we use a Cloudy grid with a 1Myr old input stellar population to estimate the $[\rm OIII]_{88\mu m}$/SFR ratio as a function of ionisation parameter, for models with different metallicity and gas density. For modest gas density the measurements are consistent with 10% solar oxygen abundance, however, higher gas densities or older ages for the input stellar population will give higher metallicity estimates (up to solar metallicity).

The detection of both carbon and oxygen lines thus reinforce the notion that GS-z14 is already moderately chemically enriched. Adopting a fiducial $Z \sim 0.05 - 0.2\,Z_\odot$ in combination with the stellar mass from Helton et al. (2024), GS-z14 falls onto the high-redshift mass-metallicity relation, which has been mapped out to $z \sim 10$, and appears to show only mild evolution beyond $z \gtrsim 3$ (e.g., Curti et al. 2024).

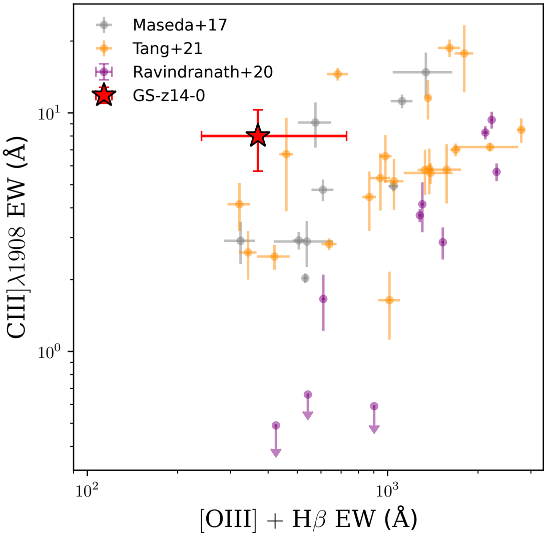

Figure 4.5. The rest-frame equivalent width of CIII]$\lambda\lambda$1907,9Å as a function of EW_0([OIII]+Hβ) (Carniani et al. 2024; Helton et al. 2024). GS-z14-0 is broadly consistent with measurements from the literature at $z = 1-3$ (grey, purple and orange points; Maseda et al. 2017; Ravindranath et al. 2020; Tang et al. 2021).

4.4.2 *Constraints on Dust Formation Processes*

The build-up of dust in galaxies is a complex process involving multiple mechanisms of dust production and destruction, operating on different timescales. Supernova explosions (SNe) produce dust quickly, on timescales similar to the lifecycle of massive stars (~10 Myr), whilst Asymptotic Giant Branch (AGB) stars contribute to dust production on significantly longer timescales (~300 Myr, Schneider & Maiolino 2024). The contribution from grain growth in the ISM depends on the physical conditions, but is expected to be sub-dominant at extremely high redshifts and low gas-phase metallicities (Ferrara et al. 2016; Dayal et al. 2022; Witstok et al. 2023a; Markov et al. 2024).

At lower redshifts it is difficult to disentangle the impact of different contributions (e.g., De Looze et al. 2020; Galliano et al. 2021), but GS-z14 has formed sufficiently early in cosmic history that dust production

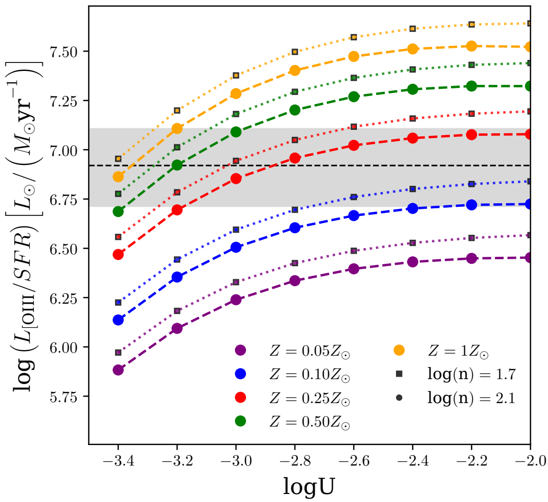

Figure 4.6. CLOUDY modelling of the $[\mathrm{OIII}]_{88\mu m}$ /SFR as a function of ionisation parameter for a range of metallicities and densities ∼50-100 cm^{-3}. Our model gives a lower limit on the metallicity of ∼10% $Z_\odot$, with higher gas densities and older ages preferring higher metallicity estimates.

through SNe is likely the dominant formation process. This makes GS-z14 an ideal test-bed for dust formation models in the early universe.

The efficiency of dust production from SNe can be inferred by measuring the dust-to-stellar mass ratio (ξ_d). This parameter is hard to interpret as it depends on both the expected number of SNe per unit of formed stellar mass (ν), which in turn depends on the assumed Initial Mass Function (IMF), and on the net dust yield per SN event (y_d), $\xi_d = y_d \times \nu$. In local SN remnants y_d values varying in the wide range from 0.01 to 1.1 $\mathrm{M}_\odot$ have been directly measured (Milisavljevic et al. 2024). Such values are broadly in agreement with most indirect high-z measurements based on dust-to-stellar mass ratios (Sommovigo et al. 2022a,b).

Utilizing the continuum non-detection of GS-z14, we can attempt to place an upper limit on y_d. Following Michałowski (2015) and adopting a Salpeter IMF, the limit of $\xi_d < 2 \times 10^{-3}$ suggests a yield of $y_d < 0.24\,M_\odot$/SN. This is consistent with a commonly adopted yield of $y_d \sim 0.1\,M_\odot$/SN (e.g., Sommovigo et al. 2022a; Dayal et al. 2022). If we rely on such a value for $y_d \sim 0.1\,M_\odot$/SN and assume that dust follows a similar spatial distribution as the stellar component, GS-z14 should be

Table 4.1. Properties of GS-z14

Parameter	Value
RA	03:32:19.9049
Dec	−27:51:20.265
Redshift	$z = 14.1793(7)$
M_{UV}	-20.81 ± 0.16
Stellar Mass ($\log(M_\odot)$)	$8.7^{+0.5}_{-0.4}$
Star Formation Rate ($M_\odot$/yr)	25^{+6}_{-5}
$[OIII]_{88\mu m}$ Luminosity (10^8 $L_\odot$)	2.1±0.5
FWHM $[OIII]_{88\mu m}$ (km s^{-1})	136±31
Dynamical Mass ($M_\odot$ $(\sin i)^2$)	$(1.0\pm0.5)\times10^9$
90-μm continuum flux (μJy/beam)	< 15.1 (3σ)
Dust Mass ($\log(M_\odot)$)	< 6.0

Notes: $M_{\rm UV}$ from Carniani et al. (2024); stellar mass and SFR from Helton et al. (2024). Values have been corrected for a lensing magnification of 1.17× (Carniani et al. 2024).

largely obscured (A_V~9.5, see also Ferrara et al. 2024) and would not have been detected with JWST. However, the JWST data only reveal a relatively low visual extinction of A_V=0.31, implying a much (1 dex) lower dust mass of 5×10^4 $M_\odot$ with $\xi_d < 10^{-4}$ and $y_d < 0.015\,M_\odot$/SN (Ferrara et al. 2024).

Clearly, SNe (and later on growth in the ISM) do produce tangible amounts of dust, as less than 500 Myr later, at $z \approx 7$, dust appears widespread (Inami et al. 2022; Schouws et al. 2023; Witstok et al. 2023a; Algera et al. 2023) – both puzzlingly high dust-to-stellar mass ratios ($M_{\rm d}/M_\star \sim 0.01$; Algera et al. 2024) and fully dust-obscured sources (Fudamoto et al. 2021) are observed at this epoch. In addition, features of the attenuation curve associated with the carbonaceous dust grains produced by SNe are observed at $z \sim 6.7$ (Witstok et al. 2023b).

The discrepancy between what is observed by JWST versus what is expected based on dust production from past SNe can be resolved by assuming that the majority of the dust has been removed from star-forming regions by radiation pressure-driven outflows. Such a scenario had been suggested in the Attenuation Free Model (AFM) presented in Ferrara et al. (2024).

In their fiducial model, Ferrara et al. (2024) suggest the dust in GS-z14 to have a typical extent of 1.4 kpc, as a more compact size would be inconsistent with the visual extinction measured by JWST. We note that, given the resolution of our data, dust of this extent would not be resolved across multiple ALMA beams. Combined with a fiducial yield of $0.1\,M_{\odot}$/SN, the AFM predicts a continuum flux density for GS-z14 of $F_{88} = 14.9\,\mu$Jy. This is just below the sensitivity limit of our observations, which yield an upper limit of $F_{88} < 15.1\,\mu$Jy beam^{-1}. However, if the assumed dust yield is 0.5 dex lower ($0.1\,M_{\odot}$/SN), then the expected flux density would be $F_{88} \sim 8\,\mu$Jy, well below the current limit. As such, a conclusive investigation of the dust content of GS-z14, as well as further testing of the AFM model predictions, requires deeper and high-resolution ALMA continuum observations.

4.5 SUMMARY

We report the robust detection of a 6.6σ $[\mathrm{OIII}]_{88\mu m}$ line of JADES-GS-z14-0 at 223.528±0.009 GHz, providing us with a precise spectroscopic redshift measurement of $z = 14.1793 \pm 0.0007$. This represents a substantial jump in redshift over the previous high-redshift $[\mathrm{OIII}]_{88\mu m}$-detection from MACS1149-JD1 at $z = 9.1096$ (Hashimoto et al. 2018). The $[\mathrm{OIII}]_{88\mu m}$ line was identified using data from an ALMA Cycle-10 DDT program (2023.A.00037.S, PI: Schouws) providing a spectral scan from 218.70 to 229.45 GHz (10.75 GHz baseline), covering the redshift range z=13.79 to 14.51. The precision of the current redshift measurement represents $\gtrsim 180\times$ gain over the prior redshift measurement of $z = 14.32^{+0.08}_{-0.20}$ from NIRSpec.

The redshift we find for the source is consistent with the redshift Carniani et al. (2024) derive ($z = 14.178 \pm 0.013$) based on their tentative 3.6σ detection of $\mathrm{CIII]}_{1907,1909}$ doublet at 2.89μm, providing strong evidence the earlier line detection is real. As such, we now have multiple line detections of GS-z14-0, $\mathrm{CIII]}_{1907,1909}$ (3.6σ) with JWST and $[\mathrm{OIII}]_{88\mu m}$ (6.6σ) with ALMA, providing rather definitive evidence for the robustness of the redshift determination of GS-z14-0. Of note, the detection of $[\mathrm{OIII}]_{88\mu m}$ with ALMA was achieved with less integration time (2.8 hours) than was required for the 3.6σ tentative detection of $\mathrm{CIII]}_{1907,1909}$ with JWST (9.3 hours), providing a rather dramatic illustration of the discovery potential of ALMA.

We find no detection of the dust continuum from JADES-GS-z14-0 based on the DDT observations, with a $< 3\sigma$ upper limit of $<15.1\,\mu$Jy beam^{-1}.

This suggests a low dust-to-stellar mass ratio of $M_{\rm d}/M_{\star} < 1.9 \times 10^{-3}$, consistent with supernova dust production yields $y_d < 0.24\,M_{\odot}$/SN.

Combining a previous JWST/MIRI photometric measurement of the [OIII]$\lambda\lambda$4959,5007Å and Hβ lines with CLOUDY models, we find GS-z14 to be surprisingly metal-enriched ($Z \sim$ 0.05-0.2 $Z_{\odot}$) a mere 300 Myr after the Big Bang, with moderate to low density $\log(N) < 3.0\,{\rm cm}^{-3}$.

Thanks to the precise spectroscopic redshift measurement and $[{\rm OIII}]_{88\mu m}$ line detection we now have for GS-14-0 using just 2.8 hours, it is clear that additional follow-up of GS-z14-0 with ALMA would be highly fruitful and should include (1) higher spatial resolution observations of $[{\rm OIII}]_{88\mu m}$ to improve constraints on dynamical masses and state of GS-z14-0 and deeper constraints on the dust continuum, (2) observations of the $[{\rm CII}]_{158\mu m}$ line in band 4, lying just 0.2 GHz above the low-frequency boundary, to better probe the ionization parameter U and build-up of metals, and (3) JWST/MIRI observations of [OIII]$\lambda\lambda$4959,5007Å and Hβ to place tighter constraints on the electron density and metallicity of GS-z14-0.

ACKNOWLEDGMENTS

This paper makes use of the following ALMA data: ADS/JAO.ALMA 2023.A.00037.S. ALMA is a partnership of ESO (representing its member states), NSF (USA) and NINS (Japan), together with NRC (Canada), MOST and ASIAA (Taiwan), and KASI (Republic of Korea), in cooperation with the Republic of Chile. The Joint ALMA Observatory is operated by ESO, AUI/NRAO and NAOJ. We are greatly appreciative to our ALMA program coordinator Violette Impellizzeri for support with our ALMA program and Allegro, the European ALMA Regional Center node in the Netherlands. We are grateful to J. Witstok for providing the CLOUDY models from Witstok et al. (2022) for the analysis conducted in this paper. We thank M. Kohandel and A. Pallottini for simulated data analysis. This work was supported by NAOJ ALMA Scientific Research Grant Code 2021-19A (HA). AF acknowledges support from the ERC Advanced Grant INTERSTELLAR H2020/740120 and support from the grant NSF PHY-2309135 to the Kavli Institute for Theoretical Physics (KITP). MS acknowledges support from the European Research Commission Consolidator Grant 101088789 (SFEER), from the CIDEGENT/2021/059 grant by Generalitat Valenciana, and from project PID2023-149420NB-I00 funded by MICIU/AEI/10.13039/501100011033 and by ERDF/EU.

REFERENCES

Akins, H. B., Fujimoto, S., Finlator, K., et al. 2022, ApJ, 934, 64,

Algera, H. S. B., Inami, H., Oesch, P. A., et al. 2023, MNRAS, 518, 6142,

Algera, H. S. B., Inami, H., Sommovigo, L., et al. 2024, MNRAS, 527, 6867,

ALMA Technical Handbook. 2024, ALMA Cycle 10 Technical Handbook, ALMA Observatory

Arata, S., Yajima, H., Nagamine, K., Abe, M., & Khochfar, S. 2020, MNRAS, 498, 5541,

Asplund, M., Grevesse, N., Sauval, A. J., & Scott, P. 2009, ARA&A, 47, 481,

Bakx, T. J. L. C., Tamura, Y., Hashimoto, T., et al. 2020, MNRAS, 493, 4294,

Bakx, T. J. L. C., Zavala, J. A., Mitsuhashi, I., et al. 2023, MNRAS, 519, 5076,

Béthermin, M., Fudamoto, Y., Ginolfi, M., et al. 2020, A&A, 643, A2,

Bouwens, R., Illingworth, G., Oesch, P., et al. 2023, MNRAS, 523, 1009,

Bouwens, R. J., Smit, R., Schouws, S., et al. 2022, ApJ, 931, 160,

Bunker, A. J., Saxena, A., Cameron, A. J., et al. 2023, Astronomy & Astrophysics, 677, A88,

Bunker, A. J., Saxena, A., Cameron, A. J., et al. 2023, A&A, 677, A88,

Carniani, S., Ferrara, A., Maiolino, R., et al. 2020, MNRAS, 499, 5136,

Carniani, S., Hainline, K., D'Eugenio, F., et al. 2024, Nature, 633, 318,

Castellano, M., Fontana, A., Treu, T., et al. 2022, ApJL, 938, L15,

Castellano, M., Napolitano, L., Fontana, A., et al. 2024, ApJ, 972, 143,

Chabrier, G. 2003, PASP, 115, 763,

Cormier, D., Madden, S. C., Lebouteiller, V., et al. 2015, A&A, 578, A53,

Curti, M., Maiolino, R., Curtis-Lake, E., et al. 2024, A&A, 684, A75,

Curtis-Lake, E., Carniani, S., Cameron, A., et al. 2023, Nature Astronomy, 7, 622,

Dayal, P., Ferrara, A., Sommovigo, L., et al. 2022, Monthly Notices of the Royal Astronomical Society, 512, 989–1002,

Dayal, P., Ferrara, A., Sommovigo, L., et al. 2022, MNRAS, 512, 989,

De Looze, I., Cormier, D., Lebouteiller, V., et al. 2014, A&A, 568, A62,

De Looze, I., Lamperti, I., Saintonge, A., et al. 2020, MNRAS, 496, 3668,

Donnan, C. T., McLeod, D. J., Dunlop, J. S., et al. 2022, Monthly Notices of the Royal Astronomical Society, 518, 6011–6040,

Eisenstein, D. J., Willott, C., Alberts, S., et al. 2023a, arXiv e-prints, arXiv:2306.02465,

Eisenstein, D. J., Johnson, B. D., Robertson, B., et al. 2023b, arXiv e-prints, arXiv:2310.12340,

Faisst, A. L., Fudamoto, Y., Oesch, P. A., et al. 2020, Monthly Notices of the Royal Astronomical Society, 498, 4192, Faisst, A. L., Schaerer, D., Lemaux, B. C., et al. 2020, ApJS, 247, 61,

Ferland, G. J., Chatzikos, M., Guzmán, F., et al. 2017, RMxAA, 53, 385.

Ferrara, A. 2024, A&A, 689, A310,

Ferrara, A., Carniani, S., di Mascia, F., et al. 2024.

Ferrara, A., Viti, S., & Ceccarelli, C. 2016, MNRAS, 463, L112,

Finkelstein, S. L., Leung, G. C. K., Bagley, M. B., et al. 2024, ApJL, 969, L2,

Fudamoto, Y., Oesch, P. A., Schouws, S., et al. 2021, Nature, 597, 489,

Fujimoto, S., Finkelstein, S. L., Burgarella, D., et al. 2023, ApJ, 955, 130,

Fujimoto, S., Ouchi, M., Nakajima, K., et al. 2024, ApJ, 964, 146,

Furlanetto, S. R., & Mirocha, J. 2023, Monthly Notices of the Royal Astronomical Society, 523, 5274–5279,

Galliano, F., Nersesian, A., Bianchi, S., et al. 2021, A&A, 649, A18,

Genzel, R., Tacconi, L. J., Gracia-Carpio, J., et al. 2010, Monthly Notices of the Royal Astronomical Society, 407, 2091–2108,

Hainline, K. N., Johnson, B. D., Robertson, B., et al. 2024, ApJ, 964, 71,

Harikane, Y., Ouchi, M., Inoue, A. K., et al. 2020, ApJ, 896, 93,

Harikane, Y., Ouchi, M., Oguri, M., et al. 2023, ApJS, 265, 5,

Harikane, Y., Ouchi, M., Oguri, M., et al. 2023, The Astrophysical Journal Supplement Series, 265, 5,

Harikane, Y., Inoue, A. K., Ellis, R. S., et al. 2024, arXiv e-prints, arXiv:2406.18352,

Hashimoto, T., Laporte, N., Mawatari, K., et al. 2018, Nature, 557, 392,

Heintz, K. E., Brammer, G. B., Watson, D., et al. 2025, AA, 693, A60,

Helton, J. M., Rieke, G. H., Alberts, S., et al. 2024.

Hunter, T. R., Indebetouw, R., Brogan, C. L., et al. 2023, Publications of the Astronomical Society of the Pacific, 135, 074501,

Inami, H., Algera, H. S. B., Schouws, S., et al. 2022, MNRAS, 515, 3126,

Isobe, Y., Ouchi, M., Nakajima, K., et al. 2023, ApJ, 956, 139,

Jones, T., Sanders, R., Roberts-Borsani, G., et al. 2020, ApJ, 903, 150,

Kaasinen, M., van Marrewijk, J., Popping, G., et al. 2023, A&A, 671, A29,

Katz, H., Kimm, T., Sijacki, D., & Haehnelt, M. G. 2017, MNRAS, 468, 4831,

Katz, H., Galligan, T. P., Kimm, T., et al. 2019, Monthly Notices of the Royal Astronomical Society, 487, 5902–5921,

Katz, H., Rosdahl, J., Kimm, T., et al. 2022, MNRAS, 510, 5603,

Kepley, A. A., Tsutsumi, T., Brogan, C. L., et al. 2020, PASP, 132, 024505,

Kohandel, M., Ferrara, A., Pallottini, A., et al. 2023, MNRAS, 520, L16,

Le Fèvre, O., Béthermin, M., Faisst, A., et al. 2020, A&A, 643, A1,

Liang, L., Feldmann, R., Kereš, D., et al. 2019, MNRAS, 489, 1397, Markov, V., Gallerani, S., Ferrara, A., et al. 2024, arXiv e-prints, arXiv:2402.05996,

Maseda, M. V., Brinchmann, J., Franx, M., et al. 2017, A&A, 608, A4,

Meyer, R. A., Oesch, P. A., Giovinazzo, E., et al. 2024, Monthly Notices of the Royal Astronomical Society, 535, 1067,

Michałowski, M. J. 2015, A&A, 577, A80,

Milisavljevic, D., Temim, T., Looze, I. D., et al. 2024, The Astrophysical Journal Letters, 965, L27,

Moriwaki, K., Yoshida, N., Shimizu, I., et al. 2018, Monthly Notices of the Royal Astronomical Society: Letters, 481, L84–L88,

Naidu, R. P., Oesch, P. A., van Dokkum, P., et al. 2022, ApJL, 940, L14,

Nakazato, Y., Yoshida, N., & Ceverino, D. 2023, ApJ, 953, 140,

Oesch, P. A., Brammer, G., Dokkum, P. G. v., et al. 2016, The Astrophysical Journal, 819, 129,

Oesch, P. A., Brammer, G., Naidu, R. P., et al. 2023, MNRAS, 525, 2864,

Oke, J. B., & Gunn, J. E. 1983, ApJ, 266, 713,

Pallottini, A., Ferrara, A., Gallerani, S., et al. 2022, MNRAS, 513, 5621,

Popping, G. 2023, Astronomy & Astrophysics, 669, L8,

Ravindranath, S., Monroe, T., Jaskot, A., Ferguson, H. C., & Tumlinson, J. 2020, The Astrophysical Journal, 896, 170,

Robertson, B. E., Tacchella, S., Johnson, B. D., et al. 2023, Nature Astronomy, 7, 611–621,

Santini, P., Fontana, A., Castellano, M., et al. 2023, The Astrophysical Journal Letters, 942, L27,

Schneider, R., & Maiolino, R. 2024, A&A Rv, 32, 2,

Schouws, S., Stefanon, M., Bouwens, R., et al. 2022, ApJ, 928, 31,

Schouws, S., Bouwens, R., Smit, R., et al. 2023, ApJ, 954, 103,

Schreiber, C., Elbaz, D., Pannella, M., et al. 2018, A&A, 609, A30,

Solomon, P. M., Downes, D., & Radford, S. J. E. 1992, ApJL, 387, L55,

Sommovigo, L., Ferrara, A., Carniani, S., et al. 2021, MNRAS, 503, 4878,

Sommovigo, L., Ferrara, A., Pallottini, A., et al. 2022a, MNRAS, 513, 3122,

Sommovigo, L., Ferrara, A., Carniani, S., et al. 2022b, MNRAS, 517, 5930,

Tang, M., Stark, D. P., Chevallard, J., et al. 2021, MNRAS, 501, 3238,

Thompson, A. R., Moran, J. M., & Swenson, George W., J. 2017, Interferometry and Synthesis in Radio Astronomy, 3rd Edition,

Treu, T., Calabrò, A., Castellano, M., et al. 2023, The Astrophysical Journal Letters, 942, L28,

Vallini, L., Ferrara, A., Pallottini, A., Carniani, S., & Gallerani, S. 2021, MNRAS, 505, 5543,

Vallini, L., Witstok, J., Sommovigo, L., et al. 2024, MNRAS, 527, 10,

Weingartner, J. C., & Draine, B. T. 2001, ApJ, 548, 296, Williams, C. C., Alberts, S., Ji, Z., et al. 2024, ApJ, 968, 34,

Witstok, J., Jones, G. C., Maiolino, R., Smit, R., & Schneider, R. 2023a, MNRAS, 523, 3119,

Witstok, J., Smit, R., Maiolino, R., et al. 2022, MNRAS, 515, 1751,

Witstok, J., Shivaei, I., Smit, R., et al. 2023b, Nature, 621, 267,

Yang, S., & Lidz, A. 2020, Monthly Notices of the Royal Astronomical Society, 499, 3417–3433,

Yoon, I., Carilli, C. L., Fujimoto, S., et al. 2023, The Astrophysical Journal, 950, 61,

Zavala, J. A., Castellano, M., Akins, H. B., et al. 2024, arXiv e-prints, arXiv:2403.10491,

Chapter 5

Deep Constraints on [CII]$_{158\mu m}$ in JADES-GS-z14-0: Further Evidence for a Galaxy with Low Gas Content at z=14.2

We present deep ALMA observations targeting the [CII]$_{158\mu m}$ line in JADES-GS-z14-0, the most distant known galaxy at z=14.1793. We do not detect the [CII]$_{158\mu m}$ line in our deep observations, implying a luminosity of $<6\times10^7$ $L_\odot$ (3σ) for the target. Comparing this with the detected [OIII]$_{88\mu m}$ line, we constrain the [OIII]/[CII] ratio to be >3.5, significantly improving our probe of the ionization parameter U. The observed ratio is higher than analogues in the local universe, but consistent with galaxies at $z \approx$ 6-9. Through ISM modeling, we infer extreme ionizing conditions with log(U)> -2.0, likely requiring a young stellar population. Our modeling also indicates a relatively low gas density (51^{+116}_{-32} cm^{-3}), significantly lower than expected from lower redshift trends. We infer a relatively high gas-phase metallicity (16±6% solar) consistent with previous results and implying a rapid build-up of metals. Finally, using [CII] as a molecular/cold gas mass tracer, we infer a low gas fraction ($f_{\rm gas,mol} < 0.77$), consistent with previous estimates of the dynamical mass from [OIII]$_{88\mu m}$. Combined with the low observed gas density, lack of dust and high ionization parameter, this suggests strong feedback processes are playing an important role in the evolution of this galaxy. Our observations show that JADES-GS-z14-0 is a rapidly evolving galaxy with extreme ISM conditions, shedding light on the earliest phases of galaxy formation.

Schouws, Bouwens, Algera, Smit, Kumari, Rowland,
van Leeuwen, Sommovigo, Ferrara, Oesch, Ormerod, Stefanon,
Herard-Demanche, Hodge, Fudamoto, Röttgering, and van der Werf
arXiv:2502.01610 (2025)

5.1 INTRODUCTION

The discovery and spectroscopic confirmation of galaxies at $z > 10$ has recently become possible due to the groundbreaking capabilities offered by the James Webb Space Telescope (*JWST*) (e.g., Curtis-Lake et al. 2023; Zavala et al. 2024a). While initial follow-up with the Atacama Large Millimeter/submillimeter Array (ALMA) of bright *JWST* targets was largely unsuccessful (e.g. Bakx et al. 2023; Popping 2023; Yoon et al. 2023; Fujimoto et al. 2023; Kaasinen et al. 2023), this changed with the detection of $[OIII]_{88\mu m}$ in JADES-GS-z14-0 (hereafter GS-z14) at $z = 14.1793 \pm 0.0007$ (Carniani et al. 2024a; Schouws et al. 2024) and GHZ2/GLASSz12 at $z = 12.3327 \pm 0.0035$ (Zavala et al. 2024b). This has provided a new and unique view of these galaxies, revealing a rapid build-up of metals, relatively low densities and potentially a low gas fraction (Carniani et al. 2024a; Schouws et al. 2024; Zavala et al. 2024b) and has opened the door for further studies of $z > 10$ galaxies with ALMA.

These developments have provided a glimpse into the physical conditions of the interstellar medium (ISM) for the earliest galaxies, which has been a longstanding goal in high redshift astronomy (e.g., Robertson 2022). Emission lines provide us with key information to constrain these physical conditions. The advent of *JWST* has revolutionized the detection of rest-frame optical emission lines that have traditionally been essential to characterize the ISM. However, this becomes much more challenging at $z > 9.5$ when strong rest-frame optical emission lines like [OIII]$\lambda\lambda$4959,5007Å and Hβ move out of the spectral coverage of NIRSpec. While these lines can still be targeted by MIRI (Zavala et al. 2024a; Álvarez-Márquez et al. 2024), the cost is much higher due to the lower sensitivity of MIRI and lack of multiplexing. In this regime, ALMA can provide competitive and complementary insights that rival or exceed those possible with *JWST* (Schouws et al. 2024; Carniani et al. 2024a).

The aim of this study is to report on new deep $[CII]_{158\mu m}$ observations of GS-z14, currently the most distant spectroscopically-confirmed galaxy known. GS-z14 has measurements of $[OIII]_{88\mu m}$, CIII]$\lambda\lambda$1907,9Å, and a photometric constraint on [OIII]$\lambda\lambda$4959,5007Å+ Hβ (Carniani et al. 2024b,a; Schouws et al. 2024; Helton et al. 2024). Although this makes GS-z14 one of the best characterized $z > 10$ galaxies, this suite of emission lines is insufficient for an unambiguous characterization of its ISM, with sizable uncertainties in key parameters, particularly the ionization parameter (Carniani et al. 2024a; Schouws et al. 2024). Fortunately, with sensitive observations of $[CII]_{158\mu m}$ we can substantially reduce many existing uncertainties in our modeling of the ISM conditions of GS-z14.

Of particular relevance is the $[OIII]_{88\mu m}/[CII]_{158\mu m}$ ratio (hereafter [OIII]/[CII]), which provides us with invaluable constraints on the ionization conditions in the ISM (e.g. Arata et al. 2020; Harikane et al. 2023; Katz et al. 2022). This ratio also has been a key focus of study both in the local universe and galaxies at $z \sim$ 6-9, facilitating direct comparisons to our observational results (Inoue et al. 2016; Hashimoto et al. 2019; Laporte et al. 2019; Bakx et al. 2020; Carniani et al. 2020; Harikane et al. 2020; Akins et al. 2022; Witstok et al. 2022; Algera et al. 2024; Bakx et al. 2024; Fujimoto et al. 2024).

Throughout this paper we assume a standard ΛCDM cosmology with $H_0 = 70$ km s^{-1} Mpc^{-1}, $\Omega_m = 0.3$ and $\Omega_\Lambda = 0.7$. Magnitudes are presented in the AB system (Oke & Gunn 1983). For star formation rates (SFR) and stellar masses, we adopt a Chabrier initial mass function (Chabrier 2003). Error-bars indicate the 68% confidence interval unless specified otherwise. All measured and derived physical quantities are corrected for gravitational lensing by a factor of 1.17× (Carniani et al. 2024b). Logarithms use base 10 unless specified otherwise.

5.2 OBSERVATIONS AND DATA-REDUCTION

5.2.1 *Previous Observations*

GS-z14 is the most distant galaxy currently known and simultaneously the second most luminous $z > 8$ galaxy with a spectroscopic redshift (only GN-z11 is more luminous by a factor ∼2×: Oesch et al. 2016; Bunker et al. 2023). In contrast to other bright $z > 10$ galaxies (e.g., GN-z11 or GHZ2: Castellano et al. 2024), GS-z14 has a relatively extended morphology (FWHM∼0.16″), indicating that its luminosity is primarily driven by star formation as opposed to an active galactic nucleus (AGN).

It was initially discovered in deep imaging of the GOODS-South field obtained by the *JWST* Advanced Deep Extragalactic Survey (JADES; Eisenstein et al. 2023a), the First Reionization Epoch Spectroscopic COmplete Survey (FRESCO; Oesch et al. 2023), and JADES Origins Field (JOF) program (Eisenstein et al. 2023b) and subsequently targeted for follow-up spectroscopy with NIRSpec.

The NIRSpec spectroscopy showed a strong break at ∼1.85μm, consistent with a Lyman break at $z \sim 14$, but also a lack of strong rest-frame

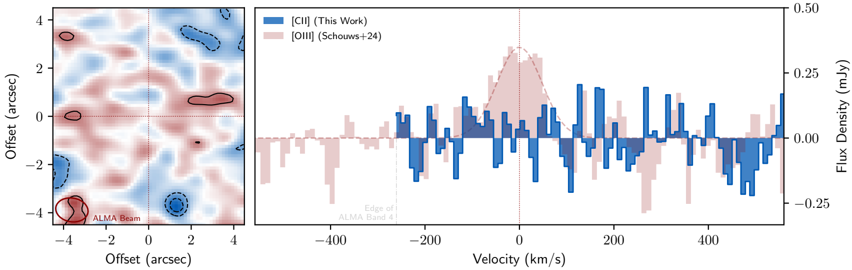

Figure 5.1. Sensitive constraints just obtained on $[CII]_{158\mu m}$ emission from GS-z14 with ALMA (2024.A.00007.S: PI Schouws). *Left Panel:* Moment-0 map collapsed over 130 km/s at the expected frequency of $[CII]_{158\mu m}$. To provide a sense of the noise levels, a 10"×10" area is presented, with contours drawn at the −3, −2, 2 and 3-σ levels, where dashed contours are used for the negative significance levels. The ALMA beam-size is shown as a red ellipse in the lower left corner. The position of GS-z14 is highlighted by the red cross-hairs at the center. *Right Panel:* Spectrum extracted within a 0.5″aperture centered on the position of GS-z14 (*blue bars*). A small amount of smoothing (bin size of 2-spectral elements) is applied. The spectral coverage is limited due to its proximity of $[CII]_{158\mu m}$ to the edge of ALMA Band 4 at 125 GHz. For context, emission from $[OIII]_{88\mu m}$ line is also using a similar aperture and extraction scheme (*red bars*). The red-dashed line shows the Schouws et al. (2024) fit to the $[OIII]_{88\mu m}$ line. It is clear that $[CII]_{158\mu m}$ is not detected. (We note that equal flux in both lines would result in a ratio [OIII]/[CII]∼1.8 due to the dependence of the derived luminosity on frequency, e.g., Solomon et al. 1992).

UV emission lines, resulting in considerable uncertainty in the spectroscopic redshift estimate ($z = 14.32^{+0.08}_{-0.20}$) (Carniani et al. 2024b).

GS-z14 was subsequently targeted in an ALMA DDT programme (#2023.A.00037.S: PI Schouws) to scan for the luminous $[OIII]_{88\mu m}$ line. These observations were successful, resulting in a 6.6σ detection of the $[OIII]_{88\mu m}$ line at z=14.1793±0.0007 in only 2.3 hours on-source integration (Carniani et al. 2024a; Schouws et al. 2024). The discovered $[OIII]_{88\mu m}$ line detection further confirmed the reality of the tentative 3.7σ CIII]$\lambda\lambda$1907,9Å line candidate that was previously identified in the NIRSpec spectroscopy.

Finally, GS-z14 is also detected by MIRI in the F770W filter (Helton et al. 2024). This filter covers the rest-frame optical emission of GS-z14, corresponding to wavelengths of 4.4 to 5.7μm, enabling a constraint on the luminosity of the strong [OIII]$\lambda\lambda$4959,5007Å and Hβ emission lines.

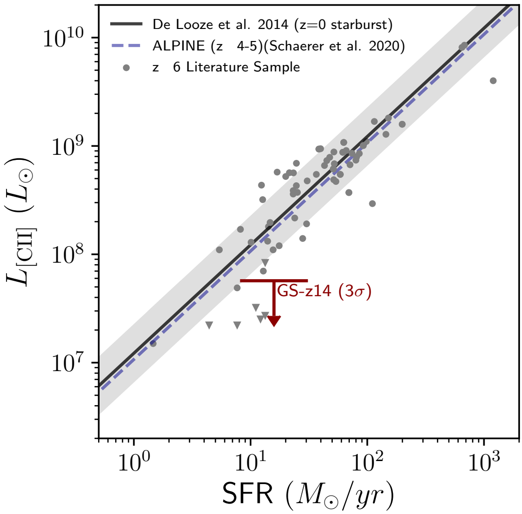

Figure 5.2. Comparison of the limiting $[CII]_{158\mu m}$ luminosity (*downward arrow*) inferred from GS-z14 against its SFR. The horizontal line associated with the upper limit extends over the full range in SFR derived for GS-z14 from Carniani et al. (2024b) and Helton et al. (2024). Previous studies have revealed a tight correlation between the SFR and $L_{[CII]}$ in local galaxies (De Looze et al. 2014) and at high-redshift (e.g. Carniani et al. 2017; Schaerer et al. 2020, Schouws et al. in prep.) GS-z14 lies below the relation over the full range of SFRs.

5.2.2 *ALMA $[CII]_{158\mu m}$ Follow-up*

The observations presented in this work were obtained as part of a Cycle 11 Director's Discretionary Time (DDT) program (#2024.A.00007.S, PI: Schouws). We target the $[CII]_{158\mu m}$ line, which is expected at 125.20 GHz and falls just within ALMA Band 4 (i.e. within 0.2 GHz from the edge of the band). We use a standard observing set-up with a single tuning and two spectral windows in each of the side-bands.

The observations were carried out between 11 and 19 January 2025 with an average PWV of 2.38mm (ranging from 1.67mm to 2.98mm), achieving the requested sensitivity in 8.15 hours on-source (12.2 hours including overheads). The target was observed with a moderately compact configuration with baselines ranging from 15m to 783m, resulting in a natural-weighted synthesized beam with a resolution of $1.35{\times}0.99''$ at the expected frequency of $[CII]_{158\mu m}$. At this resolution, we expect that all $[CII]_{158\mu m}$ flux from GS-z14 lies within a single beam, preventing signal dilution and loss of S/N (e.g. Carniani et al. 2020). The resolution is furthermore similar to the previous observations targeting the $[OIII]_{88\mu m}$ line (Schouws et al. 2024).

For the imaging, we use reduced and calibrated measurement sets obtained through the ALMA archival data service. The individual measurement sets are combined and time-averaged in bins of 30 seconds to reduce data-volume and we carefully verify that time-average smearing does not impact fluxes even at the edge of the field of view (e.g. Thompson et al. 2017).

Imaging of the calibrated visibilities was performed with natural weighting using the TCLEAN task in CASA (v6.6.1-17) (CASA; Hunter et al. 2023). We clean to a depth of 3σ using automasking with the recommended settings for low-resolution ALMA data (Kepley et al. 2020). At the expected $[CII]_{158\mu m}$ frequency, we generate a moment-0 map including channels within 130 km/s, to approximately match the inferred FWHM of the $[OIII]_{88\mu m}$ line (126 km/s). The resulting moment-0 map has a rms of 7.2 mJy·km/s.

We do not detect continuum emission from GS-z14, constraining the flux to $< 9.5\,\mu\text{Jy}\,\text{beam}^{-1}$ (3σ). This is slightly deeper than the previous constraints from the ALMA Band 6 observations ($< 15.1\,\mu\text{Jy}\,\text{beam}^{-1}$), but does not improve constraints on the dust content of GS-z14 due to the shape of the dust SED. We therefore refer to Schouws et al. (2024) for a more detailed discussion on the dust content of GS-z14.

5.3 RESULTS

5.3.1 *Non-detection of* $[CII]_{158\mu m}$

We do not detect significant emission at the location and expected $[CII]_{158\mu m}$ frequency of GS-z14. This is illustrated in Figure 5.1, where we show the moment-0 map and spectrum as extracted within an aperture with a diameter of 0.5″ centered on GS-z14. We do not even find evidence for tentative ($\sim$1-2σ) $[CII]_{158\mu m}$ emission from GS-z14. For context, we also include the extracted spectrum of $[OIII]_{88\mu m}$ for GS-z14 using the same method.

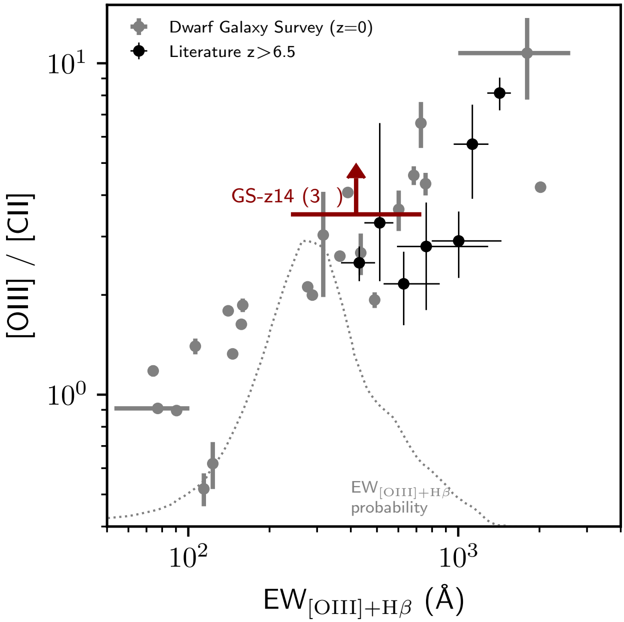

Figure 5.3. [OIII]/[CII] ratio as a function of [OIII]$_{4959,5007}$+Hβ equivalent width. GS-z14 is shown as a lower limit (maroon), and its EW probability distribution from Helton et al. (2024) is overlaid via the dotted line. High-z galaxies from the literature are overplotted as black markers (Witstok et al. 2022; Algera et al. in preparation). Moreover, low-redshift galaxies from the Dwarf Galaxy Survey are shown as grey symbols (Kumari et al. 2024).

Based on the rms of the moment-0 map, we therefore constrain the apparent [CII]$_{158\mu m}$ flux to be below <22 mJy·km/s (3σ). This corresponds to a limiting luminosity of $<6\times10^7$ L$_\odot$ (corrected for lensing)[1].

[1] The impact of the cosmic microwave background (CMB) on [CII]$_{158\mu m}$ (assuming optically thin transmission) can be estimated by η=F$_\nu^{obs}$/F$_\nu^{intr}$=$1 - B_\nu(T_{CMB})/B_\nu(T_{spin}^{[CII]})$ (e.g. Kohandel et al. 2019). The CMB temperature at this redshift is $T_{CMB} = 41.4$K and the [CII]$_{158\mu m}$ spin temperature depends strongly on the ISM conditions of the emitting gas. At high redshifts [CII]$_{158\mu m}$ primarily originates from photo-dissociation region (PDR) (e.g. Gullberg et al. 2015; Novak et al. 2019; Cormier et al. 2019), which have relatively high densities ($log(n_e) \sim 2-4$). Given the extreme nature of GS-z14, the kinetic temperature is likely to be high ($T_{kin} \sim 500-1000$K). Based on this, we estimate a spin temperature of $T_{spin}^{[CII]} = 100 - 1000$K (Gong et al. 2012). This gives $\eta \approx 0.60 - 0.96$, implying a potentially modest suppression of signal from the CMB. Given the large uncertainty in the physical properties of the [CII]$_{158\mu m}$ emitting gas in GS-z14, the reported [CII]$_{158\mu m}$ luminosities in the paper are not corrected for the impact of the CMB

Galaxies in the local and high redshift universe show a moderately tight correlation between their SFRs and $[CII]_{158\mu m}$ luminosities (De Looze et al. 2014; Herrera-Camus et al. 2015; Schaerer et al. 2020). In Figure 5.2, we show that the $[CII]_{158\mu m}$ luminosity of GS-z14 lies below this relation. The estimated SFR of GS-z14 ranges from 10^{+2}_{-2} $M_\odot$/yr (Carniani et al. 2024b) to 25^{+6}_{-5} $M_\odot$/yr (Helton et al. 2024). Depending on the assumed SFR, GS-z14 falls either well below the relation or is marginally consistent, given the observed 0.3dex scatter in the local relation (De Looze et al. 2014). For the lower SFR estimates, the $[CII]_{158\mu m}$ deficit in GS-z14 would be a good match to the deficiency seen in other high redshift galaxies (e.g. Harikane et al. 2020; Binggeli et al. 2021; Glazer et al. 2024). This may therefore indicate that the SFR estimate of Helton et al. (2024) for GS-z14 is too high.

Leveraging our earlier determination of the $[OIII]_{88\mu m}$ luminosity (2.1×10^8 $L_\odot$: Schouws et al. 2024) for GS-z14, we constrain the $[OIII]_{88\mu m}$ to $[CII]_{158\mu m}$ ratio to be >3.5. This is consistent with what is typically observed for $z\sim6$ - 9 galaxies, which show line ratios of [OIII]/[CII] $\approx 2-10$ (e.g. Harikane et al. 2020; Carniani et al. 2020; Witstok et al. 2022; Algera et al. 2024).

ISM modelling has shown that the [OIII]/[CII] ratio correlates with the ionization parameter, which can be elevated by bursts of recent star formation (e.g. Ferrara et al. 2019; Algera et al. 2024). Observationally, recent bursts in star formation result also enhance the equivalent width of [OIII]$\lambda\lambda$4959,5007Å+Hβ (hereafter $EW_{[OIII]+H\beta}$) due to an increased contrast between enhanced emission lines driven by recent star formation and the underlying stellar continuum.

These effects result in a tight correlation between $EW_{[OIII]+H\beta}$ and [OIII]/[CII] as shown in Figure 5.3, we also show our constraint on [OIII]/[CII] for GS-z14 in this figure together with the estimate for $EW_{[OIII]+H\beta}$ from Helton et al. (2024) (370^{+360}_{-130} Å). Our constraint implies that [OIII]/[CII] in GS-z14 is be higher than expected based on its $EW_{[OIII]+H\beta}$, but could also imply that $EW_{[OIII]+H\beta}$ might be underestimated by Helton et al. (2024).

We discuss the physical implications of the [OIII]/[CII] ratio of GS-z14 in the context of the known high-redshift galaxy population in the next section.

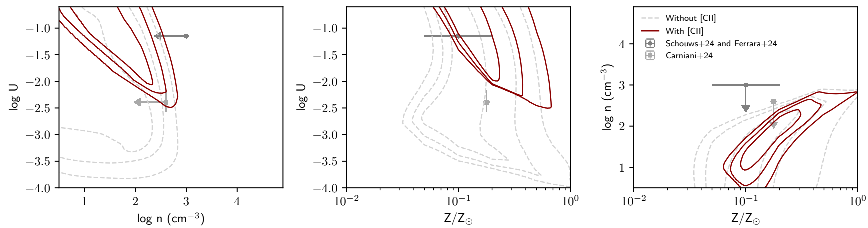

Figure 5.4. Constraints on the ISM of GS-z14. Each panel shows constraints on two ISM properties while we marginalize over the remaining parameter. We show 1, 2 and 3σ constraints for fits both with and without the constraints on $[CII]_{158\mu m}$ (red and gray dashed contours, respectively). The inclusion of $[CII]_{158\mu m}$ significantly improves the constraints on the ISM properties, particularly the ionization parameter. For reference we also indicate previous estimates on the ISM properties of GS-z14 from Carniani et al. (2024a) and Schouws et al. (2024) (with log(U) estimated by Ferrara 2024).

5.4 DISCUSSION

5.4.1 *Constraints on the ISM of GS-z14*

The detection of line emission from galaxies (or physically meaningful limits) provides us with a powerful way to constrain the ISM conditions in galaxies. In the case of GS-z14, flux measurements are available for $[OIII]_{88\mu m}$ and CIII]$\lambda\lambda$1907,9Å lines, an upper limit is now available on $[CII]_{158\mu m}$, and finally [OIII]$\lambda\lambda$4959,5007Å+ Hβ fluxes have constraints thanks to deep MIRI photometry on the source (Carniani et al. 2024b,a; Helton et al. 2024; Schouws et al. 2024).

To enable a constraint on the ISM properties of GS-z14 based on these measurements, we use Bayesian inference on an extensive grid of photoionization models made with Cloudy (v17.02; Ferland et al. 2017). In particular, the models consist of an HII region that smoothly transitions into a PDR until a fixed optical depth (A_V=10) in a plane parallel geometry. The models have three main parameters to describe the ISM, the ionization parameter (U), density (n) and metallicity (Z). For more details on the models, we refer to Witstok et al. (2022).

In Figure 5.4, we show the results of our fitting, both with and without our new constraints on the $[CII]_{158\mu m}$ luminosity of GS-z14. The current emission line constraints are well described by models with a high ionization parameter, low density, and moderate metallicity (see Table 5.1).

This is consistent with previous modeling efforts of the ISM of high redshift galaxies (e.g. Harikane et al. 2020; Katz et al. 2022; Nakazato et al.

2023), showing that high ionization parameters are necessary to explain the high observed [OIII]/[CII] ratios at $z > 6$. Our analysis suggests that GS-z14 has a high $\log(U) > -2$, which is consistent with the range of ionization parameters found by Reddy et al. (2023) and Tang et al. (2023) for a sample of $z \approx$ 3-9 galaxies observed with *JWST*/NIRSpec ($-3 \lesssim \log U \lesssim -1.5$). Moreover, the inferred value for GS-z14 is consistent with the ionization parameter of GHZ2, for which Calabrò et al. (2024) infer $\log(U) = -1.75 \pm 0.16$. This suggests that high ionization parameters are ubiquitous in the early Universe.

On the other hand, earlier estimates preferred lower values for the ionization parameter for GS-z14. For instance, Helton et al. (2024) measured $\log(U) \approx -2.5$ from NIRCam and MIRI F770W photometry, with the latter band containing the photometric signature of the $[\mathrm{OIII}]_{4959,5007}$ and Hβ lines. Similarly, Carniani et al. (2024a) inferred a fiducial value of $\log(U) = -2.39^{+0.23}_{-0.19}$ by also including the ALMA $[\mathrm{OIII}]_{88\mu m}$ detection in GS-z14. The higher $\log(U) > -2$ we infer here highlights the value of our current probe of $[\mathrm{CII}]_{158\mu m}$ has for breaking the degeneracy between ionization parameter, density and metallicity.

While a high ionization parameter is a possible driver of the high [OIII]/[CII] ratios of distant galaxies (e.g., Harikane et al. 2020), other interpretations exist in the literature. For example, a low PDR covering fraction is also expected to result in a high [OIII]/[CII] ratio (Harikane et al. 2020), and is qualitatively consistent with the low inferred gas fraction for GS-z14, which may suggest it hosts an outflow (Section 5.4.2).

Finally, the production of carbon is thought to lag behind that of oxygen, which is also expected to result in elevated [OIII]/[CII] ratios (e.g., Katz et al. 2022; Fujimoto et al. 2024; Nyhagen et al. 2024). However, leveraging the CIII]$\lambda\lambda$1907,9Å detection for GS-z14, Carniani et al. (2024a) do not find evidence for an elevated C/O abundance in the galaxy, although the uncertainties on the abundance ratio are large.

5.4.2 *Low Gas Content in GS-z14: Evidence for A Post Outflow Phase?*

In recent years, the $[\mathrm{CII}]_{158\mu m}$ line has seen frequent use as a molecular gas mass tracer at high redshift (e.g., Zanella et al. 2018; Dessauges-Zavadsky et al. 2020; Aravena et al. 2024), owing to the faintness of canonical cold gas tracers such as CO at this epoch. While the precise conversion from $[\mathrm{CII}]_{158\mu m}$ luminosity to molecular gas mass remains debated (e.g., Casavecchia et al. 2024; Algera et al. 2025), we use the commonly adopted

Table 5.1. Properties of GS-z14

Parameter	**Value**
RA	03:32:19.9049
Dec	−27:51:20.265
Redshift	14.1793(7)
M_{UV} [a]	-20.81 ± 0.16
Stellar Mass($\log(M_\odot)$)[b]	$8.7^{+0.5}_{-0.4}$
Star Formation Rate ($M_\odot$/yr)	10^{+2}_{-2} [(a)] ; 25^{+6}_{-5} [(b)]
CIII] Luminosity (10^8 $L_\odot$)[a]	2.0±0.5[c]
[OIII]+Hβ Luminosity (10^8 $L_\odot$)[b]	22±10[c]
$[\mathrm{OIII}]_{88\mu m}$ Luminosity (10^8 $L_\odot$)[d]	2.1±0.5
$[\mathrm{CII}]_{158\mu m}$ Luminosity (10^8 $L_\odot$)	< 0.6[e]
[OIII]/[CII]	> 3.5[e]
log(U)[f]	> -2.0[g]
log(n) (cm^{-3})[f]	$1.7^{+0.5}_{-0.4}$
$Z/Z_\odot$[f]	$0.16^{+0.06}_{-0.06}$

Notes: All values have been corrected for a lensing magnification of 1.17× (Carniani et al. 2024b). [a] Value from Carniani et al. (2024b); [b] Value from Helton et al. (2024); [c] Corrected for extinction; [d] Value from Schouws et al. (2024); [e] 3σ limit; [f] Based on the ISM fitting presented in this work; [g] 95% confidence interval.

value from Zanella et al. (2018) of $M_{\mathrm{mol}}/M_\odot = 31 L_{[\mathrm{CII}]_{158\mu m}}/L_\odot$ to place an upper limit on the molecular gas mass of GS-z14 of $\log(M_{\mathrm{mol}}/M_\odot) < 9.2$ (3σ).

Adopting the stellar mass from Helton et al. (2024) (Table 5.1), the $[\mathrm{CII}]_{158\mu m}$-based gas mass estimate implies a gas fraction of $f_{\mathrm{gas,mol}} = M_{\mathrm{mol}}/(M_{\mathrm{mol}} + M_\star) < 0.77$ for GS-z14. This is significantly below what is expected for a galaxy with a metallicity of $Z/Z_\odot \sim 0.1 - 0.2$ (c.f., $f_{\mathrm{gas,mol}} \gtrsim 0.9$; e.g., De Vis et al. 2019; Algera et al. 2025), which may suggest the gas in GS-z14 is efficiently expelled through outflows.

The low $[\mathrm{CII}]_{158\mu m}$ based gas mass estimate is consistent with the low dynamical mass of GS-z14 based on the line width of the $[\mathrm{OIII}]_{88\mu m}$ line of $\log(M_{\mathrm{dyn}}/M_\odot) \sim 9.0$ (Carniani et al. 2024a; Schouws et al. 2024). After subtracting the stellar mass, this dynamical estimate would imply a gas fraction of only ∼30% (Carniani et al. 2024a).

Further evidence for feedback comes from the lack of dust in GS-z14 as implied by the low A_V=0.31 (Carniani et al. 2024b) and non-detection of the dust continuum by ALMA (Carniani et al. 2024a; Schouws et al. 2024;

Algera et al. 2025). Dust enrichment is expected to follow rapidly after the onset of star formation as a consequence of production by Supernovae and for the observed stellar mass, GS-z14 should consequently be detectable with ALMA if all the dust was still present.

Detailed modeling of GS-z14 by Ferrara (2024) and Ferrara et al. (2024) suggests that the galaxy recently experienced an outflow, causing its dust to be blown out to large radii. Such an extended dust distribution is subject to a less intense radiation field, enabling it to efficiently cool, and rendering it undetectable at the current depth of the ALMA observations while also explaining the low A_V as observed by *JWST*. Following this previous outflow event, Ferrara et al. (2024) suggest that GS-z14 currently resides in a 'post-outflow' phase, characterized by a low current SFR and little obscuration. In other words, the observable properties of GS-z14 appear to be shaped by strong feedback from the galaxy.

Finally, this would also be qualitatively consistent with the high ionization parameter and low density we infer from our observations. The same star-bursting phase would not only produce a young stellar population and high ionization parameter (e.g. Reddy et al. 2023), but also drive strong feedback in the galaxies, expelling or otherwise puffing up its gas reservoir, leaving the source with the low gas density we infer ($n \sim 50\,\mathrm{cm}^{-3}$: well below the typical densities observed for $z \gtrsim 6$ galaxies, e.g., Isobe et al. 2023).

5.5 SUMMARY

We presented new results based on sensitive ALMA observations of the $[\mathrm{CII}]_{158\mu m}$ line in JADES-GS-z14-0, the most distant galaxy currently known at $z = 14.1793 \pm 0.0007$ (Carniani et al. 2024b,a; Schouws et al. 2024). Our main conclusions are as follows:

- We do not detect the $[\mathrm{CII}]_{158\mu m}$ line in GS-z14 down to a (lensing-corrected) luminosity of $L_{[\mathrm{CII}]_{158\mu m}} < 6 \times 10^7\,L_\odot$ at 3σ (Figure 5.1). This places the galaxy below the $[\mathrm{CII}]_{158\mu m}$-SFR relation (Figure 5.2), which is qualitatively consistent with what has been observed for low-SFR galaxies at $z \approx 6-9$ (Harikane et al. 2020; Binggeli et al. 2021; Glazer et al. 2024).

- Combined with a previous detection of the $[\mathrm{OIII}]_{88\mu m}$ line in GS-z14 (Carniani et al. 2024a; Schouws et al. 2024), we infer a lower limit on its [OIII]/[CII] ratio of > 3.5 (Figure 5.3). While larger than what is typically seen in galaxies in the local Universe, this elevated line ratio is consistent with that seen in many z∼6-9 galaxies (e.g. Inoue et al. 2016).

- Leveraging the sensitive constraints on the $[\mathrm{CII}]_{158\mu m}$ luminosity, we investigate the ISM conditions of GS-z14 (Figure 5.4). In agreement with analyses by Carniani et al. (2024b,a) and our own analysis (Schouws et al. 2024), we find that GS-z14 is already significantly metal-enriched, with $Z/Z_{\odot} = 0.16 \pm 0.06$. Crucially, our new $[\mathrm{CII}]_{158\mu m}$ observations allow us to break a previously existing degeneracy between the ionization parameter U and density of GS-z14. We find an ionization parameter of $\log(U) > -2$, higher than what was previously inferred for the galaxy. Moreover, we infer a low density for $\log(n/\mathrm{cm}^{-3})$ of $1.7^{+0.5}_{-0.4}$.
- Using $[\mathrm{CII}]_{158\mu m}$ as a gas mass tracer, we infer a low molecular gas fraction of $f_{\mathrm{gas,mol}} < 0.77$ for GS-z14, consistent with that obtained via a dynamical estimate from the previously detected $[\mathrm{OIII}]_{88\mu m}$ line (Carniani et al. 2024a). This is lower than expected for galaxies at a metallicity similar to GS-z14 (e.g., see Algera et al. 2025), suggesting the efficient removal of its gas through outflows.

Overall, the high ionization parameter, low gas density, lack of dust, and low gas fraction of GS-z14 suggest the galaxy is subject to strong feedback effects, likely driven by its star-bursting nature. These extreme physical conditions highlight the complex nature of galaxy formation in the early Universe.

ACKNOWLEDGMENTS

This paper makes use of the following ALMA data: ADS/JAO.ALMA 2024.A.00007.S and 2023.A.00037.S. ALMA is a partnership of ESO (representing its member states), NSF (USA) and NINS (Japan), together with NRC (Canada), MOST and ASIAA (Taiwan), and KASI (Republic of Korea), in cooperation with the Republic of Chile. The Joint ALMA Observatory is operated by ESO, AUI/NRAO and NAOJ. We are greatly appreciative to our ALMA program coordinator Megan Lewis and also Violette Impellizzeri for support with our ALMA program and Allegro, the European ALMA Regional Center node in the Netherlands. We are grateful to J. Witstok for providing the Cloudy models from Witstok et al. (2022) for the analysis conducted in this paper. We thank M. Kohandel and A. Pallottini for simulated data analysis. AF acknowledges support from the ERC Advanced Grant INTERSTELLAR H2020/740120 and support from the grant NSF PHY-2309135 to the Kavli Institute for Theoretical Physics (KITP).

REFERENCES

Akins, H. B., Fujimoto, S., Finlator, K., et al. 2022, ApJ, 934, 64,

Algera, H., Rowland, L., Stefanon, M., et al. 2025, arXiv e-prints, arXiv:2501.10508,

Algera, H. S. B., Inami, H., Sommovigo, L., et al. 2024, MNRAS, 527, 6867,

Álvarez-Márquez, J., Crespo Gómez, A., Colina, L., et al. 2024, arXiv e-prints, arXiv:2412.12826,

Arata, S., Yajima, H., Nagamine, K., Abe, M., & Khochfar, S. 2020, MNRAS, 498, 5541,

Aravena, M., Heintz, K., Dessauges-Zavadsky, M., et al. 2024, A&A, 682, A24,

Bakx, T. J. L. C., Tamura, Y., Hashimoto, T., et al. 2020, MNRAS, 493, 4294,

Bakx, T. J. L. C., Zavala, J. A., Mitsuhashi, I., et al. 2023, MNRAS, 519, 5076,

Bakx, T. J. L. C., Algera, H. S. B., Venemans, B., et al. 2024, MNRAS, 532, 2270,

Binggeli, C., Inoue, A. K., Hashimoto, T., et al. 2021, A&A, 646, A26,

Bunker, A. J., Saxena, A., Cameron, A. J., et al. 2023, A&A, 677, A88,

Calabrò, A., Castellano, M., Zavala, J. A., et al. 2024, ApJ, 975, 245,

Carniani, S., Maiolino, R., Pallottini, A., et al. 2017, A&A, 605, A42, Carniani, S., Ferrara, A., Maiolino, R., et al. 2020, MNRAS, 499, 5136,

Carniani, S., D'Eugenio, F., Ji, X., et al. 2024a, arXiv e-prints, arXiv:2409.20533,

Carniani, S., Hainline, K., D'Eugenio, F., et al. 2024b, Nature, 633, 318,

Casavecchia, B., Maio, U., Péroux, C., & Ciardi, B. 2024, A&A, 689, A106,

Castellano, M., Napolitano, L., Fontana, A., et al. 2024, ApJ, 972, 143,

Chabrier, G. 2003, PASP, 115, 763,

Cormier, D., Abel, N. P., Hony, S., et al. 2019, A&A, 626, A23,

Curtis-Lake, E., Carniani, S., Cameron, A., et al. 2023, Nature Astronomy, 7, 622,

De Looze, I., Cormier, D., Lebouteiller, V., et al. 2014, A&A, 568, A62,

De Vis, P., Jones, A., Viaene, S., et al. 2019, A&A, 623, A5,

Dessauges-Zavadsky, M., Ginolfi, M., Pozzi, F., et al. 2020, A&A, 643, A5,

Eisenstein, D. J., Willott, C., Alberts, S., et al. 2023a, arXiv e-prints, arXiv:2306.02465,

Eisenstein, D. J., Johnson, B. D., Robertson, B., et al. 2023b, arXiv e-prints, arXiv:2310.12340,

Ferland, G. J., Chatzikos, M., Guzmán, F., et al. 2017, RMxAA, 53, 385.

Ferrara, A. 2024, A&A, 689, A310,

Ferrara, A., Carniani, S., di Mascia, F., et al. 2024.

Ferrara, A., Vallini, L., Pallottini, A., et al. 2019, MNRAS, 489, 1,

Fujimoto, S., Finkelstein, S. L., Burgarella, D., et al. 2023, ApJ, 955, 130,

Fujimoto, S., Ouchi, M., Nakajima, K., et al. 2024, ApJ, 964, 146,

Glazer, K., Bradăc, M., Sanders, R. L., et al. 2024, MNRAS, 531, 945,

Gong, Y., Cooray, A., Silva, M., et al. 2012, ApJ, 745, 49,

Gullberg, B., De Breuck, C., Vieira, J. D., et al. 2015, MNRAS, 449, 2883,

Harikane, Y., Ouchi, M., Inoue, A. K., et al. 2020, ApJ, 896, 93,

Harikane, Y., Ouchi, M., Oguri, M., et al. 2023, ApJS, 265, 5,

Hashimoto, T., Inoue, A. K., Mawatari, K., et al. 2019, PASJ, 71, 71,

Helton, J. M., Rieke, G. H., Alberts, S., et al. 2024.

Herrera-Camus, R., Bolatto, A. D., Wolfire, M. G., et al. 2015, ApJ, 800, 1,

Hunter, T. R., Indebetouw, R., Brogan, C. L., et al. 2023, Publications of the Astronomical Society of the Pacific, 135, 074501,

Inoue, A. K., Tamura, Y., Matsuo, H., et al. 2016, Science, 352, 1559,

Isobe, Y., Ouchi, M., Nakajima, K., et al. 2023, ApJ, 956, 139,

Kaasinen, M., van Marrewijk, J., Popping, G., et al. 2023, A&A, 671, A29,

Katz, H., Rosdahl, J., Kimm, T., et al. 2022, MNRAS, 510, 5603,

Kepley, A. A., Tsutsumi, T., Brogan, C. L., et al. 2020, PASP, 132, 024505,

Kohandel, M., Pallottini, A., Ferrara, A., et al. 2019, MNRAS, 487, 3007,

Kumari, N., Smit, R., Leitherer, C., et al. 2024, MNRAS, 529, 781, Laporte, N., Katz, H., Ellis, R. S., et al. 2019, MNRAS, 487, L81,

Nakazato, Y., Yoshida, N., & Ceverino, D. 2023, ApJ, 953, 140,

Novak, M., Bañados, E., Decarli, R., et al. 2019, ApJ, 881, 63,

Nyhagen, C. T., Schimek, A., Cicone, C., Decataldo, D., & Shen, S. 2024, arXiv e-prints, arXiv:2410.18471,

Oesch, P. A., Brammer, G., Dokkum, P. G. v., et al. 2016, The Astrophysical Journal, 819, 129,

Oesch, P. A., Brammer, G., Naidu, R. P., et al. 2023, MNRAS, 525, 2864,

Oke, J. B., & Gunn, J. E. 1983, ApJ, 266, 713,

Popping, G. 2023, Astronomy & Astrophysics, 669, L8,

Reddy, N. A., Topping, M. W., Sanders, R. L., Shapley, A. E., & Brammer, G. 2023, ApJ, 952, 167,

Robertson, B. E. 2022, ARA&A, 60, 121,

Schaerer, D., Ginolfi, M., Béthermin, M., et al. 2020, A&A, 643, A3,

Schouws, S., Bouwens, R. J., Ormerod, K., et al. 2024, arXiv e-prints, arXiv:2409.20549,

Solomon, P. M., Downes, D., & Radford, S. J. E. 1992, ApJL, 387, L55,

Tang, M., Stark, D. P., Chen, Z., et al. 2023, MNRAS, 526, 1657,

Thompson, A. R., Moran, J. M., & Swenson, George W., J. 2017, Interferometry and Synthesis in Radio Astronomy, 3rd Edition,

Witstok, J., Smit, R., Maiolino, R., et al. 2022, MNRAS, 515, 1751,

Yoon, I., Carilli, C. L., Fujimoto, S., et al. 2023, The Astrophysical Journal, 950, 61,

Zanella, A., Daddi, E., Magdis, G., et al. 2018, MNRAS, 481, 1976,

Zavala, J. A., Castellano, M., Akins, H. B., et al. 2024a, arXiv e-prints, arXiv:2403.10491,

Zavala, J. A., Bakx, T., Mitsuhashi, I., et al. 2024b, ApJL, 977, L9,

Nederlandse Samenvatting

Een reis terug in de tijd

Wanneer we ’s nachts naar de hemel kijken, zien we de sterren niet zoals ze nu zijn, maar zoals ze in het verleden waren. Omdat licht een vaste snelheid heeft (bijna 300.000 kilometer per seconde), kost het tijd voordat het licht van verre objecten ons bereikt. Hoe verder we het heelal in kijken, hoe verder we terugkijken in de tijd. Het heelal is ongeveer 13,8 miljard jaar oud. Met de huidige generatie telescopen kunnen we zó ver kijken, dat we sterrenstelsels waarnemen die al bestonden toen het heelal nog maar een fractie van zijn huidige leeftijd had: slechts een paar honderd miljoen jaar na de oerknal. Dit tijdperk markeert de ‘kosmische dageraad’, de periode waarin de allereerste sterren en sterrenstelsels het heelal begonnen te verlichten.

Het bestuderen van deze allereerste stelsels is echter een enorme uitdaging. Doordat het heelal uitdijt, wordt de ruimte zélf opgerekt. Hierdoor wordt het licht van verre stelsels uitgerekt terwijl het naar ons toe reist. De golflengte van het licht verschuift hierdoor naar het rodere, onzichtbare deel van het spectrum. Dit fenomeen noemen we roodverschuiving. Om sterrenstelsels in het vroege heelal te bestuderen, hebben we daarom telescopen nodig die heel gevoelig zijn voor infraroodstraling en radiogolven.

In de afgelopen jaren heeft de James Webb Space Telescope (JWST) spectaculaire ontdekkingen gedaan door het infrarode licht van vroege sterrenstelsels vast te leggen. In dit proefschrift maken we echter gebruik van een heel ander instrument: de Atacama Large Millimeter/submillimeter Array (ALMA). ALMA is een netwerk van meer dan vijftig radioschotels, gelegen op een hoogvlakte in Chili. In plaats van naar het licht van de sterren zelf te kijken, vangt ALMA submillimeterstraling op. Hiermee observeren we niet de sterren, maar de grondstoffen waaruit sterren worden geboren: de ijskoude wolken van gas en stof die de ruimte tussen de sterren vullen, en het gas dat door jonge sterren wordt verhit. Dit stof en gas maken deel uit van het Interstellaire Medium (ISM).

Het Interstellaire Medium en het Mysterie van ’Feedback’

Sterrenstelsels vormen zich in zogeheten ‘halo’s’ van donkere materie. De zwaartekracht van deze donkere materie trekt oergas (voornamelijk waterstof en helium) naar zich toe. Terwijl het gas naar binnen valt, warmt het op. Om nieuwe sterren te kunnen vormen, moet dit hete gas afkoelen en samentrekken. Dat afkoelen gebeurt doordat atomen en moleculen in het gas energie uitstralen.

Theoretische modellen voorspelden lange tijd dat bijna ál het gas in een halo snel zou moeten afkoelen en in sterren zou veranderen. In werkelijkheid observeren we dat sterrenstelsels veel minder efficiënt zijn in het vormen van sterren. Er moet dus een proces zijn dat het gas verhit, uit het stelsel verdrijft of verhindert af te koelen, zodat stervorming wordt afgeremd. In de sterrenkunde noemen we dit proces feedback. Deze feedback kan afkomstig zijn van de intense straling van jonge sterren, ontploffende sterren (supernova's) of superzware zwarte gaten. De grote open vraag is hoe deze feedbackprocessen precies werken en hoe ze de allereerste sterrenstelsels vormgaven.

Om de fysieke omstandigheden in deze vroege stelsels te meten, bestuderen we specifieke specifieke emissielijnen en kosmisch stof. Kosmisch stof bestaat uit piepkleine vaste deeltjes van zware elementen, zoals koolstof en silicaten, die voornamelijk geproduceerd worden tijdens supernova-explosies. Emissielijnen zijn als de vingerafdrukken van specifieke gassen (zoals geïoniseerd koolstof ([CII]) en zuurstof ([OIII])). Door de helderheid van deze lijnen met ALMA te meten, kunnen we de temperatuur, gasdichtheid en de chemische samenstelling (metalliciteit) van de stelsels bepalen.

Kosmisch stof en verborgen stervorming (Hoofdstuk 2)

In hoofdstuk 2 onderzoeken we een groep van vijftien zeer heldere sterrenstelsels toen het heelal ongeveer 700 tot 800 miljoen jaar oud was (een roodverschuiving van $z \sim 7-8$). Voor de komst van telescopen zoals ALMA werd de mate van stervorming in het vroege heelal vooral gemeten aan de hand van ultraviolet (UV) licht van jonge sterren. UV-licht wordt echter heel makkelijk geabsorbeerd door kosmisch stof. Het stof warmt hierdoor op en straalt de energie weer uit als ver-infrarode straling, wat wij met ALMA kunnen detecteren.

Voorheen werd aangenomen dat er zo vroeg in de geschiedenis van het heelal nog niet veel stof zou zijn. Uit onze diepe ALMA-waarnemingen blijkt echter dat we in maar liefst zes van deze stelsels grote hoeveelheden stof waarnemen. Door het UV-licht (zichtbare stervorming) te combineren met de ALMA-data (verborgen stervorming), toonden we aan dat zelfs in de vroegste tijdperken ongeveer één derde van de stervorming in zware stelsels door stof aan het zicht wordt onttrokken. Omdat deze stelsels zo jong zijn, betekent dit dat het stof in een extreem hoog tempo moet zijn geproduceerd, zeer waarschijnlijk door vroege supernova's.

ALMA als 'roodverschuivingsmachine' (Hoofdstuk 3)

Om de eigenschappen van vroege sterrenstelsels goed te kunnen bestuderen, is het cruciaal om hun exacte afstand te weten. Dit gebeurt door hun precieze roodverschuiving te bepalen. Vóór de lancering van JWST was dit enorm lastig, omdat we vanaf de aarde het benodigde licht door de blokkerende werking van de aardatmosfeer vaak niet konden zien.

In hoofdstuk 3 demonstreren we een innovatieve methode: we gebruikten ALMA om zonder vooraf bekende spectroscopische roodverschuiving een frequentiebereik af te zoeken naar de emissielijn van geïoniseerd koolstof ([CII]). We selecteerden hiervoor zes extreem heldere stelsels op basis van hun specifieke kleuren in archiefdata van de Spitzer-ruimtetelescoop. Dit bleek een efficiënte strategie: in 50% van de gevallen vonden we exact de gezochte koolstoflijn.

Deze waarnemingen gaven ons niet alleen de exacte roodverschuiving, maar onthulden ook de interne dynamiek van deze stelsels. Het koolstofsignaal is zo sterk dat we konden zien hóe het gas beweegt (kinematica). We ontdekten een verrassende diversiteit: één stelsel vertoonde de kalme, geordende rotatie van een schijf, een ander bleek de chaotische nasleep van twee op elkaar botsende sterrenstelsels (een merger), en een derde leek gedomineerd te worden door wilde interne turbulentie met lokaal extreem heldere klonters van stervorming.

Naar de Grens van het Heelal: GS-z14 (Hoofdstuk 4 & 5)

Hoofdstukken 4 en 5 richten zich op slechts één object, maar wel een hele speciale: JADES-GS-z14-0. Dit stelsel werd onlangs met de JWST ontdekt en was tot voor kort het verste sterrenstelsel dat de mensheid kende. We zien dit stelsel zoals het was op een roodverschuiving van $z=14.2$, wat betekent dat het heelal op dat moment slechts 300 miljoen jaar oud was (ongeveer 2% van de huidige leeftijd). Desondanks is dit stelsel bijzonder helder en groot.

In hoofdstuk 4 presenteren we de succesvolle ALMA-waarneming van geïoniseerde zuurstof ([OIII]) in dit stelsel. Dit was een opmerkelijke ontdekking. Om zuurstof te kunnen waarnemen, moesten eerdere generaties sterren in het stelsel (die nagenoeg volledig bestonden uit waterstof en helium) al in de kern zuurstof hebben geproduceerd, geëxplodeerd zijn, en dit zuurstof door het stelsel hebben verspreid. Onze detectie laat zien dat dit stelsel al opvallend rijk is aan “metalen” (astronomisch jargon voor elementen zwaarder dan helium). Dit bevestigt dat de evolutie van de eerste sterrenstelsels veel sneller verliep dan we voorheen voor mogelijk hielden.

In hoofdstuk 5 presenteren we vervolgonderzoek om nóg dieper naar de geheimen van GS-z14 te kijken. We scanden met ALMA langdurig naar de koolstoflijn [CII] (net als hoofdstuk 3) en koud stof, om zo te bepalen hoeveel koud gas (brandstof voor toekomstige sterren) er in het stelsel aanwezig is. Tot onze verbazing vonden we... niets. We registreerden uiterst lage bovengrenzen voor de hoeveelheid van dit koolstof.

Deze 'non-detectie' vertelt echter een cruciaal verhaal. De verhouding tussen de grote hoeveelheid zuurstof enerzijds, en het gebrek aan koolstof, koud stof en koud gas anderzijds, wijst op extreme omstandigheden in het stelsel. Uit onze modellen blijkt dat het gas in het stelsel niet alleen heel ijl is, maar ook blootstaat aan extreem intense, ”harde” straling.

Dit is een interessante indicatie voor de feedback die we in de inleiding bespraken. Een mogelijke interpretatie is dat we GS-z14 waarnemen in een dynamische “post-outflow” fase. Er heeft onlangs een extreem heftige stervormingspiek (een starburst) plaatsgevonden. De energie en straling van deze pasgeboren, hete sterren, samen met de vele supernova's, is zó krachtig geweest dat het koudere gas en het stof het stelsel uit zijn geblazen. Het lijkt er dus op dat dit sterrenstelsel een deel van zijn eigen stervormingsbrandstof aan het verdrijven of ioniseren is.

Conclusie

Dit proefschrift toont aan dat het vroege heelal allesbehalve een rustige plek was waar structuren langzaam vormkregen. Door vanuit een submillimeter perspectief te kijken, met ALMA als ons voornaamste instrument, zien we een uiterst dynamisch plaatje. De allereerste sterrenstelsels ontwikkelden zich in een ongekend hoog tempo, verrijkten zichzelf in korte tijd met zware elementen, produceerden massaal grote hoeveelheden kosmisch stof, én bliezen zichzelf leeg door de ongekende kracht van hun eigen ontluikende sterren. Deze ontdekkingen helpen ons te begrijpen hoe een oersoep van koud waterstofgas uiteindelijk evolueerde tot de majestueuze, gestructureerde sterrenstelsels – inclusief onze eigen Melkweg – die we vandaag de dag in het lokale heelal om ons heen zien.

Publications

First-author publications

- *Detection of [O III]$_{88\mu m}$ in JADES-GS-z14-0 at $z = 14.1793$*
  Schouws, Sander, Bouwens, Rychard J., Ormerod, Katherine, Smit, Renske, Algera, Hiddo, Sommovigo, Laura, Hodge, Jacqueline, Ferrara, Andrea, Oesch, Pascal A., Rowland, Lucie E., van Leeuwen, Ivana, Stefanon, Mauro, Herard-Demanche, Thomas, Fudamoto, Yoshinobu, Röttgering, Huub, and van der Werf, Paul
  2025, ApJ, 988, 19
- *Deep Constraints on [CII]158μm in JADES-GS-z14-0: Further Evidence for a Galaxy with Low Gas Content at z=14.2*
  Schouws, Sander, Bouwens, Rychard J., Algera, Hiddo, Smit, Renske, Kumari, Nimisha, Rowland, Lucie E., van Leeuwen, Ivana, Sommovigo, Laura, Ferrara, Andrea, Oesch, Pascal A., Ormerod, Katherine, Stefanon, Mauro, Herard-Demanche, Thomas, Hodge, Jacqueline, Fudamoto, Yoshinobu, Röttgering, Huub, and van der Werf, Paul
  2025, arXiv, arXiv:2502.01610
- *ALMA as a Redshift Machine: Using [C II] to Efficiently Confirm Galaxies in the Epoch of Reionization*
  Schouws, Sander, Bouwens, Rychard, Smit, Renske, Hodge, Jacqueline, Stefanon, Mauro, Witstok, Joris, Hilhorst, Juliëtte, Labbé, Ivo, Algera, Hiddo, Boogaard, Leindert, Maseda, Michael, Oesch, Pascal, Röttgering, Huub, and van der Werf, Paul
  2023, ApJ, 954, 103
- *Significant Dust-obscured Star Formation in Luminous Lyman-break Galaxies at z∼7-8*
  Schouws, Sander, Stefanon, Mauro, Bouwens, Rychard, Smit, Renske, Hodge, Jacqueline, Labbé, Ivo, Algera, Hiddo, Boogaard, Leindert, Carniani, Stefano, Fudamoto, Yoshinobu, Holwerda, Benne W., Illingworth, Garth D., Maiolino, Roberto, Maseda, Michael, Oesch, Pascal, and van der Werf, Paul
  2022, ApJ, 928, 31

Co-authored publications

- *Direct detection of cool molecular gas in a star-forming galaxy at z=7.31*
  Cescon, Karin, Hodge, Jacqueline A., Boogaard, Leindert A., Algera, Hiddo S. B., Rowland, Lucie E., Riechers, Dominik A., Smit, Renske, De Looze, Ilse, Bouwens, Rychard, van der Werf, Paul, Aravena, Manuel, da Cunha, Elisabete, Dayal, Pratika, Ferrara, Andrea, Fisher, Rebecca, Inami, Hanae, Mancera Piña, Pavel E., Oesch, Pascal A., Pallottini, Andrea, Rybak, Matus, Schouws, Sander, Sommovigo, Laura, Stefanon, Mauro, and Vallini, Livia
  2026, MNRAS, 549, stag924
- *A first systematic study of [OIII] 88 μ m at $z > 8$: two luminous oxygen lines and a powerful ionized outflow in the first 600 million years*
  Algera, Hiddo, Weaver, John R., Bakx, Tom J. L. C., Aravena, Manuel, Bouwens, Rychard J., Cescon, Karin, Chen, Chian-Chou, da Cunha, Elisabete, Dayal, Pratika, Faisst, Andreas, Ferrara, Andrea, Fujimoto, Seiji, Hashimoto, Takuya, Heintz, Kasper, Herrera-Camus, Rodrigo, Hodge, Jacqueline, Inami, Hanae, Inoue, Akio K., Matthee, Jorryt, Meyer, Romain, Mizukoshi, Shoichiro, Mondal, Chayan, Nanayakkara, Themiya, Oesch, Pascal A., Pallottini, Andrea, Röttgering, Huub, Rowland, Lucie E., Schouws, Sander, Smit, Renske, Sommovigo, Laura, Stark, Daniel P., Sugahara, Yuma, Vallini, Livia, Vijarnwannaluk, Bovornpratch, van der Werf, Paul, Werner, Norbert, Witstok, Joris, and Xiao, Mengyuan
  2026, OJAp, 9, 65333
- *REBELS-IFU: Spatially Resolved Ionizing Photon Production Efficiencies of 12 Bright Galaxies in the Epoch of Reionization*
  Komarova, Lena, Stefanon, Mauro, Laza-Ramos, Andrés, Algera, Hiddo S. B., Aravena, Manuel, Bouwens, Rychard, Bowler, Rebecca, da Cunha, Elisabete, Dayal, Pratika, Ferrara, Andrea, Fisher, Rebecca, Nanayakkara, Themiya, Rowland, Lucie E., Schouws, Sander, Smit, Renske, Sommovigo, Laura, Stark, Daniel P., and van der Werf, Paul
  2026, ApJ, 1000, 228
- *REBELS-MOSFIRE: Weak C III] Emission Is Typical among Extremely UV-bright, Massive Galaxies at $z \sim 7$*

Endsley, Ryan, Shapley, Alice E., Topping, Michael W., Stark, Daniel P., Bouwens, Rychard J., Rowland, Lucie E., Sommovigo, Laura, Algera, Hiddo S. B., Aravena, Manuel, Bowler, Rebecca A. A., da Cunha, Elisabete, de Looze, Ilse, Ferrara, Andrea, Fisher, Rebecca, González, Valentino, Inami, Hanae, Nanayakkara, Themiya, Schouws, Sander, and Tang, Mengtao
2026, ApJ, 999, 95

- *REBELS-IFU: evidence for metal-rich massive galaxies at $z \sim 6-8$*
Rowland, Lucie E., Stefanon, Mauro, Bouwens, Rychard, Hodge, Jacqueline, Algera, Hiddo, Fisher, Rebecca, Dayal, Pratika, Pallottini, Andrea, Stark, Daniel P., Heintz, Kasper E., Aravena, Manuel, Bowler, Rebecca A. A., Cescon, Karin, Endsley, Ryan, Ferrara, Andrea, Fudamoto, Yoshinobu, Gonzalez, Valentino, Graziani, Luca, Gulis, Cindy, Herard-Demanche, Thomas, Inami, Hanae, Laza-Ramos, Andrès, van Leeuwen, Ivana, de Looze, Ilse, Nanayakkara, Themiya, Oesch, Pascal, Ormerod, Katherine, Palla, Marco, Sartorio, Nina S., Schouws, Sander, Smit, Renske, Sommovigo, Laura, Toft, Sune, Weaver, John R., and van der Werf, Paul
2026, MNRAS, 546, staf2023
- *REBELS-IFU: dust build-up in massive galaxies at redshift 7*
Algera, Hiddo S. B., Rowland, Lucie, Stefanon, Mauro, Palla, Marco, Sommovigo, Laura, Inami, Hanae, Bouwens, Rychard, Aravena, Manuel, Bowler, Rebecca A. A., Dayal, Pratika, De Looze, Ilse, Ferrara, Andrea, Fisher, Rebecca, Graziani, Luca, Gulis, Cindy, Heintz, Kasper, Hodge, Jacqueline, Laza-Ramos, Andrés, van Leeuwen, Ivana, Pallottini, Andrea, Phillips, Siân, Schouws, Sander, Smit, Renske, Stark, Daniel P., and van der Werf, Paul
2026, MNRAS, 545, staf1897
- *The ALMA REBELS survey: [O III]$_{88\mu m}$ line scans of UV-bright $z \gtrsim 7.6$ galaxies*
van Leeuwen, I. F., Bouwens, R. J., Hodge, J. A., van der Werf, P. P., Algera, H. S. B., Schouws, S., Aravena, M., Bowler, R. A. A., Dayal, P., Ferrara, A., Fisher, R., Fudamoto, Y., Gulis, C., Herard-Demanche, T., Inami, H., de Looze, I., Pallottini, A., Smit, R., Sommovigo, L., and Stefanon, M.
2025, MNRAS, 542, 1388

- *REBELS-IFU: on the origin of the elevated [OIII]/[CII] ratios in the early Universe*
  Algera, Hiddo, Rowland, Lucie, Smit, Renske, Fisher, Rebecca, Ramambason, Lise, Kumari, Nimisha, Vallini, Livia, Inami, Hanae, Nanayakkara, Themiya, Stefanon, Mauro, Aravena, Manuel, Bakx, Tom, Bouwens, Rychard, Bowler, Rebecca, Cescon, Karin, Chen, Chian-Chou, Dayal, Pratika, De Looze, Ilse, Ferrara, Andrea, Fudamoto, Yoshinobu, Komarova, Lena, van Leeuwen, Ivana, Ormerod, Katherine, Schouws, Sander, Sommovigo, Laura, Vijayan, Aswin, Wang, Wei-Hao, van der Werf, Paul, and Witstok, Joris
  2025, arXiv, arXiv:2509.16071

- *Beneath the Surface: >85% of z¿5.9 QSOs in Massive Host Galaxies are UV-Faint*
  Bouwens, R. J., Banados, E., Decarli, R., Hennawi, J., Yang, D., Algera, H., Aravena, M., Farina, E., Gloudemans, A., Hodge, J., Inami, H., Matthee, J., Meyer, R., Naidu, R. P., Oesch, P., Rottgering, H. J. A., Schouws, S., Smit, R., Stefanon, M., van der Werf, P., Venemans, B., Walter, F., and Fudamoto, Y.
  2025, arXiv, arXiv:2506.24128

- *REBELS-IFU: dust attenuation curves of 12 massive galaxies at $z\simeq7$*
  Fisher, R., Bowler, R. A. A., Stefanon, M., Rowland, L. E., Algera, H. S. B., Aravena, M., Bouwens, R., Dayal, P., Ferrara, A., Fudamoto, Y., Gulis, C., Hodge, J. A., Inami, H., Ormerod, K., Pallottini, A., Phillips, S. G., Sartorio, N. S., Schouws, S., Smit, R., Sommovigo, L., Stark, D. P., and van der Werf, P. P.
  2025, MNRAS, 539, 109

- *ALMA observations of super-early galaxies: Attenuation-free model predictions*
  Ferrara, A., Carniani, S., di Mascia, F., Bouwens, R. J., Oesch, P., and Schouws, S.
  2025, AA, 694, A215

- *Correction to: Characterising the contribution of dust-obscured star formation at $z \gtrsim 5$ using 18 serendipitously identified [C II] emitters*
  van Leeuwen, I. F., Bouwens, R. J., van der Werf, P. P., Hodge, J. A., Schouws, S., Stefanon, M., Algera, H. S. B., Aravena, M., Boogaard, L. A., Bowler, R. A. A., da Cunha, E., Dayal, P., Decarli, R., Gonzalez, V., Inami, H., de Looze, I., Sommovigo, L., Venemans,

B. P., Walter, F., Barrufet, L., Ferrara, A., Graziani, L., Hygate, A. P. S., Oesch, P., Palla, M., Rowland, L., and Schneider, R.
2024, MNRAS, 535, 3342

- *REBELS-25: discovery of a dynamically cold disc galaxy at $z = 7.31$*
Rowland, Lucie E., Hodge, Jacqueline, Bouwens, Rychard, Mancera Piña, Pavel E., Hygate, Alexander, Algera, Hiddo, Aravena, Manuel, Bowler, Rebecca, da Cunha, Elisabete, Dayal, Pratika, Ferrara, Andrea, Herard-Demanche, Thomas, Inami, Hanae, van Leeuwen, Ivana, de Looze, Ilse, Oesch, Pascal, Pallottini, Andrea, Phillips, Siân, Rybak, Matus, Schouws, Sander, Smit, Renske, Sommovigo, Laura, Stefanon, Mauro, and van der Werf, Paul
2024, MNRAS, 535, 2068

- *Characterising the contribution of dust-obscured star formation at $z \gtrsim 5$ using 18 serendipitously identified [C II] emitters*
van Leeuwen, I. F., Bouwens, R. J., van der Werf, P. P., Hodge, J. A., Schouws, S., Stefanon, M., Algera, H. S. B., Aravena, M., Boogaard, L. A., Bowler, R. A. A., da Cunha, E., Dayal, P., Decarli, R., Gonzalez, V., Inami, H., de Looze, I., Sommovigo, L., Venemans, B. P., Walter, F., Barrufet, L., Ferrara, A., Graziani, L., Hygate, A. P. S., Oesch, P., Palla, M., Rowland, L., and Schneider, R.
2024, MNRAS, 534, 2062

- *The ALMA Reionization Era Bright Emission Line Survey: The molecular gas content of galaxies at $z\sim7$*
Aravena, M., Heintz, K., Dessauges-Zavadsky, M., Oesch, P., Algera, H., Bouwens, R., da Cunha, E., Dayal, P., De Looze, I., Ferrara, A., Fudamoto, Y., Gonzalez, V., Graziani, L., Hygate, A. P. S., Inami, H., Pallottini, A., Schneider, R., Schouws, S., Sommovigo, L., Topping, M., van der Werf, P., and Palla, M.
2024, A&A, 682, A24

- *The ALMA REBELS survey: obscured star formation in massive Lyman-break galaxies at $z=$ 4-8 revealed by the IRX-β and $M_\star$ relations*
Bowler, R. A. A., Inami, H., Sommovigo, L., Smit, R., Algera, H. S. B., Aravena, M., Barrufet, L., Bouwens, R., da Cunha, E., Cullen, F., Dayal, P., De Looze, I., Dunlop, J. S., Fudamoto, Y., Mauerhofer, V., McLure, R. J., Stefanon, M., Schneider, R., Ferrara, A., Graziani, L., Hodge, J. A., Nanayakkara, T., Palla, M., Schouws, S., Stark, D.

P., and van der Werf, P. P.
2024, MNRAS, 527, 5808

- *The ALMA REBELS Survey: discovery of a massive, highly star-forming, and morphologically complex ULIRG at z = 7.31*
  Hygate, A. P. S., Hodge, J. A., da Cunha, E., Rybak, M., Schouws, S., Inami, H., Stefanon, M., Graziani, L., Schneider, R., Dayal, P., Bouwens, R. J., Smit, R., Bowler, R. A. A., Endsley, R., Gonzalez, V., Oesch, P. A., Stark, D. P., Algera, H. S. B., Aravena, M., Barrufet, L., Ferrara, A., Fudamoto, Y., Hilhorst, J. H. A., De Looze, I., Nanayakkara, T., Pallottini, A., Riechers, D. A., Sommovigo, L., Topping, M. W., and van der Werf, P.
  2023, MNRAS, 524, 1775

- *ALMA confirmation of an obscured hyperluminous radio-loud AGN at z = 6.853 associated with a dusty starburst in the 1.5 deg^2 COSMOS field*
  Endsley, Ryan, Stark, Daniel P., Lyu, Jianwei, Wang, Feige, Yang, Jinyi, Fan, Xiaohui, Smit, Renske, Bouwens, Rychard, Hainline, Kevin, and Schouws, Sander
  2023, MNRAS, 520, 4609

- *The ALMA REBELS survey: the dust-obscured cosmic star formation rate density at redshift 7*
  Algera, Hiddo S. B., Inami, Hanae, Oesch, Pascal A., Sommovigo, Laura, Bouwens, Rychard J., Topping, Michael W., Schouws, Sander, Stefanon, Mauro, Stark, Daniel P., Aravena, Manuel, Barrufet, Laia, da Cunha, Elisabete, Dayal, Pratika, Endsley, Ryan, Ferrara, Andrea, Fudamoto, Yoshinobu, Gonzalez, Valentino, Graziani, Luca, Hodge, Jacqueline A., Hygate, Alexander P. S., de Looze, Ilse, Nanayakkara, Themiya, Schneider, Raffaella, and van der Werf, Paul P.
  2023, MNRAS, 518, 6142

- *Correction to: The ALMA REBELS Survey: dust continuum detections at z > 6.5*
  Inami, Hanae, Algera, Hiddo S. B., Schouws, Sander, Sommovigo, Laura, Bouwens, Rychard, Smit, Renske, Stefanon, Mauro, Bowler, Rebecca A. A., Endsley, Ryan, Ferrara, Andrea, Oesch, Pascal, Stark, Daniel, Aravena, Manuel, Barrufet, Laia, da Cunha, Elisabete, Dayal, Pratika, De Looze, Ilse, Fudamoto, Yoshinobu, Gonzalez, Valentino, Graziani, Luca, Hodge, Jacqueline A., Hygate, Alexander P. S.,

Nanayakkara, Themiya, Pallottini, Andrea, Riechers, Dominik A., Schneider, Raffaella, Topping, Michael, and van der Werf, Paul
2023, MNRAS, 518, 3702

- *The REBELS ALMA Survey: efficient Ly α transmission of UV-bright $z\simeq7$ galaxies from large velocity offsets and broad line widths*
Endsley, Ryan, Stark, Daniel P., Bouwens, Rychard J., Schouws, Sander, Smit, Renske, Stefanon, Mauro, Inami, Hanae, Bowler, Rebecca A. A., Oesch, Pascal, Gonzalez, Valentino, Aravena, Manuel, da Cunha, Elisabete, Dayal, Pratika, Ferrara, Andrea, Graziani, Luca, Nanayakkara, Themiya, Pallottini, Andrea, Schneider, Raffaella, Sommovigo, Laura, Topping, Michael, van der Werf, Paul, and Hutter, Anne
2022, MNRAS, 517, 5642

- *The ALMA REBELS Survey: specific star formation rates in the reionization era*
Topping, Michael W., Stark, Daniel P., Endsley, Ryan, Bouwens, Rychard J., Schouws, Sander, Smit, Renske, Stefanon, Mauro, Inami, Hanae, Bowler, Rebecca A. A., Oesch, Pascal, Gonzalez, Valentino, Dayal, Pratika, da Cunha, Elisabete, Algera, Hiddo, van der Werf, Paul, Pallottini, Andrea, Barrufet, Laia, Schneider, Raffaella, De Looze, Ilse, Sommovigo, Laura, Whitler, Lily, Graziani, Luca, Fudamoto, Yoshinobu, and Ferrara, Andrea
2022, MNRAS, 516, 975

- *Dual constraints with ALMA: new [O III] 88-μm and dust-continuum observations reveal the ISM conditions of luminous LBGs at $z\sim7$*
Witstok, Joris, Smit, Renske, Maiolino, Roberto, Kumari, Nimisha, Aravena, Manuel, Boogaard, Leindert, Bouwens, Rychard, Carniani, Stefano, Hodge, Jacqueline A., Jones, Gareth C., Stefanon, Mauro, van der Werf, Paul, and Schouws, Sander
2022, MNRAS, 515, 1751

- *The ALMA REBELS Survey: dust continuum detections at $z > 6.5$*
Inami, Hanae, Algera, Hiddo S. B., Schouws, Sander, Sommovigo, Laura, Bouwens, Rychard, Smit, Renske, Stefanon, Mauro, Bowler, Rebecca A. A., Endsley, Ryan, Ferrara, Andrea, Oesch, Pascal, Stark, Daniel, Aravena, Manuel, Barrufet, Laia, da Cunha, Elisabete, Dayal, Pratika, De Looze, Ilse, Fudamoto, Yoshinobu, Gonzalez, Valentino, Graziani, Luca, Hodge, Jacqueline A., Hygate, Alexander P. S.,

Nanayakkara, Themiya, Pallottini, Andrea, Riechers, Dominik A., Schneider, Raffaella, Topping, Michael, and van der Werf, Paul
2022, MNRAS, 515, 3126

- *The ALMA REBELS Survey: Average [C II] 158 μm Sizes of Star-forming Galaxies from z∼7 to z∼4*
  Fudamoto, Y., Smit, R., Bowler, R. A. A., Oesch, P. A., Bouwens, R., Stefanon, M., Inami, H., Endsley, R., Gonzalez, V., Schouws, S., Stark, D., Algera, H. S. B., Aravena, M., Barrufet, L., da Cunha, E., Dayal, P., Ferrara, A., Graziani, L., Hodge, J. A., Hygate, A. P. S., Inoue, A. K., Nanayakkara, T., Pallottini, A., Pizzati, E., Schneider, R., Sommovigo, L., Sugahara, Y., Topping, M., van der Werf, P., Bethermin, M., Cassata, P., Dessauges-Zavadsky, M., Ibar, E., Faisst, A. L., Fujimoto, S., Ginolfi, M., Hathi, N., Jones, G. C., Pozzi, F., and Schaerer, D.
  2022, ApJ, 934, 144
- *The ALMA REBELS Survey: cosmic dust temperature evolution out to z∼7*
  Sommovigo, L., Ferrara, A., Pallottini, A., Dayal, P., Bouwens, R. J., Smit, R., da Cunha, E., De Looze, I., Bowler, R. A. A., Hodge, J., Inami, H., Oesch, P., Endsley, R., Gonzalez, V., Schouws, S., Stark, D., Stefanon, M., Aravena, M., Graziani, L., Riechers, D., Schneider, R., van der Werf, P., Algera, H., Barrufet, L., Fudamoto, Y., Hygate, A. P. S., Labbé, I., Li, Y., Nanayakkara, T., and Topping, M.
  2022, MNRAS, 513, 3122
- *Reionization Era Bright Emission Line Survey: Selection and Characterization of Luminous Interstellar Medium Reservoirs in the z>6.5 Universe*
  Bouwens, R. J., Smit, R., Schouws, S., Stefanon, M., Bowler, R., Endsley, R., Gonzalez, V., Inami, H., Stark, D., Oesch, P., Hodge, J., Aravena, M., da Cunha, E., Dayal, P., de Looze, I., Ferrara, A., Fudamoto, Y., Graziani, L., Li, C., Nanayakkara, T., Pallottini, A., Schneider, R., Sommovigo, L., Topping, M., van der Werf, P., Algera, H., Barrufet, L., Hygate, A., Labbé, I., Riechers, D., and Witstok, J.
  2022, ApJ, 931, 160
- *Radio and far-IR emission associated with a massive star-forming galaxy candidate at z≃6.8: a radio-loud AGN in the reionization era?*
  Endsley, Ryan, Stark, Daniel P., Fan, Xiaohui, Smit, Renske, Wang,

Feige, Yang, Jinyi, Hainline, Kevin, Lyu, Jianwei, Bouwens, Rychard, and Schouws, Sander
2022, MNRAS, 512, 4248

- *The ALMA REBELS survey: the dust content of z∼7 Lyman break galaxies*
  Dayal, P., Ferrara, A., Sommovigo, L., Bouwens, R., Oesch, P. A., Smit, R., Gonzalez, V., Schouws, S., Stefanon, M., Kobayashi, C., Bremer, J., Algera, H. S. B., Aravena, M., Bowler, R. A. A., da Cunha, E., Fudamoto, Y., Graziani, L., Hodge, J., Inami, H., De Looze, I., Pallottini, A., Riechers, D., Schneider, R., Stark, D., and Endsley, R.
  2022, MNRAS, 512, 989

- *The ALMA REBELS Survey. Epoch of Reionization giants: Properties of dusty galaxies at z≃7*
  Ferrara, A., Sommovigo, L., Dayal, P., Pallottini, A., Bouwens, R. J., Gonzalez, V., Inami, H., Smit, R., Bowler, R. A. A., Endsley, R., Oesch, P., Schouws, S., Stark, D., Stefanon, M., Aravena, M., da Cunha, E., De Looze, I., Fudamoto, Y., Graziani, L., Hodge, J., Riechers, D., Schneider, R., Algera, H. S. B., Barrufet, L., Hygate, A. P. S., Labbé, I., Li, C., Nanayakkara, T., Topping, M., and van der Werf, P.
  2022, MNRAS, 512, 58

- *Spectroscopic confirmation of a gravitationally lensed Lyman-break galaxy at $z_{[CII]}$ = 6.827 using NOEMA*
  Molyneux, S. J., Smit, R., Schaerer, D., Bouwens, R. J., Bradley, L., Hodge, J. A., Longmore, S. N., Schouws, S., van der Werf, P., Zitrin, A., and Phillips, S.
  2022, MNRAS, 512, 535

- *Normal, dust-obscured galaxies in the epoch of reionization*
  Fudamoto, Y., Oesch, P. A., Schouws, S., Stefanon, M., Smit, R., Bouwens, R. J., Bowler, R. A. A., Endsley, R., Gonzalez, V., Inami, H., Labbe, I., Stark, D., Aravena, M., Barrufet, L., da Cunha, E., Dayal, P., Ferrara, A., Graziani, L., Hodge, J., Hutter, A., Li, Y., De Looze, I., Nanayakkara, T., Pallottini, A., Riechers, D., Schneider, R., Ucci, G., van der Werf, P., and White, C.
  2021, Natur, 597, 489

- *The ALMA Spectroscopic Survey in the HUDF: Nature and Physical Properties of Gas-mass Selected Galaxies Using MUSE Spectroscopy*
  Boogaard, Leindert A., Decarli, Roberto, González-López, Jorge, van der Werf, Paul, Walter, Fabian, Bouwens, Rychard, Aravena, Manuel, Carilli, Chris, Bauer, Franz Erik, Brinchmann, Jarle, Contini, Thierry, Cox, Pierre, da Cunha, Elisabete, Daddi, Emanuele, Díaz-Santos, Tanio, Hodge, Jacqueline, Inami, Hanae, Ivison, Rob, Maseda, Michael, Matthee, Jorryt, Oesch, Pascal, Popping, Gergö, Riechers, Dominik, Schaye, Joop, Schouws, Sander, Smail, Ian, Weiss, Axel, Wisotzki, Lutz, Bacon, Roland, Cortes, Paulo C., Rix, Hans-Walter, Somerville, Rachel S., Swinbank, Mark, and Wagg, Jeff
  2019, ApJ, 882, 140

Curriculum Vitae

I was born on the 12 March 1994 in Heemskerk, as the eldest child of Nico and Jolanda Schouws. I grew up in the nearby village of Limmen together with my younger sister, Mandy, and brother, Simon. I attended primary education there and completed my secondary education at the Jac. P. Thijsse College in Castricum, where I obtained my VWO diploma.

During my high school years, I had the opportunity to participate in the LAPP-Top programme for astronomy and the Dutch Astronomy Olympiad, both hosted at Leiden University. This early familiarity with the observatory made Leiden the obvious choice for my university studies, and I enrolled in a double bachelor's programme in Astronomy and Physics. I participated in the honours programme and conducted my bachelor's research project under the supervision of Huub Röttgering, who would later become my promotor. Working with LOFAR data to search for radio haloes and relics in galaxy clusters ignited a lasting passion for radio astronomy.

I continued my studies in Leiden, starting my master's degree Research in Astronomy. I was fortunate to be Jacqueline Hodge's first master's student, working on a project involving the stacking of submillimeter observations, which taught me the power of using the sub-mm regime to study galaxy formation and evolution. For my second research project, I worked with Marijn Franx on the deep LEGA-C survey. This project was my first substantial experience with rest-frame optical spectroscopy and the impact of kinematics on these spectra—concepts that I would continue to build upon later in my research.

After completing my master's degree, I started my PhD research at Leiden Observatory under the supervision of Rychard Bouwens. Shortly before my PhD officially commenced, together with Rychard, we submitted an ALMA proposal that was awarded observing time. The resulting data, together with observations generously shared by Mauro Stefanon, formed the foundation for the first two chapters of this thesis. This early work also helped lay the groundwork for the ambitious REBELS ALMA Large Programme, for which I later had the opportunity to lead the ALMA data reduction efforts.

Building on my growing familiarity with spectral scans and FIR emission lines, I applied for Director's Discretionary Time (DDT) to observe what had recently been identified as the most distant known galaxy. These observations successfully yielded a robust [OIII] detection, leading to the third paper of this thesis. This exciting result ultimately became the basis for the PHOENIX ALMA Large Programme, which I am currently leading.

During my PhD, I enjoyed contributing to the academic community by acting as a teaching assistant for the Computational Astrophysics and Observational Cosmology courses. I also had the pleasure of supervising several bachelor's and master's students during their research projects.

Following the completion of my PhD, I moved to Valencia to take up a postdoctoral position at the University of Valencia, where I will continue my research into the physical processes governing early galaxy evolution.

Acknowledgements

First and foremost, I would like to express my sincere gratitude to my supervisory team: my primary supervisor, Rychard; my promotor, Huub; my co-supervisor, Jackie; and my unofficial co-supervisor, Renske. I am incredibly grateful for your continuous support, endless patience, and the freedom you gave me to explore my own interests. Rychard, thank you for your encouragement and for supporting me in writing proposals. Huub, thank you for the many fruitful discussions about both science and life in general. Jackie, thank you for acting as a trusted confidant throughout this journey.

I am also profoundly grateful to Mauro. When my funding in Leiden came to an end, you went far above and beyond by providing the salary that allowed me to complete this PhD. I am incredibly thankful for your extraordinary generosity and support.

I would also like to thank my PhD colleagues and the wider department in Leiden. Thank you for always being willing to give advice, share insights, and engage in interesting discussions. While there are too many of you to name individually, your support made my time there incredibly rewarding. A special thanks goes to the computer group, who always patiently indulged me and helped resolve even my silliest help desk tickets. To my new colleagues in Valencia: thank you for welcoming me so warmly. You are an amazing and talented group of people, and I am glad to be working with you.

My gratitude also goes to the broader astronomical community, particularly the developers and contributors of the open-source Python packages and public software that we all rely on so heavily.

Outside of the office, my time in Leiden was made much richer by the SKC volleyball association, and I am incredibly grateful to my teammates and everyone at the club for the fun matches, training sessions, and all other activities.

On a personal note, I want to thank my parents for their unconditional support and for always ensuring that I have a home to come back to. To my brother, Simon, and sister, Mandy: thank you for being wonderful siblings, for your constant support, and for the fun city trips that provided the perfect escape from work.

We shall not cease from exploration
And the end of all our exploring
Will be to arrive where we started
And know the place for the first time.

— T. S. Eliot, *Four Quartets*